POLITECNICO DI TORINO

Facoltà di ingegneria

Corso di Laurea in Ingegneria Elettrica

TESI DI LAUREA

FRACTIONAL-SLOT CONCENTRATED-WINDING SURFACE-MOUNTED PERMANENT MAGNET MOTOR DESIGN AND ANALYSIS FOR IN-WHEEL APPLICATION

Relatori:

Prof. Alberto TENCONI

Candidato:

Zijian LI

April 2012

ACKNOWLEDGEMENTS

It is very lucky that I can make a closure to my thesis at home in China. With all the memories of growing up, I want to say the endless love from parents and family is beyond any word of appreciation in this world.

After 42 months living in Turin, Italy, after the joy, depression, prejudice, communication, as a foreigner I could not say my life gets better, but as a person, I feel I get better. I take Turin as my second hometown. I appreciate this city and the people living on this land.

I wish to express my gratitude to Professor AlbertoTenconi for his guidance and support. Without his support, my research activity would not be as present.

I wish to express my gratitude to Professor Radu Bojoi who brought me to the world of motor control, made me enlarge my knowledge and infected me with serious and careful engineering attitude.

I wish to express my thanks to Professor Andrea Cavagnino who helped me to solve the problems about motor design.

I wish to express my deep thanks to Maceratini Roberto and the colleagues in Fiat Research Center who took me as friend and gave me so many fresh and practical ideas.

I wish to express my special thanks to Tao Huang, Di Wu, Daniel Roiu, Alessio Miotto who spent a lot of time to discuss with me and share their knowledge with me.

I wish to express my deep gratitude to Professor Song Liwei in Harbin Institute of Technology, China, who always encouraged me to progress and cleared up my doubts in life and academic research.

I am grateful to my colleagues in the department coming from different countries. The language and cultural difference did not become the barrier for us to have great time.

I am also very grateful to Rasarani Dasi Kleyn, Fabrizio Chiarenza, Marco Rizzi, Giuseppe Abbate, Hua Wang and the friends I met in Italy. We had so much fun. They brought me the passion in life and refreshed my mind to become a confident, independent and complete person.

I wish to express my thanks to the people who ever taught me Italian and listened to my expression with patience.

Last, but not least, I would like to thank Wei Zhuang, Guanjun Pan, Lili Yu, Hao Ma, Tong Liu, Yu Zhang and the friends that we came to Italy together from China. I will not forget the time we spent together. Thank you all.

Zijian LI

April 10th, 2012

Abstract

Title: Fractional-slot concentrated-winding surface-mounted permanent magnet motor design and analysis for in-wheel application

Supervisor: Prof. Alberto Tenconi

Area of Concentration: Converters, Machines and Drives

Keywords: in-wheel motor, SPM motor, motor design, motor control, loss evaluation, efficiency map evaluation, driving cycle analysis, multi-objective optimization, finite element analysis.

Number of pages: 134

The study on the driving cycle and powertrain of electric vehicle presents the conclusion that there is a regular working area on efficiency map where electric motor works for the most time. Thus, two motivations are proposed: first, to evaluate the efficiency map of electric motor analytically, second, to design an electric motor whose maximum efficiency area on efficiency map covers its regular working area.

To evaluate motor efficiency map, three tasks have to be completed: calculating torque-speed characteristic, calculating losses, studying on motor control strategy. For in-wheel application, surface-mounted permanent magnet motor with fractional-slot concentrated-windings is adopted. Its torque-speed profile of flux-weakening control is calculated. Different methods of losses calculation are compared and the results are presented. Motor control strategy is studied to obtain the input electric parameters of other operating points within the torque-speed profile.

To design the motor, driving cycle and powertrain of electric vehicle are analyzed. Multi-objective optimization is utilized to obtain the optimal motor design. Different factors impacting motor efficiency map are discussed. The motor designs are compared to illustrate the loss balance of electric motor.

Motor design and analytic results are validated in powertrain calculation and finite element calculation. Flux-weakening control is implemented. The co-simulation model is built up for further study to calculate the dynamic efficiency of driving cycle. A prototype with similar typology and winding layout is manufactured. Some preliminary experiment results are presented and compared with analytic results.

TABLE OF CONTENTS

Contents

LIST OF TABLES

LIST OF FIGURES

INTRODUCTION

Due to the crude oil crisis and environment pollution by greenhouse gas, electric vehicle has played an important role for the evolution of sustainable harmonious human society. Many prototypes of electric vehicles have been realized and commercialized successfully. Related reports of investigation on the materials and mechanical, electrical, thermal system are also released [1–9].

1.1 In-wheel motor concept

There are various configurations of electric vehicle propulsion system. In (f) of Figure 1 the motor is mounted into the wheels to drive the vehicle directly, which is the so-called in-wheel motor or wheel hub motor. This figure shows the evolution from a normal propulsion system to an in-wheel propulsion system. The advantage of in-wheel motor is illustrated evidently. Figure 2 shows an example of in-wheel motor assembling.

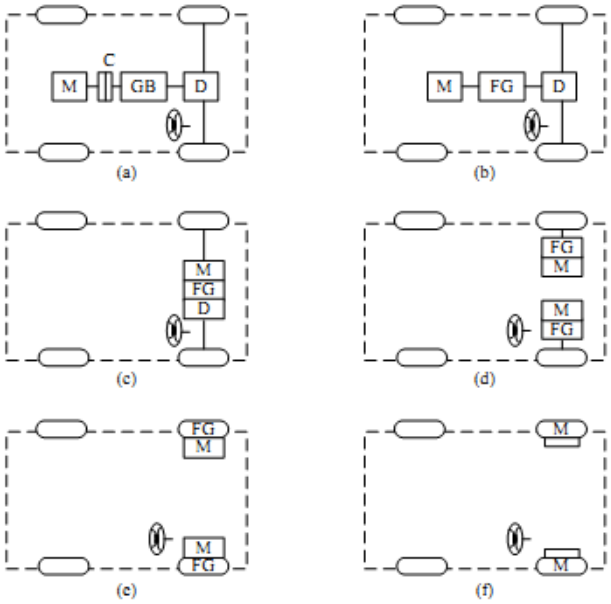

C: Clutch; D: Differential; FG: Fixed gearing; GB: Gearbox; M: Electric motor

Figure 1 Propulsion system configuration of electric vehicle

Compared with other configurations, the adoption of in-wheel motor exhibits following advantages [10]:

(1) The mechanical transmission between the driving motor and wheels can be eliminated. Furthermore, the differential, gearbox, clutch, and connection shafts are not necessary either. The removal of these components will not only bring extra space but also reduce the overall curb weight of the vehicle and further increase the fuel economy.

(2) With less mechanical connection and transmission losses, the compact in-wheel configuration can improve the global efficiency of powertrain.

(3) Due to its very compact assembling, there is more space on board for batteries or other energy sources. Compared with other configurations, extra power will help to extend driving range.

(4) There is more space to assemble the safety apparatuses like energy absorbing boxes for car crash.

(5) The electric vehicle can have four-wheel drive or two-wheel drive. Each individual wheel can be controlled independently, which provides more flexibility during driving.

(6) It is more efficient to collect regenerative power during braking.

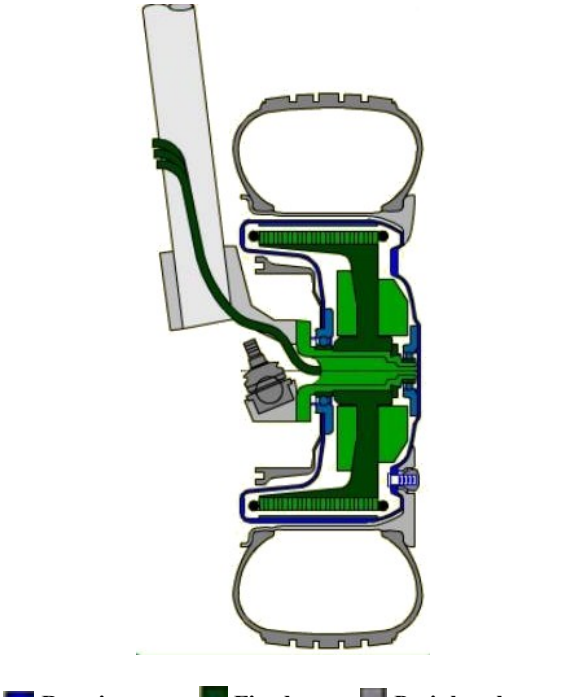

Figure 2 An example of the structure of an in-wheel motor

1.2 Products overview

Figure 3 Michielin active wheel system

Michielin invented the active wheel system since 2008. The system has the common features of in-wheel application like no engine under hood, gearboxes or transmission. In addition, this wheel system also integrates a compact active suspension inside. There are two electric motors. One motor delivers 30kW continuous power for traction and braking, the other functions for the active suspension control. The active suspension system can stabilize the car when driving on bumps. Michelin also developed the electronics and the battery pack with the capacities ranging from 15KWh to 38KWh.

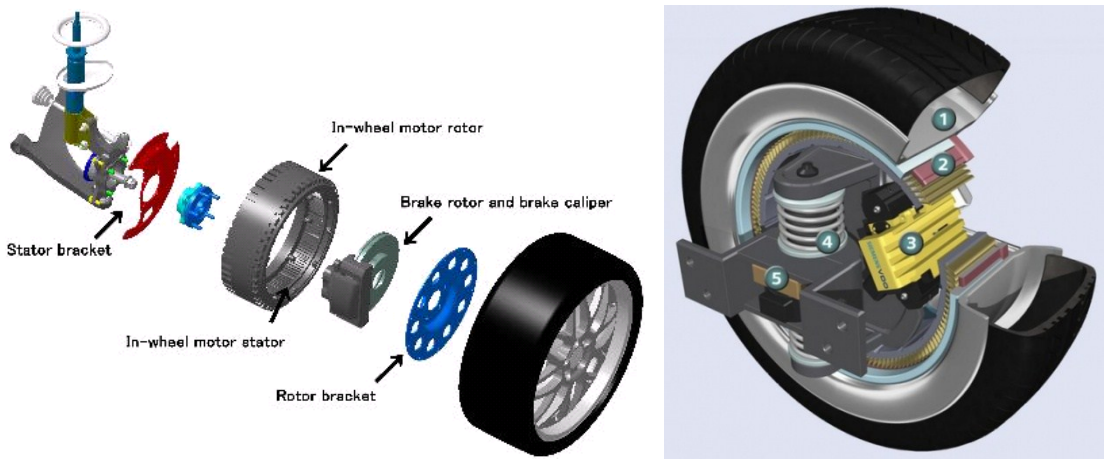

(1) wheel rim (2) in-wheel motor (3) electronic wedge brake

(4) active suspension (5) electronic steering

Figure 4 The in-wheel motor of Siemens VDO

Siemens VDO proposed the concept of "drive-by-wire" and started the so-called eCorner project in 2006 [11]. They developed Electric Corner Modules (ECM) to replace the conventional wheel suspension system, which can be any combination of tire, wheel, brake, steering, suspension, electric motor and/ or cooling system. The main target is to reduce the vehicle weight and improve the fuel economy. Figure 4 displays the explosion view and the composition of the wheel.

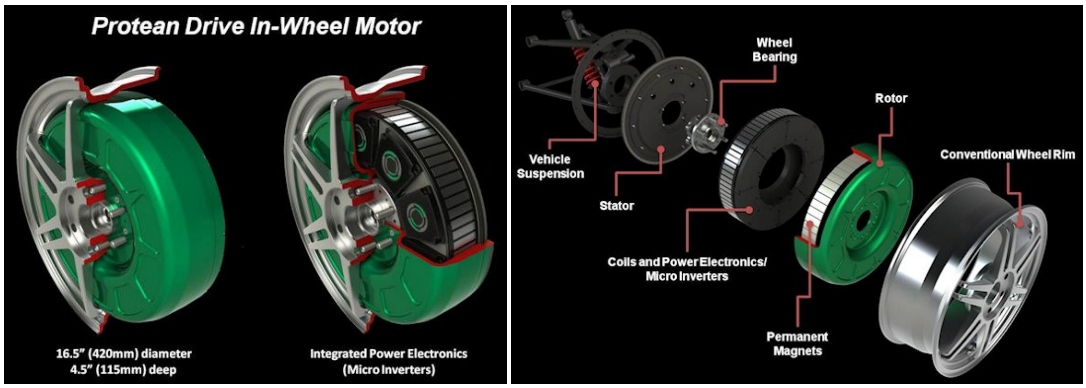

Figure 5 Protean in-wheel motor

Protean electric developed liquid-cooling in-wheel motors with integrated inverters [12] as shown in Figure 5. This electric in-wheel motor can be used as vehicle's unique traction power source which

will lead to radical redesigns of the car body. Alternatively, as a secondary power of combustion engine in hybrid electric vehicle, it will serve to boost the power during acceleration, improve fuel economy or to realize zero emission in urban drive-cycle. Figure 6 shows the overview of the powertrain of an electric vehicle adopting in-wheel motor. Figure 7 shows the torque-speed and power-speed characteristics of Protean in-wheel motor. It can be seen that the motor can deliver 81kW peak power and 64kW continuous power with the inverter DC voltage 400V.

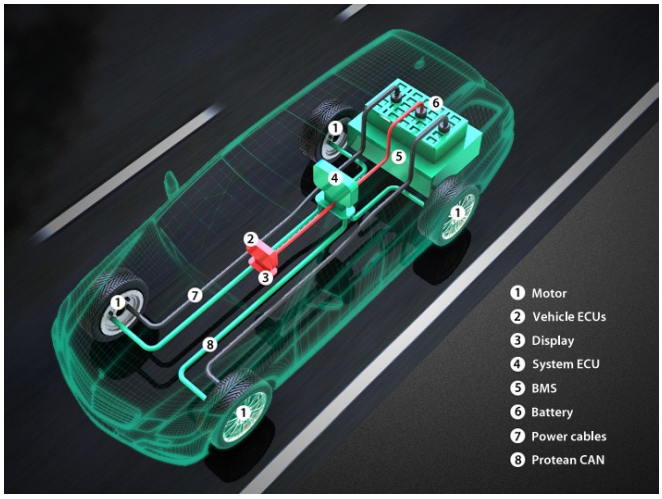

Figure 6 Powertrain of electric vehicle with in-wheel motor

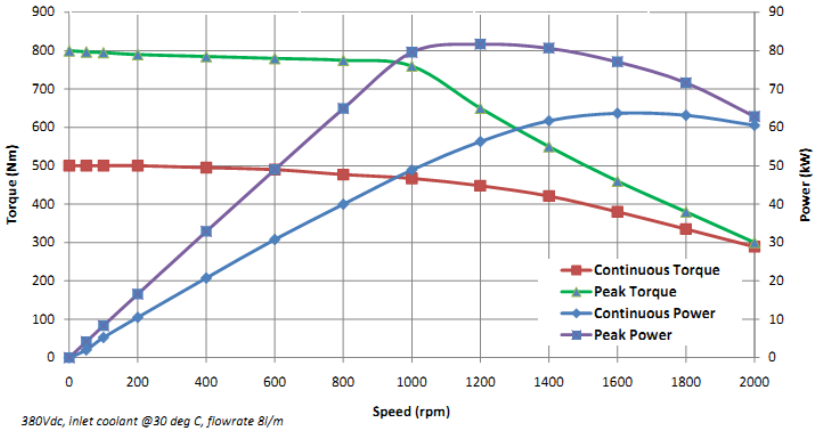

Figure 7 The torque-speed and power-speed characteristics of Protean in-wheel motor

Table 1 Performance of Protean in-wheel motor

Peak power @400V	81kW
Continuous power @400V	64kW
Peak torque	800Nm
Continuous torque	500Nm
DC voltage	200-400V
Length	115mm
Diameter	420mm
Mass	31kg

Besides the above-mentioned companies, also other car producers manufactured electric vehicle with in-wheel motor like Mitsubishi iMEV, Ford Hi-Pa Drive F-150, Volvo C-30 recharge, Porsche 918 Spyder, PML Mini etc.

1.3 Challenges and design considerations

Although there is a bundle of advantages that in-wheel motor could bring for the development of electric vehicle, there still exist many challenges, which may hinder in-wheel motor's wide utilization.

First, the in-wheel electric motor increases the weight of the wheel, which influences vehicle dynamics. This influence may make the suspension difficult to adapt to the road profile and cause vibration of car body. This indicates the weight and power density are very important crucial points during in-wheel motor design.

Second, the in-wheel motor is assembled into the wheels, which is not supported by sprung. This requires changes to the suspension and damping systems or even redesigning the vehicle's structure. Conventional vehicle will not be applicable to mount in-wheel motor.

Third, due to the enclosed operating conditions and the integrated electronic module, the in-wheel motor confronts harsh thermal and cooling problems. This also proposes the requirements of high-efficiency motor design, effective cooling system, as well as accurate thermal field prediction.

Besides, high starting torque and overloading torque are also requested during starting the vehicle, accelerating or climbing ramps.

1.4 Comparison of motor typologies

Many papers have compared various types of suitable traction motors for electric vehicle. In [13], the authors discussed about the basic characteristics of electric traction motor for electric vehicle and reviewed the merits of induction, switched reluctance motor, permanent magnet brushless motor as well as their motor drives. In [14], induction, brushless and synchronous reluctance motors are compared for application in high performance drive. In [15], the authors discussed different kinds of permanent magnet motors and their drives for electric vehicle. In [16], the reluctance motor is compared with induction motor from the view of torque density and the paper illustrates the benefits brought by magnet adoption.

For in-wheel traction application although some papers reported to use the switched reluctance motor due to its inherent fault-tolerant ability and simple construction [17]. However, due to the high requirement on high power density of in-wheel application, permanent magnet motor still appears to be the ideal candidate and widely used. Both the axial flux motor and radial flux motor adoption are reported in [18–20]. In [21] and [22], they are compared from the view of motor design [23] and performance. External-rotor surface mounted permanent (SPM) magnet motor has drawn more attention for in-wheel motor solution as shown in Figure 4 and Figure 5. The external rotor can be mounted directly on the rim to drive the wheels. The speed of the motor is equal to the speed of electric vehicle. No gears are needed. Besides, this kind of in-wheel motor can be designed into pancake shape with high ratio of stator diameter to length, which makes the motor deliver high torque at low speed.

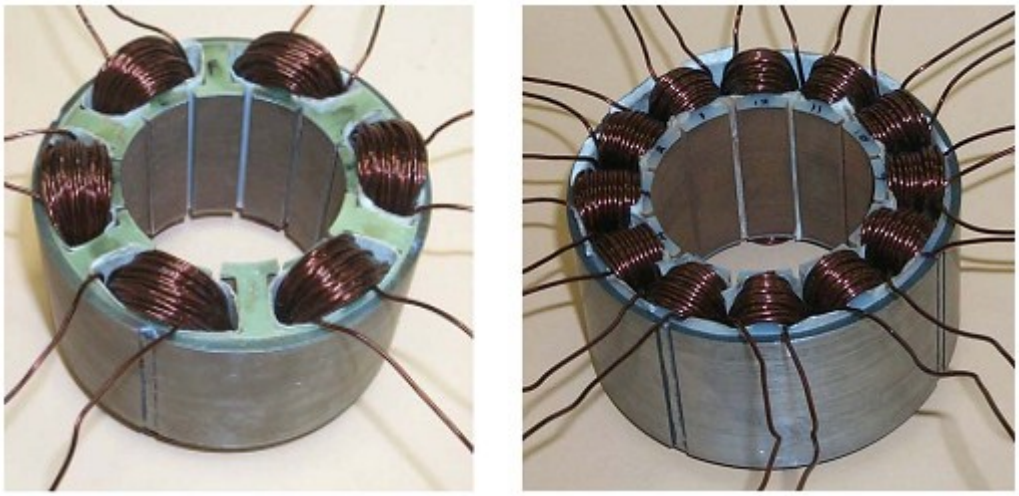

Figure 8 12-slots 10-poles fractional-slot concentrated winding [24]

(left: single layer; right: double layer)

Usually SPM motor is considered to have lower flux-weakening capability due to the lower winding inductance, because the actual airgap, the thickness of magnet plus the thickness of airgap, is very large. However, [25–27] proposed SPM motor design with fractional-slot concentrated windings as shown in Figure 8, which significantly increase the winding inductance. From the view of fault tolerance, [28–30] mentioned that non-overlapped single-layer concentrated windings, which have alternate teeth wound, separate phase windings physically, magnetically and thermally. This character yields nearly zero mutual inductances and avoids phase-phase short circuit. As for turn-turn short circuit, large slot leakage inductance inhibits the short-circuit current, which can be designed lower than the limit current of inverter. [31] and [32] compared the impact of winding layer number indicating that double-layer windings yield lower torque ripple and magnet eddy current losses than single layer windings while contribute to a lower overload torque capability. Besides, all these references reported fractional-slot concentrated windings inherently exhibits low cogging torque, short end-windings and, hence, a low copper loss, high efficiency and high power density as well as excellent flux-weakening performance. Except the serious attention on the magnet loss and temperature, SPM motor with fractional-slot single-layer concentrated winding become attractive candidate for the in-wheel application of electric vehicle.

1.5 Key points of in-wheel motor design

As discussed in previous two sections, during in-wheel motor design there are several key points that should be considered. First, the shape of the motor has to be pancake, which has big ratio of motor diameter to length. One reason is the room of the motor has to be compatible with that of the rim. Another reason is that pancake motor could deliver high torque at low speed. This character makes this kind of motor suitable for the direct-drive application.

Second, the volume of motor has a limit due the dimensional limit of the rim. With the possible cooling system and acceptable temperature rise, the torque density is expected to reach the optimal value. In another word, that means the constraints of motor design are dimensional limit and cooling

condition. The input of motor design is the requested peak torque. The objective is to design a motor with the minimum volume or weight.

Last key point and the most important one is the efficiency. The motor used for electric vehicle is different from the conventional electric motor, which is designed and optimized based on rated operating point. The in-wheel motor is required to have wide range of high efficiency area on efficiency map. Efficiency map is composed of x-axis representing speed, y-axis representing torque and z-axis contour representing efficiency. However, different driving cycles have different torque-speed requests. Usually these requests congregate in a certain area called motor's regular operating area. If motor's high efficiency area can match its regular working area, the high efficiency motor design is realized [33], [34]. Thus driving cycle oriented motor design becomes important if the electric vehicle commonly operates for some certain driving situation like urban car, city bus or highway vehicle.

1.6 Objectives of the thesis

First, this thesis starts from external-rotor SPM motor design and analysis. A program for electromagnetic design has been developed. The magnetic field and motor losses are calculated analytically. Torque-speed characteristic is predicted. With the knowledge of motor control strategy, motor efficiency map is evaluated.

Second, the impacts on motor efficiency map are discussed. Based on a specific driving cycle and powertrain, efficiency map oriented multi-objective optimization design procedure is developed. The SPM motor is designed to have its regular working area covered by its maximum efficiency area.

Third, different motor designs have been evaluated with the help of finite element method (FEM) and powertrain analysis software [35].

CHAPTER I

EXTERNAL-ROTOR SURFACE PERMANENT MAGNET MOTOR DESIGN

In this chapter, the basic permanent magnet motor design theory will be discussed. Different winding layouts are introduced. Basic analysis of electromagnetic circuit within stator and rotor is implemented. Motor dimensions are specified preliminarily.

1.1 Winding layout design

The winding layout for three-phase motor can be classified into two kinds: overlapping windings and non-overlapping windings. As in Figure 9, overlapping windings can be distributed windings (Figure 9.a) or concentrated windings (Figure 9.b). While non-overlapping windings are concentrated windings with each tooth wound (or called single-layer winding as shown in Figure 9.c) or alternate tooth wound (or called double-layer winding as shown Figure 9.d).

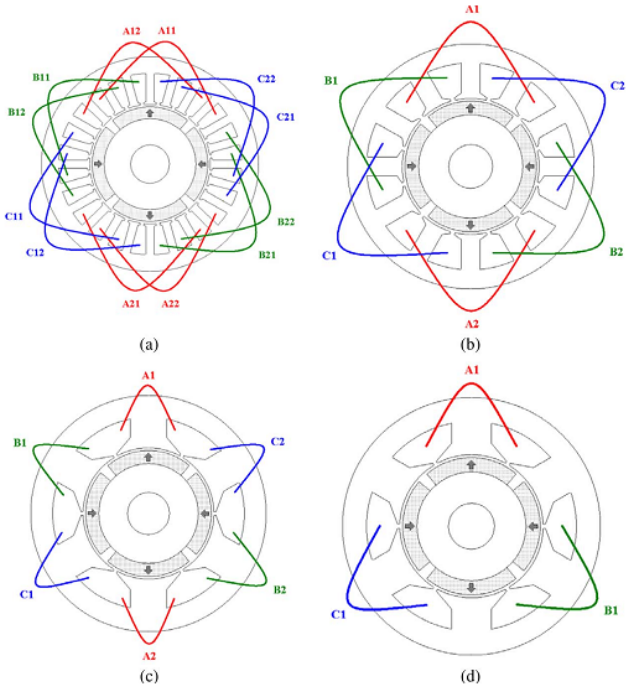

Figure 9 Winding layout

For the last few years, fractional-slot concentrated-winding (FSCW) permanent magnet motor has drawn more interest due to its short end turns, high slot fill factor, low cogging torque, flux-weakening ability and fault tolerance [24], [28], [36]. In [37], the comparison between Figure 9.b, Figure 9.c and Figure 9.d indicates FSCW motor with alternate tooth wound has a significantly higher self-inductance due to the higher harmonic and slot leakage components and significantly lower mutual inductance. In [31], the conclusions are made that the FSCW motor with alternate tooth wound in Figure 9.d has higher spatial sub-harmonics of MMF resulting in higher torque ripple and magnet eddy-current losses compared to Figure 9.c. However, it may have better

overload performance, flux-weakening ability as well as better fault tolerance due to the physical, magnetic, thermal separation between phase windings.

In [38], Bianchi proposed "Star of Slots" theory to design winding layout. Slot-star is the distribution of coils on compass based on their electrical degrees as shown in Figure 10, which belongs to a combination of 24 slots 28 poles. For double-layer winding, there are *Qs* coils and *Qs* spokes in slot-star. But for single-layer winding, there are *Qs*/2 coils and *Qs*/2 spokes viz deleting one spoke between each two spokes.

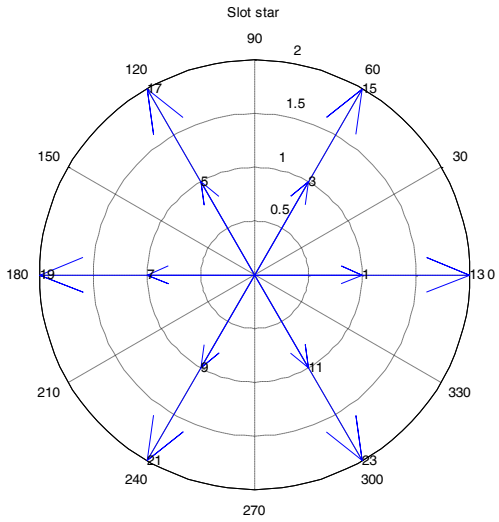

Figure 10 Single-layer slot-star of 24 slots and 28 poles

When choosing the combination of slot and pole numbers, the following constraints have to be respected.

- The number of spokes per phase $Q_s/(mt)$ must be integer, t is the greatest common divisor of pole-pair number and slot number,
- Considering the effect of cogging torque, the number of slots per pole should not be an integer except the three-slots-per-pole series.

Besides, for single-layer winding, there is an additional constraint, which is:

- Q must be even.

After the slot-star is drawn, the spokes need to be classified into each phase belt of 60 elec.deg. There are six phase belts. The sequence is A+, C-, B+, A-, C+, B-. For the case of Figure 10, the spokes belonging to the respective phase belt are classified as [1 13], [3 15], [5 17], [7 19], [9 21], [11 23]. Then with knowing the coil span, slot-star and spoke classification the winding layout is identified. As the case in Fig.1, the coil span is 1. There are 4 coils each phase which will be connected in series. The winding layout is shown in Table1, where '1' denotes the coil side going into the slot, '-1' denotes the coil side going out of the slot, '0' denotes no coil. Its MMF of

individual phase can be drawn as shown in Figure 11, assuming one turn per coil and 1A current imposed.

Table 2 Single-layer winding layout of 24 slots and 28 poles

A	1	-1	0	0	0	0	-1	1	0	0	0	0	1	-1	0	0	0	0	-1	1	0	0	0	0
B	0	0	0	0	1	-1	0	0	0	0	-1	1	0	0	0	0	1	-1	0	0	0	0	-1	1
C	0	0	-1	1	0	0	0	0	1	-1	0	0	0	0	-1	1	0	0	0	0	1	-1	0	0

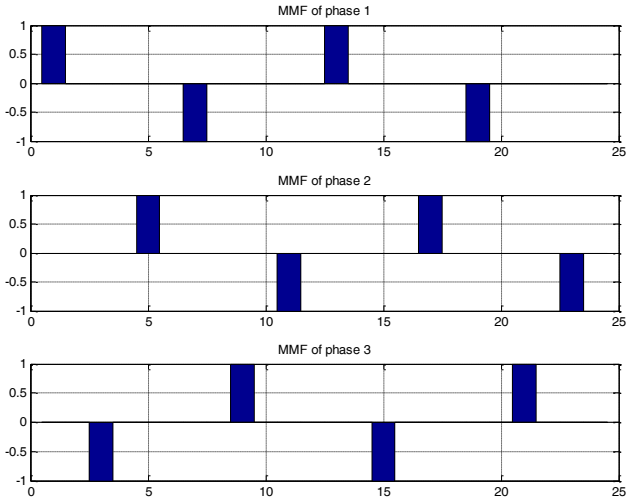

Figure 11 Single-layer MMF of each phase of 24 slots and 28 poles

As for double-layer winding, there are *Qs* coils and *Qs* spokes in slot-star, which leads to the different winding layout from single-layer winding.

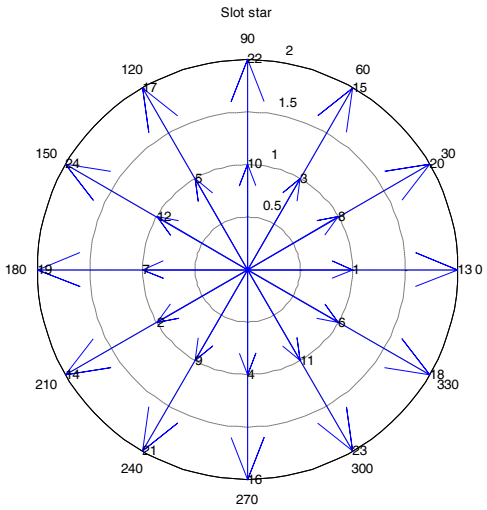

Figure 12 Double-layer slot-star of 24 slots and 28 poles

The coil span is 1 and there are 8 coils each phase which are connected in series. The winding layout is shown in Table 3. Its MMF of individual phase can be drawn as shown in Figure 13, assuming one turn per coil and 1A current imposed.

Table 3 Double-layer winding layout of 24 slots and 28 poles

A	1	-1	1	0	0	0	-1	1	-1	0	0	0	1	-1	1	0	0	0	-1	1	-1	0	0	0
B	-1	0	0	0	1	-1	1	0	0	0	-1	1	-1	0	0	0	1	-1	1	0	0	0	-1	1
C	0	0	-1	1	-1	0	0	0	1	-1	1	0	0	0	-1	1	-1	0	0	0	1	-1	1	0

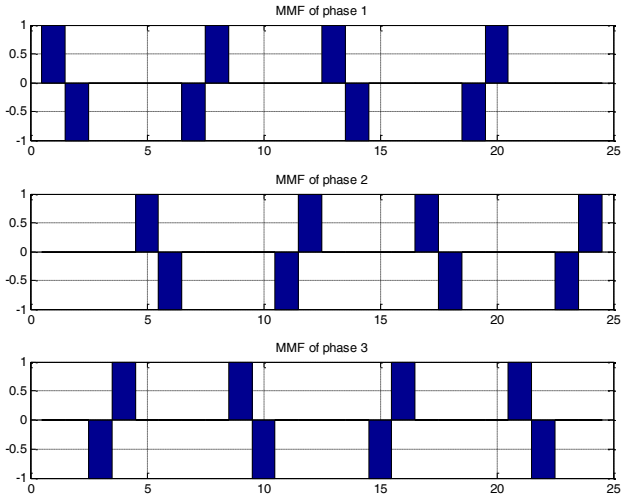

Figure 13 Double-layer MMF of each phase of 24 slots and 28 poles

With the matrix of MMF, the Fourier analysis is implemented to get the amplitude and phase angles of each harmonic. The analysis starts with Figure 11 and Figure 13. The slot numbers are transferred into mechanical radian as the x-axis. The amplitudes of MMF are multiplied by the phase current and turns per coil. Following equations are utilized during Fourier analysis,

$$MMF(\theta) = a_0 + \sum_{n=1}^{\infty}(a_n cosn\omega_0\theta + b_n sinn\omega_0\theta) \tag{1.1}$$

$$a_0 = \frac{1}{T}\int_{t0}^{t0+T} f(\theta)d\theta \tag{1.2}$$

$$a_n = \frac{2}{T}\int_{t0}^{t0+T} f(\theta)cosn\omega_0\theta d\theta \tag{1.3}$$

$$b_n = \frac{2}{T}\int_{t0}^{t0+T} f(\theta)sinn\omega_0\theta d\theta \tag{1.4}$$

Where,

$$T = 2\pi \tag{1.5}$$

$$\omega_0 = \frac{2\pi}{T} \tag{1.6}$$

The amplitude of each harmonic is expressed as

$$A = \sqrt{a_n^2 + b_n^2} \tag{1.7}$$

The phase angle of each harmonic is expressed as

$$\varphi = -atan(\frac{b_n}{a_n}) \tag{1.8}$$

For the harmonic analysis of all three phases, the amplitude and phase angle are calculated from those of each phase as

$$A_{all} = \sqrt{(a_{n1} + a_{n2} + a_{n3})^2 + (b_{n1} + b_{n2} + b_{n3})^2} \tag{1.9}$$

$$\varphi_{all} = -atan(\frac{b_{n1} + b_{n2} + b_{n3}}{a_{n1} + a_{n2} + a_{n3}}) \tag{1.10}$$

Figure 14 shows the MMF harmonics of single-layer winding for 24 slots and 28 poles. Figure 15 shows the compass of MMF harmonics of three phases.

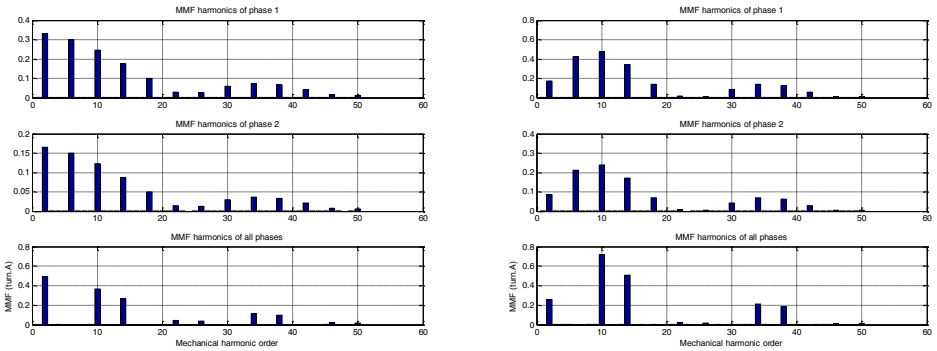

Figure 14 MMF harmonics of phase 1, phase2 and all the phases for 24 slots and 28 poles (left: single-layer winding; right: double-layer winding)

After the winding layout is configured, winding factor is calculated by

$$k_{wv} = k_{dv}k_{pv} \tag{1.11}$$

Where,

k_{dv}, is distribution factor of the v-th harmonic,

k_{pv}, is the pitch factor of the v-th harmonic.

The distribution factor of double-layer FSCW can be calculated from the slot-star. It is defined as vector sum over arithmetic sum of spokes in slot-star.

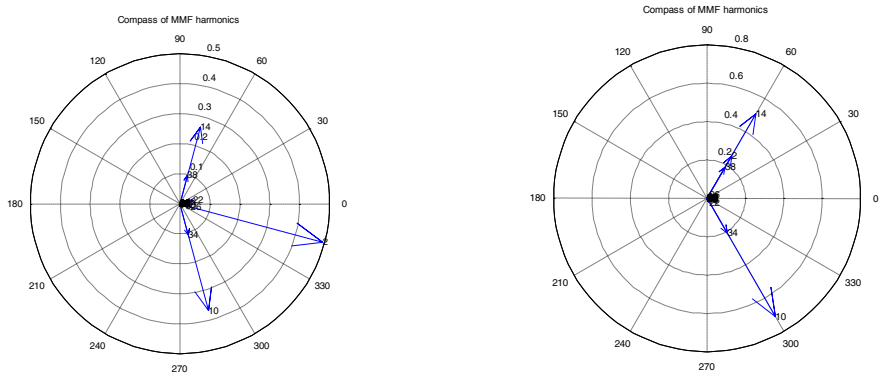

Figure 15 Compass of MMF harmonics of three phases for 24 slots and 28 poles (left: single-layer winding; right: double-layer winding)

While, the pitch factor is independent from slot-star and computed by

$$k_{p\nu} = sin(\frac{2\pi\nu\sigma_Q}{Q_s}) \tag{1.12}$$

Where,

ν, is the harmonic order,

Q_s, is the slot number,

σ_Q, is the coil throw.

The computing results of 24 slots 28 poles for both the single-layer winding and the double-layer winding are presented in Figure 16.

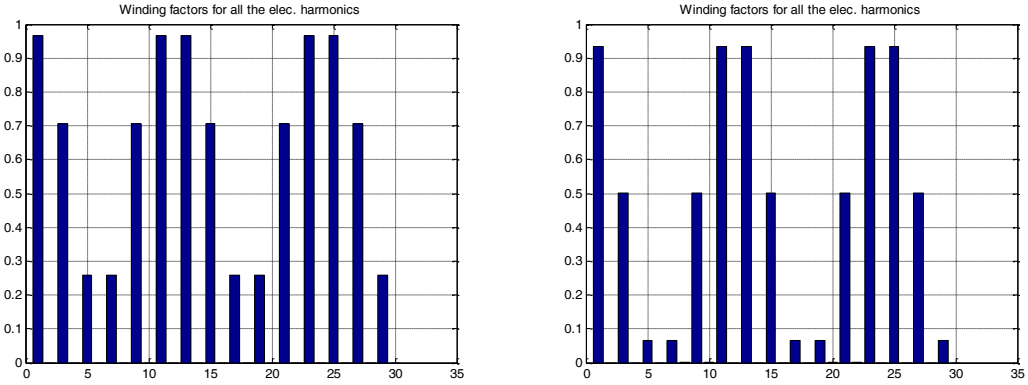

Figure 16 Winding factors for 24 slots and 28 poles (left: single-layer winding; right: double-layer winding)

Table 4 lists all the possible combinations of slot and pole number until 48 slots and 40 poles. The combinations with 2/5 and 2/7 slot/pole/phase are suggested to be better candidates [25] marked with light dark color. The column of *Qs/t* and *Qs/(2t)* will help to illustrate the orders of harmonics contained in MMF as presented in Table 5. The column of fundamental winding factor

is for single-layer winding. The column of LCM(*2p,Qs*) lists the index of cogging torque, where higher value generally indicates higher amplitude of cogging torque.

Table 4 Combinations of slots and poles

p	*Qs*	*q=Qs/(2pm)*	*t*=GCD*(p,Qs)*	*Qs/t*	*Qs/(2t)*	k_{wp}	LCM*(2p,Qs)*
6	18	1/2	6	3	1.5	0.866	36
8	12	1/4	4	3	1.5	0.866	48
8	18	3/8	2	9	4.5	0.945	144
8	24	1/2	8	3	1.5	0.866	48
8	30	5/8	2	15	7.5	0.711	240
8	36	3/4	4	9	4.5	0.617	144
10	18	2/7	2	9	4.5	0.945	180
10	24	2/5	2	12	6.0	0.966	120
10	30	1/2	10	3	1.5	0.866	60
10	36	3/5	2	18	9.0	0.735	180
10	42	2/3	2	21	10.5	0.650	420
10	48	4/5	2	24	12.0	0.588	240
12	18	1/4	6	3	1.5	0.866	72
12	36	1/2	12	3	1.5	0.866	72
14	24	2/7	2	12	6.0	0.966	168
14	30	1/3	2	15	7.5	0.951	420
14	36	3/7	2	18	9.0	0.902	252
14	42	1/2	14	3	1.5	0.866	84
14	48	4/7	2	24	12.0	0.766	336
16	24	1/4	8	3	1.5	0.866	96
16	30	1/3	2	15	7.5	0.951	480
16	36	3/8	4	9	4.5	0.945	288
16	42	4/9	2	21	10.5	0.890	672
16	48	1/2	16	3	1.5	0.866	96
21	36	2/7	3	12	6.0	0.966	252
20	48	2/5	4	12	6.0	0.966	240

Table 5 Characteristics of different combinations of slots and poles

<table>
<tr><td></td><td colspan="2">*Qs/t* even</td><td>*Qs/t* odd</td></tr>
<tr><td>Double layer</td><td colspan="2">Harmonics: (2n-1)t
Mutual inductance M=0 when $\sigma_Q = 1$</td><td>Harmonics: nt
M $\neq$ 0</td></tr>
<tr><td colspan="4">Transfer double-layer to single-layer (Qs even, σ_Q odd)</td></tr>
<tr><td rowspan="2">Single layer</td><td rowspan="2">k_d increases
Harmonics: (2n-1)t
M=0 when $\sigma_Q = 1$</td><td rowspan="2">k_d unchanged
Harmonics: nt
M $\neq$ 0</td><td>only if t is even</td></tr>
<tr><td>k_d unchanged
Harmonics: nt/2
M $\neq$ 0</td></tr>
</table>

1.2 Stator design

Stator design includes electrical design and slot geometrical design. The requested torque specifies the phase current and the number of turns per coil and the current density is checked further.

1.2.1 Phase current

The average electromagnetic torque is calculated from the main components of airgap flux density and linear current density [39], [40].

$$T_{eq-avg} = \frac{\pi}{4}\widehat{B_{g1}}\widehat{K_{sp}}D^2L_{stk} \tag{1.13}$$

Where,

$\widehat{K_{sp}}$, is the fundamental harmonic of the electric loading,

D, is the outer diameter of stator,

L_{stk}, is the length of lamination,

$\widehat{B_{g1}}$, is the peak value of fundamental harmonic of air gap flux density.

$$\widehat{B_{g1}} = \frac{4}{\pi}B_g\, sin(p\alpha_{pm}) \tag{1.14}$$

Where,

$2\alpha_{pm}$, is the mechanical permanent magnet cover angle of one pole.

B_g, is the peak value of airgap flux density as shown in Figure 17.

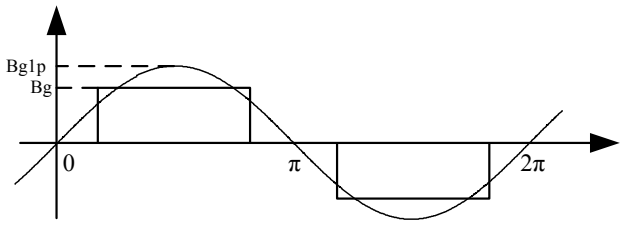

Figure 17 Airgap flux density

Thus if T_{eq-avg} is the requested design torque,

$$\widehat{K_{sp}} = \frac{T_{eq-avg}}{\frac{\pi}{4}\widehat{B_{g1}}D^2L_{stk}} \tag{1.15}$$

The corresponding fundamental phase peak current is

$$I_p = \frac{\widehat{K_{sp}}\pi D}{6k_{wp}T_{ph}} \tag{1.16}$$

Where,

k_{wp}, is the fundamental winding factor,

T_{ph}, is the number of series turns per phase.

The slot current is given by

$$\hat{I}_{slot} = \frac{\widehat{K}_{sp}\pi D}{k_{wp}Q_s} \tag{1.17}$$

Furthermore, the rms value of the slot current density can be expressed as

$$J = \frac{\hat{I}_{slot}}{\sqrt{2}S_{Cu}} = \frac{\widehat{K}_{sp}\pi D}{\sqrt{2}S_{Cu}k_{wp}Q_s} \tag{1.18}$$

1.2.2 Slot dimensions

Assuming knowing the peak flux density in airgap, stator tooth and yoke, stator outer diameter and inner diameter, the slot dimensions can be specified as following [41–43].

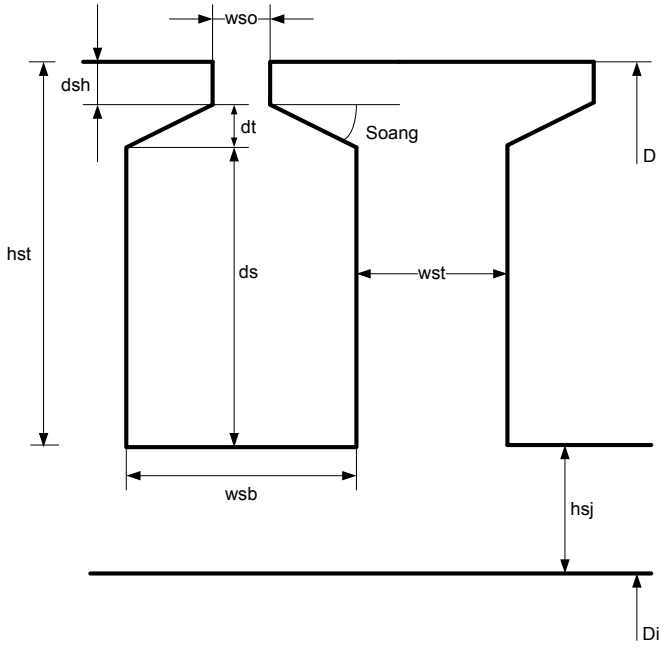

Figure 18 Slot dimensions

The stator yoke thickness is given by

$$h_{sj} = \frac{B_g \pi D}{2 B_{sj} 2p K_{Fe}} \tag{1.19}$$

Where,

B_g, is the peak open-circuit airgap flux density,

D, is the surface diameter of stator,

B_{sj}, is the peak flux density in stator yoke,

p, is the number of pole pairs,

K_{Fe}, is the lamination stacking factor.

The tooth height

$$h_{st} = \frac{D - D_i}{2} - h_{sj} \tag{1.20}$$

Where,

D_i, is the inner diameter of stator.

For factional-slot single-layer concentrated winding, some winding design can exhibit higher torque capability and lower torque ripple with unequal tooth widths [44]. The coils are wound on alternate teeth, which are wider than the unwound teeth as shown in Figure 19. The width of the wider teeth is almost equal to the pole pitch for maximizing the flux linkage.

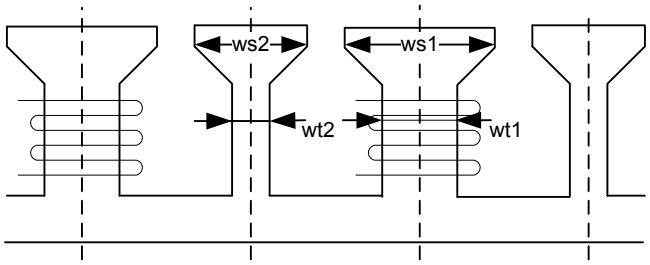

Figure 19 Unequal tooth width

The wider tooth width is given by

$$w_{t1} = \frac{B_g \pi D}{B_{st1} Q_s} \frac{2}{1 + t_r} \tag{1.21}$$

Where,

B_{st1}, is the peak flux density in wider tooth,

Q_s, is the slot number,

t_r, is the ratio of w_{t2} to w_{t1}, $w_{t2} = w_{t1}t_r$

Therefore, the flux density in narrower tooth is

$$B_{st2} = \frac{B_{st1}}{t_r} \tag{1.22}$$

Neglecting the tooth tip, the slot area results

$$\begin{aligned} S_{slot} &= \frac{\pi}{4Q_s}\left[D^2 - \left(D_i + 2h_{sj}\right)^2\right] - \frac{1}{2}w_{t1}h_{st} - \frac{1}{2}w_{t1}t_r h_{st} \\ &= \frac{\pi}{4Q_s}\left[D^2 - \left(D_i + 2h_{sj}\right)^2\right] - \frac{1}{2}w_{t1}(1 + t_r)h_{st} \end{aligned} \tag{1.23}$$

The total copper cross sectional area within the slot is given by

$$S_{Cu} = k_{fill}S_{slot} \tag{1.24}$$

Where, k_{fill} is the slot fill factor.

The length of two stator end-windings can be approximated as

$$L_{ew} = \frac{\pi}{2}\frac{p_s' + w_{st}}{2} + p_s' k_{ov}(\delta - 1) \tag{1.25}$$

Where,

w_{st}, is the width of stator tooth,

δ, is coil span,

p_s', is expressed as

$$p_s' = \frac{\pi(D - h_{st})}{Q_s} \tag{1.26}$$

For the unequal-tooth-width windings with coil span $\delta = 1$, the length of two stator end-windings can be expressed as

$$L_{ew} = \frac{\pi}{2}\frac{p_s' + w_{t1}}{2} \tag{1.27}$$

Thus, the total copper volume can be calculated by

$$Vol_{Cu} = S_{Cu}(L + L_{ew})Q_s \tag{1.28}$$

The volume of the stator teeth is

$$Vol_{st} = \left(\frac{D - D_i}{2} - \frac{B_g \pi D}{2B_{sj} 2pK_{Fe}}\right) \frac{B_g \pi D}{B_{st}} L_{stk} \tag{1.29}$$

For unequal-width stator tooth the volume is

$$Vol_{st1} = \left(\frac{D - D_i}{2} - \frac{B_g \pi D}{2B_{sj} 2pK_{Fe}}\right) \frac{B_g \pi D L_{stk}}{B_{st1}} \frac{1}{1 + t_r} \tag{1.30}$$

$$Vol_{st2} = \left(\frac{D - D_i}{2} - \frac{B_g \pi D}{2B_{sj} 2pK_{Fe}}\right) \frac{B_g \pi D L_{stk}}{B_{st1}} \frac{t_r}{1 + t_r} \tag{1.31}$$

The volume of the stator yoke is given by

$$Vol_{sj} = \pi L_{stk} [\frac{D_i B_g \pi D}{4pB_{sj} K_{Fe}} + \left(\frac{B_g \pi D}{4pB_{sj} K_{Fe}}\right)^2] \tag{1.32}$$

1.3 Rotor design

The dimensions of magnet and rotor are specified in this section. The value of permanent magnet remanence is influenced by its working temperature.

$$B_r = \left(1 + \frac{(t_m - 20)\alpha_{Br}}{100}\right)\left(1 + \frac{I_l}{100}\right) B_{r20} \tag{1.33}$$

Where,

t_m, is the working temperature of permanent magnet,

α_{Br}, is the temperature coefficient,

I_l, is the temperature coefficient.

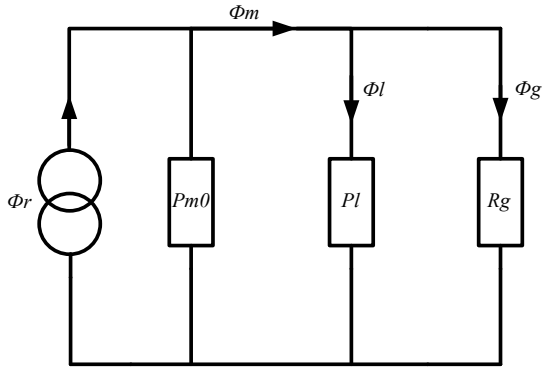

Figure 20 Magnetic circuit for one pole of SPM motor

According to the magnetic open circuit for one pole as shown in Figure 20,

$$P_m = P_{m0} + P_L = P_{m0}(1 + p_{rl}) \tag{1.34}$$

$$\Phi_m = \Phi_g + \Phi_L \tag{1.35}$$

$$\Phi_L = \frac{P_L}{P_{m0} + P_L}(\Phi_r - \Phi_g) \tag{1.36}$$

Where,

$$P_{m0} = \frac{\mu_0 \mu_r A_m}{L_m} \tag{1.37}$$

Therefore,

$$\Phi_m = \Phi_g + \frac{p_{rl}}{1 + p_{rl}}\left(\Phi_r - \Phi_g\right) \tag{1.38}$$

Considering the airgap reluctance R_g, the airgap flux is expressed as

$$\Phi_g = \frac{1/R_g}{1/R_g + P_{m0} + P_L}\Phi_r = \frac{1}{1 + (1 + p_{rl})P_{m0}R_g}\Phi_r \tag{1.39}$$

Where,

$$R_g = \frac{g_c}{\mu_0 A_g} \tag{1.40}$$

$$g_c = k_c g \tag{1.41}$$

The Carter coefficient is,

$$k_c = \frac{\tau_s}{\tau_s - b_0 + \frac{4g}{\pi} log(1 + \frac{\pi b_0}{4g})} \tag{1.42}$$

Where,

b_0, is slot opening,

g, is thickness of airgap,

τ_s, is slot pitch, $\tau_s = \frac{\pi D}{Q_s}$.

If the flux leakage factor is defined as

$$f_{LKG} = \frac{\Phi_g}{\Phi_m} = \frac{\Phi_g}{\Phi_g + \Phi_L} = \frac{1}{1 + P_L R_g} = \frac{1}{1 + p_{r1} P_{m0} R_g} \tag{1.43}$$

Thus, combining (1.38), (1.39) and (1.43) it can be obtained that

$$\Phi_m = \frac{1}{1 + f_{LKG} P_{m0} R_g} \Phi_r \tag{1.44}$$

$$\Phi_g = \frac{f_{LKG}}{1 + f_{LKG} P_{m0} R_g} \Phi_r \tag{1.45}$$

Given that $\Phi_g = B_g A_g$, $\Phi_r = B_r A_m$,

$$B_g = \frac{f_{LKG}}{1 + f_{LKG} P_{m0} R_g} \frac{A_m}{A_g} B_r \tag{1.46}$$

Where,

$$A_g \approx A_m = \frac{\alpha_p \pi D L_{\text{stk}}}{2p} \tag{1.47}$$

α_p, is the magnet-arc to pole-arc ratio.

According to the reference [45], the magnet-arc to pole-arc ratio can be specified as

$$\alpha_p = \frac{N_k - k_1}{N_k}, k_1 = 0, 1, 2..N_k \tag{1.48}$$

Where, $N_k = \big(LCM(Q_s, 2p)\big)/2p$.
In practice, due to fringing of magnet flux into the slots, the optimum of magnet-arc ratio should be increased slightly by a small factor k_2,

$$\alpha_p = \frac{N_k - k_1}{N_k} + k_2, k_1 = 1, 2..N_k - 1 \tag{1.49}$$

Where,

$k_1 = 1$, is usually the preferred value,

$k_2 = 0.01$~0.03.

The rotor yoke thickness is given by

$$h_{rj} = \frac{\alpha_p B_g \pi (D + 2g)}{2 B_{rj} 2p K_{Fe}} \tag{1.50}$$

Where,

B_{rj}, is the peak flux density in rotor yoke.

CHAPTER II

EXTERNAL-ROTOR SURFACE PERMANENT MAGNET MOTOR ANALYSIS

For in-wheel application on electric vehicle, the evaluation of SPM motor efficiency is important. Different motor designs could exhibit different efficiency maps. Investigating on design factors influencing motor's efficiency map, this chapter starts the SPM motor analysis with four main parts. First, basic analyses are implemented like the calculation of magnetic field and phase inductance [46]. Second, control strategies are discussed in order to calculate motor performance like torque-speed characteristic. Third, three main kinds of losses are calculated analytically. The results are compared and used to evaluate efficiency of each working point on the efficiency map. Finally, the impact of losses distribution on efficiency map is illustrated, which discloses the reason of the location of the maximum efficiency point on efficiency map. Equations of loss balance are presented. It is expected that the location of the maximum efficiency point on efficiency map could be predicted.

2.1 Magnetic field of outer-rotor SPM

2.1.1 Calculation of open-circuit magnetic field

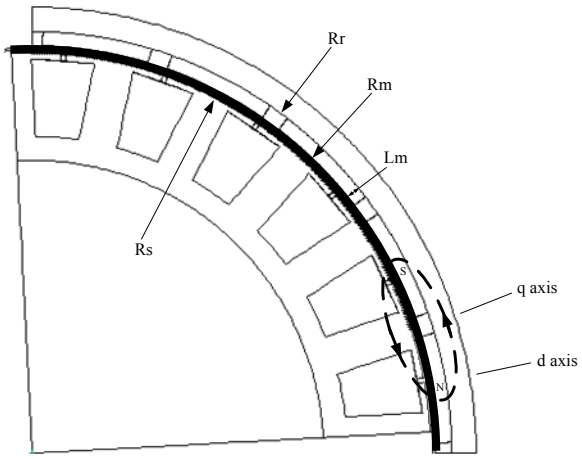

Figure 21 SPM motor cross section

The magnetic field generated by the magnet is calculated at first without considering slot effect. The permeance of lamination is assumed to be infinite to ignore the saturation. From [47], the relations between $\boldsymbol{B}$ and $\boldsymbol{H}$ are

$$\boldsymbol{B_I} = \mu_0 \boldsymbol{H_I} \tag{2.1}$$

in the airgap, where the value of airgap permeance is 1 and

$$\boldsymbol{B_{II}} = \mu_m \boldsymbol{H_{II}} + \mu_0 \boldsymbol{M} \tag{2.2}$$

in the permanent magnet. $\boldsymbol{M}$ is the residual magnetization vector. $\mu_m = \mu_0 \mu_r$ is the recoil permeability, where μ_r is the relative recoil permeability.

In terms of the scalar magnetic potential φ

$$\boldsymbol{H} = -\nabla\varphi \tag{2.3}$$

Where,

$$\nabla^2\varphi_I = 0 \tag{2.4}$$

in the airgap and

$$\nabla^2\varphi_{II} = \frac{\mathrm{div}\boldsymbol{M}}{\mu_r} \tag{2.5}$$

in the permanent magnet.

The magnetization vector $\boldsymbol{M}$ is given by

$$\boldsymbol{M} = M_r\boldsymbol{r} + M_\theta\boldsymbol{\theta} \tag{2.6}$$

Where

$$M_r = \sum_{n=1,3,5,\ldots}^{\infty} M_n cos(np\theta) \tag{2.7}$$

$$M_\theta = 0 \tag{2.8}$$

p is the number of pole pairs, θ is the angle with reference to d-axis as shown in Figure 22.

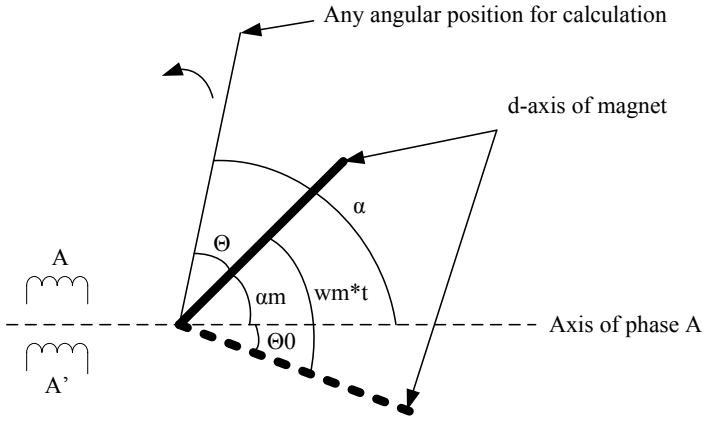

Θ is the mec. angular position refered to the rotor axis
α is the mec.angular position refered to the axis of phase A
Θ0 is an initial mec. angle depending on the commutation angle
wm is the mec.angular velocity

Figure 22 Indication of angular position

M_n is given by

$$M_n = \frac{2B_r\alpha_p}{\mu_0}\frac{sin(\frac{n\pi\alpha_p}{2})}{\frac{n\pi\alpha_p}{2}} \tag{2.9}$$

Where,

α_p, is the magnet pole-arc to pole-pitch ratio,

B_r, is the remanence.

Therefore

$$\text{div}\boldsymbol{M} = \frac{M_r}{r} + \frac{\partial M_r}{\partial r} + \frac{1}{r}\frac{\partial M_\theta}{\partial \theta} = \frac{M_r}{r} \tag{2.10}$$

Thus, according to Laplace's equation (2.4) in the airgap, quasi-Poissonian equation (2.5) in the permanent magnet and the boundary conditions as following,

$$H_{\theta I}(r,\theta)|_{r=R_s} = 0 \tag{2.11}$$

$$H_{\theta II}(r,\theta)|_{r=R_r} = 0 \tag{2.12}$$

$$B_{rI}(r,\theta)|_{r=R_m} = B_{rII}(r,\theta)|_{r=R_m} \tag{2.13}$$

$$H_{\theta I}(r,\theta)|_{r=R_m} = H_{\theta II}(r,\theta)|_{r=R_m} \tag{2.14}$$

φ_I and φ_{II} can be solved. Knowing (2.3) and (2.6) replacing $\boldsymbol{H_I}$ and $\boldsymbol{H_{II}}$ in (2.1) and (2.2), flux density in magnets and airgap can be calculated.

Therefore, for the external rotor motor, the normal component of magnetic field distribution in the airgap ($R_s < r < R_m$) when $p \neq 1$ is

$$B_{rOC}(\theta) = \sum_{n=1,3,5\ldots}^{\infty} \frac{(-\mu_0 M_n)}{\mu_r}\frac{np}{(np)^2-1}\left\{\frac{(np-1)\left(\frac{R_m}{R_r}\right)^{2np} + 2\left(\frac{R_m}{R_r}\right)^{np-1} - (np+1)}{\frac{\mu_r+1}{\mu_r}\left[1-\left(\frac{R_s}{R_r}\right)^{2np}\right] - \frac{\mu_r-1}{\mu_r}\left[\left(\frac{R_s}{R_m}\right)^{2np} - \left(\frac{R_m}{R_r}\right)^{2np}\right]}\right\} \cdot \left[\left(\frac{r}{R_m}\right)^{np-1} + \left(\frac{R_s}{R_m}\right)^{np-1}\left(\frac{R_s}{r}\right)^{np+1}\right] cos(np\theta) \tag{2.15}$$

The normal component of magnetic field distribution at the stator surface ($r = R_s$) for external rotor motors when $p \neq 1$ is

$$B_{rOC}(\theta) = \sum_{n=1,3,5\ldots}^{\infty} \frac{2(-\mu_0 M_n)}{\mu_r} \frac{np}{(np)^2-1} \left(\frac{R_s}{R_m}\right)^{np-1} \cdot \left\{ \frac{(np-1)\left(\frac{R_m}{R_r}\right)^{2np} + 2\left(\frac{R_m}{R_r}\right)^{np-1} - (np+1)}{\frac{\mu_r+1}{\mu_r}\left[1-\left(\frac{R_s}{R_r}\right)^{2np}\right] - \frac{\mu_r-1}{\mu_r}\left[\left(\frac{R_s}{R_m}\right)^{2np} - \left(\frac{R_m}{R_r}\right)^{2np}\right]} \right\} cos(np\theta) \quad (2.16)$$

Where $\theta = 0$ corresponds to the axis of pole N.

The second step of magnetic field calculation is to consider the slot effect. One method is to calculate the relative permeance proposed in [48]. Another way is to calculate the slot correction factor proposed in [49]. Here the method of reference [48] is adopted. Because of the existence of slotting, the open-circuit magnetic field is modulated as

$$B'_{rOC}(\alpha, r, t) = B_{rOC}(\alpha + \alpha_m)\tilde{\lambda}(\alpha, r) \quad (2.17)$$

where,

$\alpha_m = \frac{2\pi n}{60} t - \theta_0$, is the angle between d-axis and the axis of phase A,

t is time, *s*,

n is the speed, rpm,

$\tilde{\lambda}$ is relative permeance, which is given by

$$\tilde{\lambda}(\alpha, r) = \tilde{\Lambda}_0(r) + \sum_{\mu=1}^{\infty} (\tilde{\Lambda}_\mu(r) \cos \mu Q_s(\alpha + \alpha_{sa})) \quad (2.18)$$

Where, Q_s is the slot number. When the coil span is an odd multiple of the slot pitch, viz the axis of phase A is in line with the center of a stator tooth, $\alpha_{sa} = \frac{\pi}{Q_s}$ elec.rad. When the coil span is an even multiple of the slot pitch, viz the axis of phase A is in line with the center of a stator slot, $\alpha_{sa} = 0$ elec.rad, then $\alpha = 0$ corresponds to the axis of phase A.

$$\tilde{\Lambda}_0(r) = \frac{1}{K_c}\left(1 - \frac{1.6\beta(r) b_0}{\tau_s}\right) \quad (2.19)$$

$$\tilde{\Lambda}_\mu(r) = -\beta(r)\frac{4}{\pi\mu}\left[0.5 + \frac{\left(\mu\frac{b_0}{\tau_s}\right)^2}{0.78125 - 2\left(\mu\frac{b_0}{\tau_s}\right)^2}\right] \cdot sin\left(1.6\mu\pi\frac{b_0}{\tau_s}\right) \quad (2.20)$$

Where, b_0 is the slot opening, $\tau_s = 2\pi R_s/Q_s$ is the slot pitch.

$$\beta(r) = \frac{1}{2}\left[1 - \frac{1}{\sqrt{1 + \left(\frac{b_0}{2g'}\right)^2 (1 + \upsilon^2)}}\right] \tag{2.21}$$

Where υ is determined from

$$\frac{y\pi}{b_0} = \frac{1}{2} ln\left(\frac{\sqrt{a^2 + \upsilon^2} + \upsilon}{\sqrt{a^2 + \upsilon^2} - \upsilon}\right) + \frac{2g'}{b_0} arctan(\frac{2g'}{b_0}\frac{\nu}{\sqrt{a^2 + \upsilon^2}}) \tag{2.22}$$

$$a^2 = 1 + \left(\frac{2g'}{b_0}\right)^2 \tag{2.23}$$

For external rotor motor

$$y = R_s + g' - r \tag{2.24}$$

$$g' = \frac{L_m}{\mu_r} + g \tag{2.25}$$

g, is the length of airgap, L_m is the thickness of magnet.

k_c, is the Carter coefficient, which is approximated by

$$k_c = \frac{\tau_s}{\tau_s - \gamma g'} \tag{2.26}$$

Where,

$$\gamma = \frac{4}{\pi}\left\{\frac{b_0}{2g'}\tan^{-1}\left(\frac{b_0}{2g'}\right) - \ln\sqrt{1 + \left(\frac{b_0}{2g'}\right)^2}\right\} \tag{2.27}$$

The open-circuit magnetic field of a 24 slots 20 poles SPM motor is calculated and compared with FEA results in Figure 24 and Figure 25. The specification of the motor is shown in Table 6. The initial position of rotor is shown in Figure 21, where q-axis is in line with the axis of phase A when t=0s. In Figure 24 and Figure 25, zero angle represents the location of q-axis.

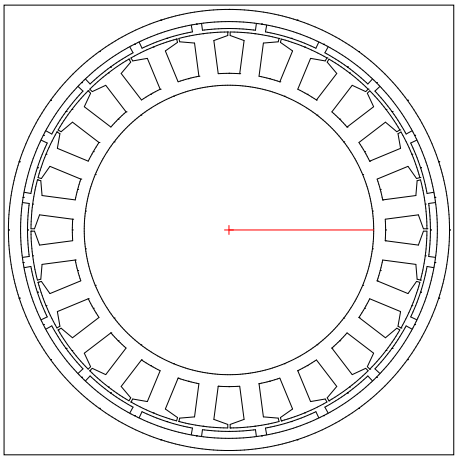

Figure 23 24 slots 20 poles SPM motor

Table 6 Specification of the SPM motor

Slots, Q_s	24
Pole pairs, p	10
Phase number, m	3
Coil span, δ	1
Remnant flux density, B_r	1.11T
Magnet pole arc, α_M	151.2 elec.deg
Magnet length, L_m	6mm
Airgap length, g	3mm
Slot opening, b_0	2mm
Stator outer radius, R_s	171mm
Magnet inner radius, R_m	174mm
Rotor inner radius, R_r	180mm
Stator tooth width, w_{st}	16.8mm
Stator yoke width, h_{sj}	10.3mm

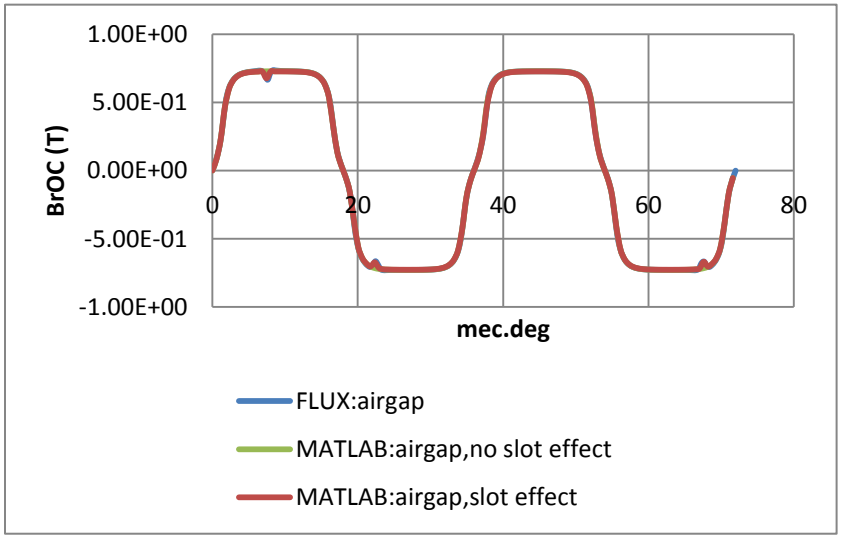

Figure 24 Comparison of airgap magnetic field

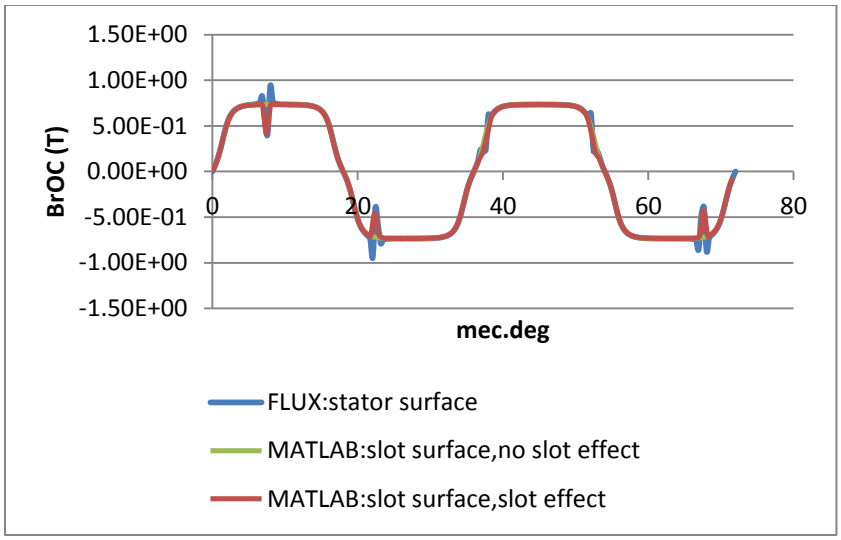

Figure 25 Comparison of slot surface magnetic field

2.1.2 Calculation of armature reaction field

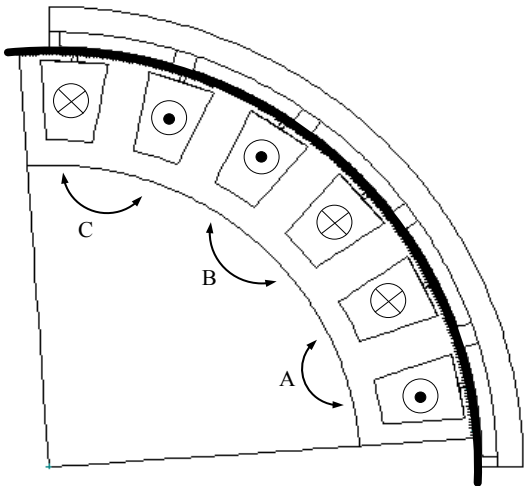

Figure 26 Configuration of winding layout

The input three phase currents are given by [50]

$$i_a = I_p \cos(pw_m t + \gamma) \tag{2.28}$$

$$i_b = I_p \cos(pw_m t + \gamma - \frac{2}{3}\pi) \tag{2.29}$$

$$i_c = I_p \cos(pw_m t + \gamma - \frac{4}{3}\pi) \tag{2.30}$$

Where,

I_p, is the peak value of current source,

p, is the number of pole pairs,

w_m, is the mechanical angular velocity, mec.rad/s,

γ, is the current advanced angle, elec.rad. When $\gamma = 0$ the axis of phase A is aligned with the q-axis. When $\gamma = \pi/2$ the axis of phase A should be aligned with the d- axis. According to Figure 22, $\gamma = \frac{\pi}{2} - p\theta_0$.

The Fourier series expansion of a winding distribution are expressed as

$$n_{da}(\alpha_{sl}) = \sum_{\upsilon=1}^{\infty} n_{d\upsilon} sin(\upsilon\alpha_{sl}) \tag{2.31}$$

$$n_{db}(\alpha_{sl}) = \sum_{\upsilon=1}^{\infty} n_{d\upsilon} sin(\upsilon\alpha_{sl} - \frac{2}{3}\pi) \tag{2.32}$$

$$n_{dc}(\alpha_{sl}) = \sum_{\upsilon=1}^{\infty} n_{d\upsilon} sin(\upsilon\alpha_{sl} - \frac{4}{3}\pi) \tag{2.33}$$

Where,

α_{sl}, is the mechanical angle with reference to slot-opening center of coil-going-out slot of phase A.

$$n_{d\upsilon} = \frac{4}{\pi}\frac{k_{w\upsilon}T_{ph}}{D} \tag{2.34}$$

$k_{w\upsilon}$, is the υ-th harmonic winding factor,

T_{ph}, is the number of series turns per phase,

D, is the diameter of the stator.

The linear current density is given by

$$\begin{aligned} K_s(\alpha_{sl}, t) = \sum_{\upsilon=1}^{\infty} [& i_a n_{d\upsilon} \sin(\upsilon\alpha_{sl})) + i_b n_{d\upsilon} \sin\left(\upsilon\alpha_{sl} - \frac{2}{3}\pi\right) \\ & + i_c n_{d\upsilon} \sin(\upsilon\alpha_{sl} - \frac{4}{3}\pi)] \\ = & \sum_{\upsilon=1}^{\infty} \frac{3}{2} n_{d\upsilon} I_p \sin(\upsilon\alpha_{sl} - p w_m t - \gamma) \end{aligned} \tag{2.35}$$

Whose amplitude is defined as

$$K_{sv} = \frac{3}{2} n_{dv} I_p = \frac{6 k_{wv} T_{ph} I_p}{\pi D} \tag{2.36}$$

Therefore, the magnetic field caused by armature reaction is

$$B_{arm}(\alpha_{sl}, t) = \frac{\mu_0 K_s(\alpha_{sl})}{g + \frac{L_m}{\mu_r}} \tag{2.37}$$

Considering slot effect,

$$B'_{arm}(\alpha, r, t) = B_{arm}\left(\alpha + \frac{\pi}{p Q_s}, t\right) \tilde{\lambda}(\alpha, r) \tag{2.38}$$

Where $\tilde{\lambda}(\alpha, r)$ is the relative permeance in (2.18).

The same prototype shown in Figure 23 and Table 6 is utilized to calculate the magnetic field of armature reaction. The results are compared with those of FEA method. It should be noticed that according to the assumptions, the magnet is set as air and the permeance of lamination is infinite in FEA method. Three phases are driven by sinusoidal current sources.

The input parameters are shown in Table 7. The initial position of rotor is shown in Figure 26. The axis of phase A is in line with q-axis. Figure 27 shows the comparison of armature reaction magnetic field at the initial position. Figure 28 shows the comparison when the rotor rotates by 9 mec.deg. The impulse ripples of FEA results are possibly caused by the unrefined mesh.

Table 7 Input parameters

Speed, *rpm*	450 rpm
Peak phase current, I_p	724.45A
Current advanced angle, γ	0 elec.rad

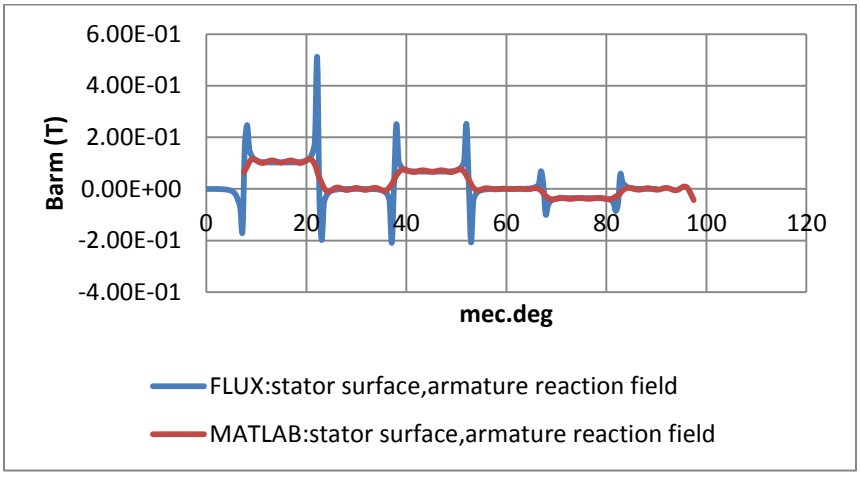

Figure 27 Comparison of armature reaction magnetic field at the initial position

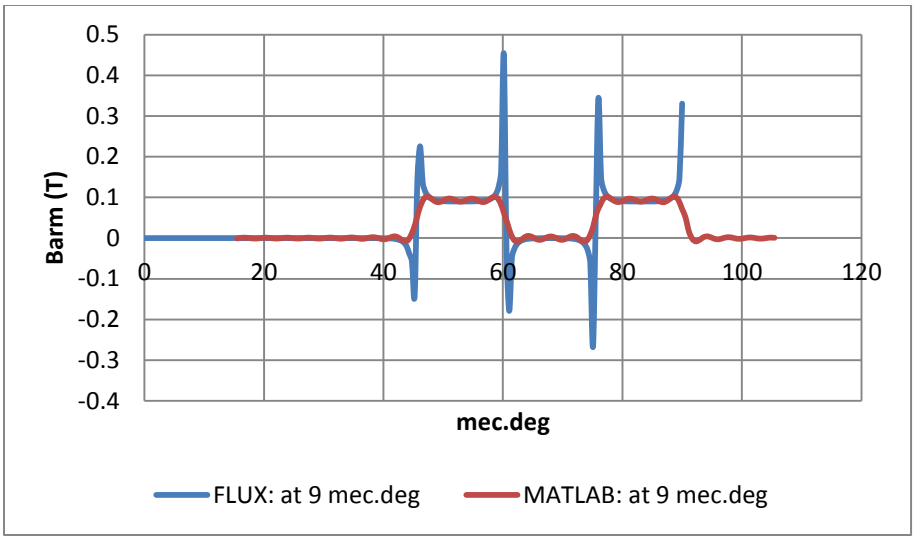

Figure 28 Comparison of armature reaction magnetic field at 9 mec.deg

2.1.3 Calculation of load magnetic field

In the proceeding discussion, the permeability of stator and rotor iron is assumed to be infinite. The analysis on magnetic field is simplified as a linear problem and the load magnetic field can be obtained by superposition of the open-circuit magnetic field and armature reaction magnetic field [51], [52]. That is,

$$B_{load}(\alpha, r, t) = B'_{rOC}(\alpha, r, t) + B'_{arm}(\alpha, r, t) \tag{2.39}$$

Where,

$\alpha = 0$ corresponds to the axis of phase A,

t is time, s.

The only problem is to unify the different reference frames when implementing superposition. Table 8 shows the different initial angular positions when calculating open-circuit field, armature-reaction field and relative permeance of slot.

Table 8 Different reference frames when calculating magnetic field

	Initial angular position to calculate
Open-circuit field	d-axis
Armature-reaction field	Slot-opening center of coil-going-out slot of phase A
Relative permeance of slot	The axis of phase A

The input parameters are still the same as in Table 7. The initial position of rotor is shown in Figure 26. The axis of phase A is in line with q-axis. Figure 29 shows the comparison of load magnetic field at the initial position. Figure 30 shows the comparison when the rotor rotates by 9 mec.deg.

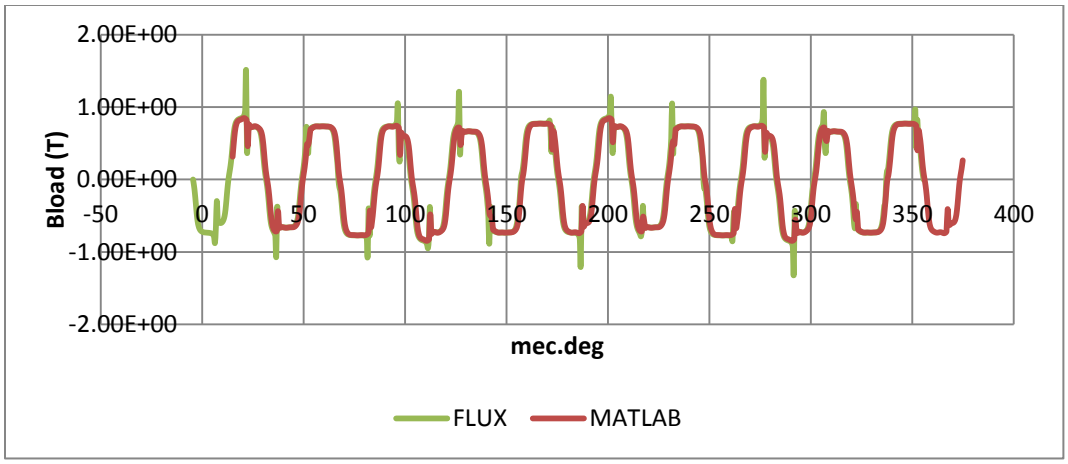

Figure 29 Comparison of load magnetic field at the initial position

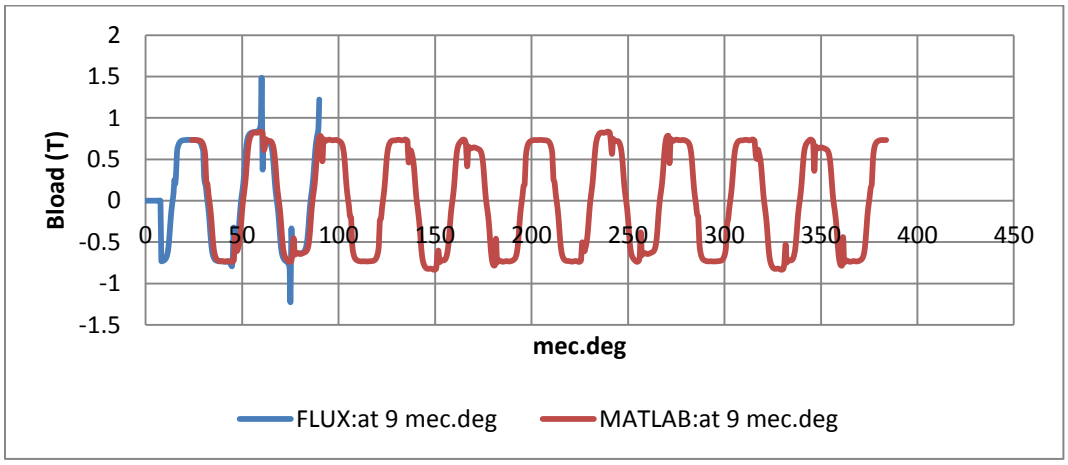

Figure 30 Comparison of load magnetic field at 9 mec.deg

2.1.4 Calculation of magnetic field in stator teeth and yoke

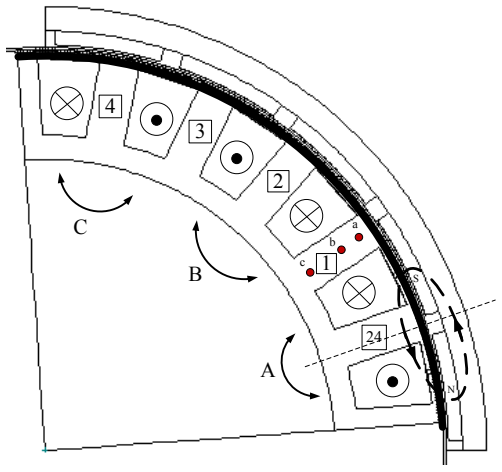

Figure 31 Motor cross section with teeth numbered

According to [49], the tooth flux is given by the integral of the flux density over one slot pitch and axial motor length,

$$\phi_t(t) = \int_{-\frac{L_{stk}}{2}}^{\frac{L_{stk}}{2}} \int_{-\frac{\alpha_s}{2}}^{\frac{\alpha_s}{2}} B_{load}(\alpha, R_s, t) R_s d\theta dz \tag{2.40}$$

Where,

L_{stk}, is the axial length of the motor,

α_s, is the slot angular pitch, mec.rad,

R_s, is the surface radius of stator,

t, is time.

It can be proved that the magnetic field in each stator tooth is the same but is delayed by the slot angular pitch. Thus, the flux in the kth tooth is given by

$$\phi_{tk}(w_e t) = \phi_t(w_e t - (k-1)\theta_s) \tag{2.41}$$

for k=1,2,…,Q_s.

Assuming the tooth flux spreads uniformly within the tooth, the tooth flux density can be given by

$$B_{tn}(w_e t) = \frac{\phi_{tk}(w_e t)}{K_{st} L_{stk} w_{st}} \tag{2.42}$$

Where,

K_{st}, is the lamination stacking factor,

L_{stk}, is the axial motor length,

w_{st}, is the tooth width,

w_e, is the electric angular velocity, is equal to $2\pi f$, f is the frequency.

The same model is used to calculate the magnetic field in stator tooth as shown in Figure 31. The stator teeth are numbered. The input parameters are still the same as in Table 7. The initial position of rotor is shown in Figure 26. Namely, the axis of phase A is in line with q-axis. The comparison of the flux density amplitude in No.1 stator tooth between analytical and FEA results is shown in Figure 33. In FEA, three points a, b, c are sampled. Their locations are labeled in Figure 31. It demonstrates that the average amplitude of flux density at tooth tip is higher than that at tooth center. The amplitude of flux density at tooth bottom is slightly lower than that at

tooth center. This is caused by the infinite permeability of stator lamination. Particularly at tooth tips, the magnet flux is linked with tooth tips without entering tooth body when No.1 tooth is at the center of two magnets gap as shown in Figure 32. In another case, when No.1 tooth is at the center of one magnet, the flux density amplitude of point a is a bit lower than that of point b because the tooth tip shunts the flux passage. The analytical result is closer to the FEA result at point b.

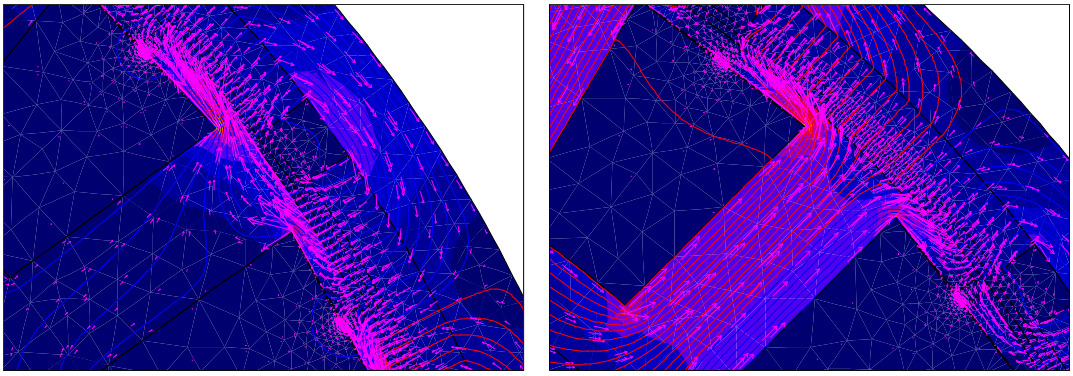

Figure 32 FEA results

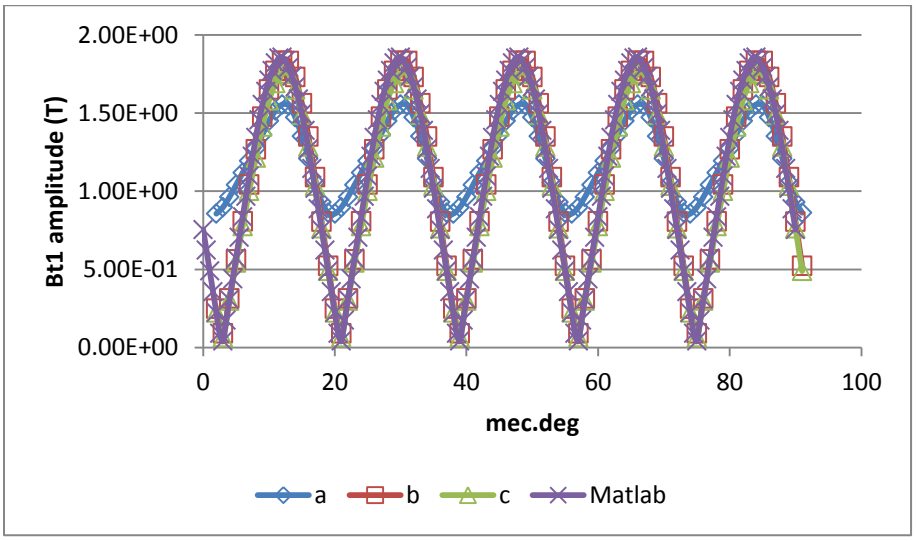

Figure 33 Stator tooth flux density variation in No.1 tooth

Based on the flux calculation of each stator tooth as in (2.41), the flux passing through the stator yoke segment between teeth can be calculated.

The flux in the stator yoke between tooth No.2 and No.1 is given by the weighted average

$$\phi_{j21}(w_e t) = \frac{1}{Q_s}\sum_{k=1}^{Q_s-1}(Q_s - k)\phi_{t(k+1)}(w_e t) \tag{2.43}$$

$$\phi_{j(k+1)k} = \phi_{jk(k-1)} - \phi_{tk} \tag{2.44}$$

Assuming the flux spreads uniformly across the stator yoke cross section, the yoke flux density can be given by

$$B_{jn} = \frac{\phi_{jn}}{K_{st} L_{st} h_{sj}} \tag{2.45}$$

Where h_{sj} is the stator yoke width.

The comparison between analytical and FEA results are shown in Figure 34. The amplitude of yoke flux density in the first yoke segment between No.2 tooth and No.1 tooth as well as in the second yoke segment between No.3 tooth and No.2 tooth is calculated. It indicates that the flux density distribution of stator yoke is different from that of stator tooth, which repeats the same shape in every tooth but one slot pitch delayed. The shape of stator yoke flux density repeats in every other yoke segment and has two different amplitudes.

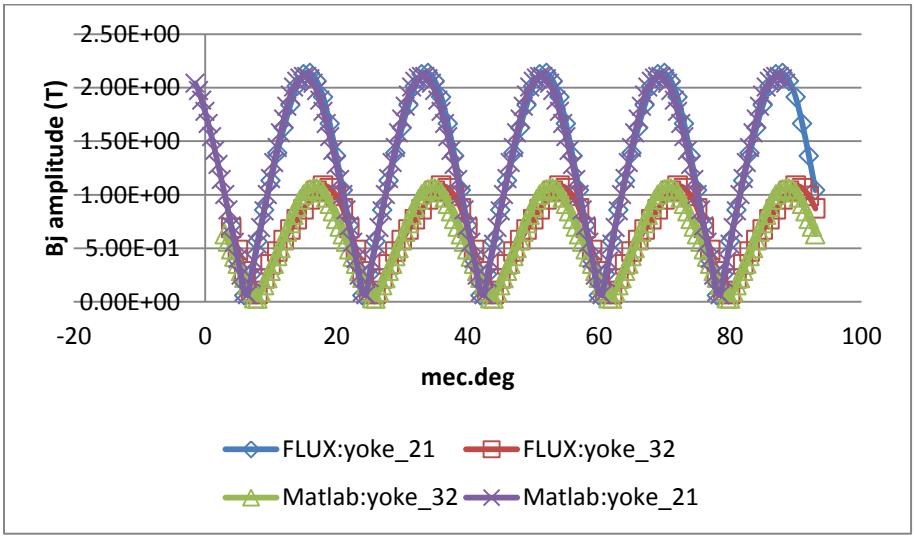

Figure 34 Stator yoke flux density variation in the first and second segments of stator yoke

2.2 Phase inductance calculation

The phase inductance of SPM motor is composed of three components: airgap inductance, slot-leakage inductance and end-turn inductance [53].

$$L_{ph} = L_g + L_{slot} + L_{end} \tag{2.46}$$

Where,

L_g, is the airgap inductance,

L_{slot}, is the slot-leakage inductance,

L_{end}, is the end-turn inductance.

2.2.1 Calculation of air gap inductance

The armature reaction flux density in the air gap is given by

$$B_{ga}=\frac{\mu_0 NI}{g'} \tag{2.47}$$

Where,

$\mu_0 = 4\pi \times 10^{-7}\mathrm{H/m}$,

N, is the number of turns in the coil,

I , is the input phase current,

The equivalent air gap length is given by

$$g' = K_c g + \frac{L_M}{\mu_r} \tag{2.48}$$

Where,

L_M, is the thickness of magnet,

μ_r, is the relative recoil permeability of magnet.

g, is the actual airgap length modified for slotting by Carter's coefficient K_c. An approximation for K_c suitable for surface magnet motors is

$$K_c = \frac{5+s}{5+s-\frac{s^2 g}{\lambda}} \tag{2.49}$$

$$s = \frac{w_{so}}{g} \tag{2.50}$$

$$\lambda = \frac{2\pi R_m / Q_s}{g} \tag{2.51}$$

Where,

w_{so}, is the slot opening as shown in Figure 18,

R_m, is magnet inner radius for outer-rotor motor,

Q_s, is slot number.

For equal-width tooth, the flux linkage of the coils in one phase is

$$\psi = N_m N B_{ga} \frac{2\pi R_m}{Q_s} L_{stk} \tag{2.52}$$

Where, N_m is the number of series coils in one phase.

Thus, the airgap inductance is calculated as

$$L_g = N_m N^2 \frac{2\pi R_m \mu_0 L_{stk}}{g' Q_s} \tag{2.53}$$

For unequal-width tooth, the slot pitch is nearly equal to pole pitch, thus,

$$w_{s1} = \frac{2\pi R_m}{2p} \tag{2.54}$$

Therefore, the flux linkage of the coils in one phase is

$$\psi = N_m N B_{ga} (w_{s1} + w_{so}) L_{stk} \tag{2.55}$$

The airgap inductance is

$$L_g = N_m N^2 \frac{\mu_0 L_{stk}}{g'} (\frac{2\pi R_m}{2p} + w_{so}) \tag{2.56}$$

2.2.2 Calculation of slot-leakage inductance

The slot-leakage inductance is calculated from slot dimensions as presented in Figure 18.

$$L_{slot} = 2N_m N^2 (\frac{\mu_0 d_s L_{stk}}{3w_{sb}} + \frac{\mu_0 d_t L_{stk}}{(w_{so} + w_{sb})/2} + \frac{\mu_0 d_{sh} L_{stk}}{w_{so}}) \tag{2.57}$$

2.2.3 Calculation of end-turn inductance

For outer rotor motor,

$$L_e = 2N_m \mu_0 \frac{2\pi(R_m - g)}{Q_s} \frac{N^2}{4} \mathrm{Ln}(\frac{\pi(R_m - g)}{Q_s} \sqrt{\frac{\pi}{S_{Cu}}}) \tag{2.58}$$

Where, S_{Cu} is the coil area in one slot.

During motor design procedure, when considering flux-weakening ability as well as fault-tolerant ability, which will be discussed in the next section, the expected phase inductance is sometimes required bigger than the value given by

$$L_d = \frac{\psi_{1Md}}{I_m} \tag{2.59}$$

Where,

I_m, is the rms value of maximum phase current, A,

ψ_{1md}, is the rms value of fundamental magnet flux linkage, V-s (rms).

For example, assuming

$$\psi_{1Md} = \frac{k_{wp}N_m \times N}{\sqrt{2}} \frac{\widehat{B_{g1}} D L_{stk}}{p} = \frac{0.966 \times 4 \times 1}{\sqrt{2}} \frac{0.74 \times 0.342 \times 0.08}{10} = 5.565\text{e}-3\ \text{V.s}$$

$$I_m = \frac{I_p}{\sqrt{2}} = \frac{724.45}{\sqrt{2}} = 512.34\ \text{A}$$

Then the expected phase inductance is

$$L_d = \frac{\psi_{1Md}}{I_m} = 10.86\ \mu\text{H}$$

Thus, by adjusting relative slot dimensions and motor dimensions the expected phase inductance can be reached.

2.3 Torque-speed characteristic

With the help of d-q theory, the phasor diagram illustrating the fundamental principle of operating salient-pole machine is drawn in Figure 35. For SPM motor,

$$L_d = L_q = L_{dq} \tag{2.60}$$

where, L_d and L_q are the d, q inductances. As for embedded internal permanent magnet motor (IPM), d and q inductances are not the same. SPM and IPM drives have some similarities. [54], [55] made a comparison between SPM and IPM drives for electric vehicle.

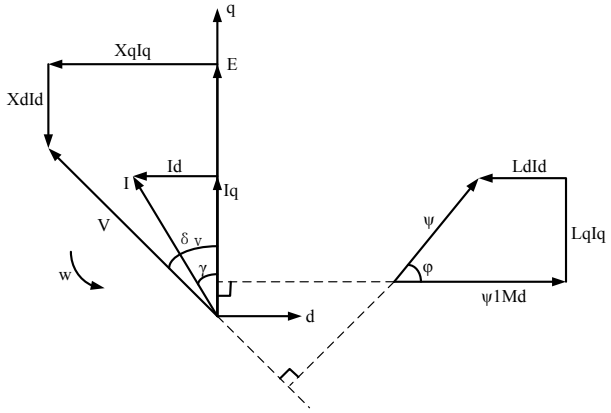

Figure 35 Phasor diagram

Corresponding to Figure 35, the relations can be obtained as following,

Voltage equations:

$$u_d = \frac{d\Psi_d}{dt} - \omega\Psi_q + Ri_d \tag{2.61}$$

$$u_q = \frac{d\Psi_q}{dt} + \omega\Psi_d + Ri_q \tag{2.62}$$

Flux-linkage equations:

$$\Psi_d = \Psi_{1Md} + L_d I_d \tag{2.63}$$

$$\Psi_q = L_q I_q \tag{2.64}$$

The time-average torque and power equations:

$$T_e = mp\left(\Psi_d I_q - \Psi_q I_d\right) = mp(\Psi_{1Md} I_q + I_d I_q (L_d - L_q)) \tag{2.65}$$

$$P_{input} = u_d i_d + u_q i_q \tag{2.66}$$

Current equations:

$$I_d^2 + I_q^2 = I^2 \tag{2.67}$$

$$I_d = -I sin\gamma \tag{2.68}$$

$$I_q = I cos\gamma \tag{2.69}$$

Furthermore,

$$T_e = mp(\Psi_{1Md} I cos\gamma - I^2 sin\gamma cos\gamma (L_d - L_q)) \tag{2.70}$$

Where,

T_e, is the electromagnetic torque,

m, is the phase number,

p, is the number of pole pairs,

Ψ_d, and Ψ_q are the d, q components of flux linkage,

I , is rms value of input phase current,

I_d and I_q are the d, q components of current, $I_d < 0$,

γ, is the current advanced angle,

Ψ_{1Md}, is the rms fundamental flux linkage due to the magnet,

$$\Psi_{1Md} = k_{wp} T_{ph} \Phi_{1Md} = \frac{k_{wp} T_{ph}}{\sqrt{2}} \frac{\widehat{B_{g1}} D L_{stk}}{p} \text{Vs. rms} \tag{2.71}$$

Without considering resistance and losses the voltage phasor is given by

$$\boldsymbol{V} = V_d + jV_q = j\omega \boldsymbol{\Psi} = -\omega \Psi_q + j\omega \Psi_d = -X_q I_q + j(E + X_d I_d) \tag{2.72}$$

Namely,

$$I_d = \frac{V_q - E}{X_d} = \frac{V_m cos\delta_v - E}{X_d} \tag{2.73}$$

$$I_q = -\frac{V_d}{X_q} = \frac{V_m sin\delta_v}{X_q} \tag{2.74}$$

Thus,

$$(X_q I_q)^2 + (E + X_d I_d)^2 = V_m^2 \tag{2.75}$$

or

$$w\sqrt{(L_q I_q)^2 + (\Psi_{1Md} + L_d I_d)^2} = V_m \tag{2.76}$$

Where,

w, is equal to $2\pi f$,

V_d and V_q are the d, q components of voltage vector,

$$V_m^2 = V_d^2 + V_q^2 \tag{2.77}$$

V_m, is the voltage limit,

X_d and X_q are the d, q reactances,

$$X_q = wL_q \tag{2.78}$$

$$X_d = wL_d \tag{2.79}$$

δ_v, is the angle between voltage vector and q-axis.

From the equations of (2.67) and (2.75), the current limit and voltage limit circles can be drawn to calculate the curve of torque-speed characteristic. Defining short-circuit current as

$$I_{sc} = \frac{\Psi_{1Md}}{L_d} = \frac{E}{X_d} \tag{2.80}$$

Where,

E, is the back EMF value,

$$E = \frac{\Psi_{1Md}}{w} \tag{2.81}$$

Depending on the location of voltage circle center, two situations are discussed separately [56]. When the short-circuit current I_{sc} is bigger than the current limit I_m, then the voltage circle center is outside the current limit circle. And when the short-circuit current I_{sc} is smaller than the current limit I_m, then the voltage circle center is inside the current limit circle.

2.3.1 In the case of $\boldsymbol{I_m \leq I_{sc}}$

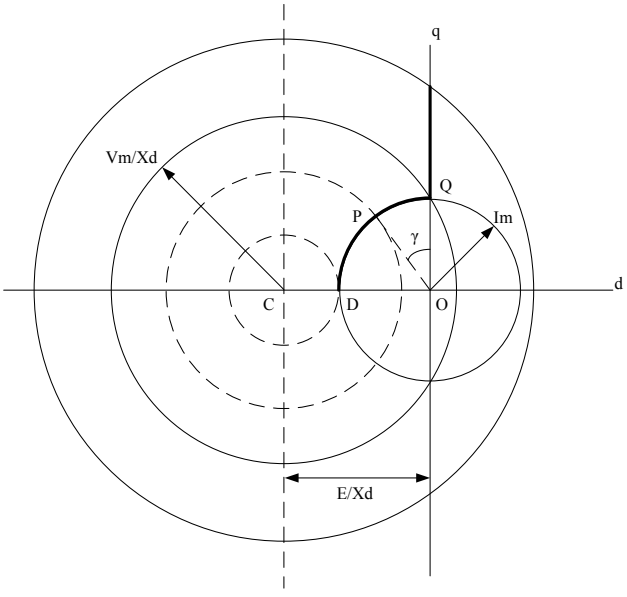

Figure 36 Current limit circle and voltage limit circle

Figure 36 shows the voltage limit circles at four various speed. With speed increasing, the voltage limit circle will shrink. When the voltage circle passing by point Q, the speed is base speed. It means that, higher than this speed, the electromagnetic torque will not be maintained by the certain input voltage, the current is advanced to q-axis, current advanced angle appears, and torque decreases. When voltage circle passing by point D, the theoretical maximum operating speed is approached. By solving the equation group of voltage limit circle and current limit circle, the base speed as in (2.82), current advanced angle as in (2.83) and theoretical maximum speed as in (2.84) can be obtained.

$$w_Q = \frac{V_m}{\sqrt{L_d^2 I_m^2 + \Psi_{1Md}^2}} \tag{2.82}$$

$$\sin\gamma = \frac{V_m^2 - X_d^2 I_m^2 - E^2}{-2EX_d I_m} \tag{2.83}$$

$$w_{max} = \frac{V_m}{\Psi_{1Md} - L_d I_m} \tag{2.84}$$

In order to simplify the problem, variables are often normalized. The base values are chosen as following,

$$I_b = I_{d(sc)} = \frac{\Psi_{1Md}}{L_d} \tag{2.85}$$

$$V_b = E_0 = w_0 \Psi_{1Md} \tag{2.86}$$

$$Z_b = \frac{V_b}{I_b} = w_0 L_d \tag{2.87}$$

$$w_b = w_0 \tag{2.88}$$

$$\Psi_b = \Psi_{1Md} \tag{2.89}$$

$$T_b = mp\Psi_b I_b \tag{2.90}$$

Where, w_0 is the base electrical angular velocity.

Therefore, the normalized forms of equations are

$$\Omega = \frac{w}{w_0} \tag{2.91}$$

$$x_d = \frac{X_d}{Z_b} = \Omega \tag{2.92}$$

$$x_q = \frac{X_q}{Z_b} = \xi\Omega \tag{2.93}$$

$$i_m = \frac{I_m}{I_b} \tag{2.94}$$

$$e = \frac{E}{V_b} = \Omega \tag{2.95}$$

$$v_d = \frac{V_d}{V_b} = -\xi \Omega i_q \tag{2.96}$$

$$v_q = \frac{V_q}{V_b} = \Omega(1 + i_d) \tag{2.97}$$

$$\tau = \frac{T_e}{T_b} = icos\gamma[1 + (\xi - 1)isin\gamma] \tag{2.98}$$

Where, ξ is the salience ratio,

$$\xi = \frac{L_q}{L_d} \tag{2.99}$$

For SPM motor,

$$\xi = 1 \tag{2.100}$$

With normalized format, the input current and output torque can be calculated at different operating points. When the speed is less than or equal to the base speed, viz at the operating point above Q along the q-axis or at Q, the input current and output torque are

$$i = i_m \tag{2.101}$$

$$\tau = i = i_m \tag{2.102}$$

The limit voltage v_m required at w_0 is, namely when $\Omega = 1$ at which speed $\tau = i_m$ can be maintained,

$$\Omega_Q = \frac{v_m}{\sqrt{i_m^2 + 1}} = 1 \tag{2.103}$$

$$v_m = \sqrt{i_m^2 + 1} \tag{2.104}$$

When the speed is bigger than base speed, like at the operating point of P,

$$\tau = i_m \cos\gamma \tag{2.105}$$

$$\xi^2 i_q^2 + (1 + i_d)^2 = \frac{v_{m^2}}{\Omega^2} = \psi^2 \tag{2.106}$$

$$i_d = -i_m \sin\gamma \tag{2.107}$$

$$i_q = i_m \cos\gamma \tag{2.108}$$

The current advanced angle to get the maximum output torque can be deduced,

$$\sin\gamma = \frac{1 + i_m^2 - \psi^2}{2i_m} \tag{2.109}$$

Which indicates for a certain ψ there exists the maximum torque τ when the current limit is reached. That is

$$\tau_{MAX} = \frac{1}{2}\sqrt{4i_m^2 - (1 + i_m^2 - \psi^2)^2} \tag{2.110}$$

At operating point of D, when the theoretical maximum speed is approached,

$$i_d = -i_m \tag{2.111}$$

$$\tau = i_q = 0 \tag{2.112}$$

$$\Omega_{max} = \frac{v_m}{1 - i_m} \tag{2.113}$$

2.3.2 In the case of $\boldsymbol{I_m > I_{sc}}$

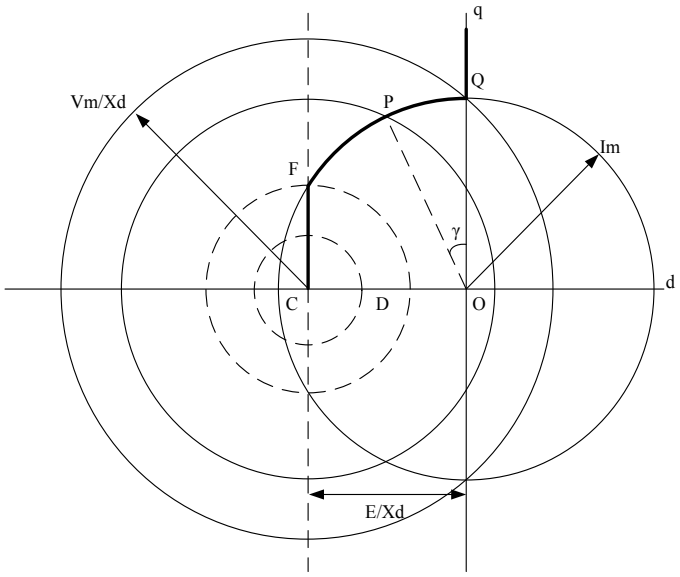

Figure 37 Current limit circle and voltage limit circle

When the short-circuit current is less than the limit current, the voltage circle center is inside the current limit circle as shown in Figure 37. In this case, another operating point F appears to

implement maximum torque per voltage (MTPV) control in the high-speed region. When the speed is less than the speed at the operating point F, the input current and output torque are the same like the discussion in previous section. When the speed gets into the high-speed region, meaning the voltage circle passing by the point F, the operation trajectory starts along the line F-C. In addition, the theoretical maximum speed is infinite.

At the operating point F, it is easy to get

$$\left(\frac{V_m}{X_d}\right)^2 + \left(\frac{E}{X_d}\right)^2 = I_m^2 \tag{2.114}$$

Thus, it can be deduced that

$$w_F = \frac{V_m}{L_d\sqrt{I_m^2 - \left(\frac{\Psi_{1Md}}{L_d}\right)^2}} \tag{2.115}$$

The normalized format is

$$\Omega_F = \frac{v_m}{\sqrt{i_m^2 - 1}} \tag{2.116}$$

Along the operation trajectory F-C, namely when $w > w_F$

$$I = \sqrt{\left(\frac{V_m}{X_d}\right)^2 + \left(\frac{E}{X_d}\right)^2} \tag{2.117}$$

$$\tan\gamma = \frac{E}{V_m} \tag{2.118}$$

The normalized format is

$$i = \sqrt{\left(\frac{v_m}{\Omega}\right)^2 + 1} = \sqrt{\psi^2 + 1} \tag{2.119}$$

$$\tan\gamma = \frac{\Omega}{v_m} \tag{2.120}$$

In conclusion, based on the aforementioned discussion, for different regions of motor speed, the requested input current and the calculated output torque are summarized in Table 9 with normalized form.

Table 9 Input current and output torque in normalized form

	Above Q and at Q Constant-torque region MTPA control	Q-F Flux-weakening region FW control	F-C Maximum output power control MTPV control
i	i_m	i_m	$\sqrt{\psi^2+1}$
i_q	i_m	$\sqrt{i_m^2-\left(\frac{1+i_m^2-\psi^2}{2}\right)^2}$	ψ
i_d	0	$-\frac{1+i_m^2-\psi^2}{2}$	1
γ	0	$\mathrm{asin}(\frac{1+i_m^2-\psi^2}{2i_m})$	$\mathrm{atan}(\frac{1}{\psi})$
τ	i_m	$\sqrt{i_m^2-\left(\frac{1+i_m^2-\psi^2}{2}\right)^2}$	ψ

Following is an example to analyze the torque-speed characteristic of an external-rotor SPM motor. The input parameters are shown in Table 10. From the output it can be seen the requested phase rms voltage which can maintain the torque 119Nm at 667 rpm is 29.2V. The short circuit current is less than the maximum phase current meaning the voltage limit center is inside the current limit center. There will be three speed regions including constant-torque region, flux-weakening region and maximum-output-power region. The speed at the operating point F as shown in Figure 37 Current limit circle and voltage limit circleFigure 37 is 1251rpm. Figure 38 compares the torque-speed profile of $i_d = 0$ control and flux-weakening control. Figure 39 shows the variation of input current versus speed. From the curve of i_d, the three speed regions can be observed. Figure 40 shows the increasing of current advanced angle and Figure 41 shows the variation of power factor.

Table 10 Input parameters

Phase number, m	3
Pole pairs, p	10
Slot number, Q_s	24
Stator outer diameter, D	282 mm
Lamination length, L_{stk}	30 mm
Airgap peak flux density, B_g	0.863 T
Magnet pole arc, α_M	160 elec.deg
Turns per coil, N_s	10
Base speed at point Q, nN	667
Maximum peak current, I_{pm}	224.29 A
d-axis inductance, L_d	0.211 mH

Table 11 Output parameters

Phase rms voltage, V_m	29.2 V
Short-circuit peak current, I_{sc}	167.48 A
Ratio of I_{pm} to I_{sc}, i	1.34
Speed at point F of FW control	1251
Maximum speed of $i_d = 0$ control	1114

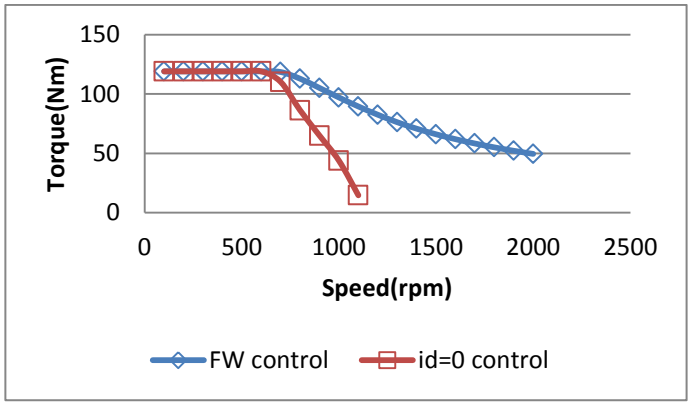

Figure 38 Torque-speed characteristic

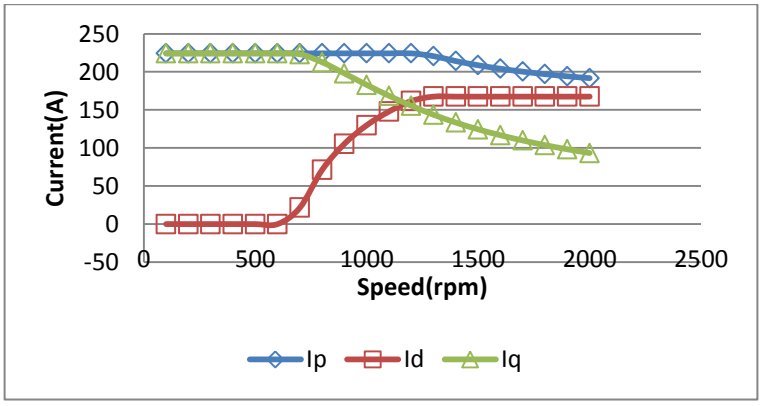

Figure 39 Input current versus speed

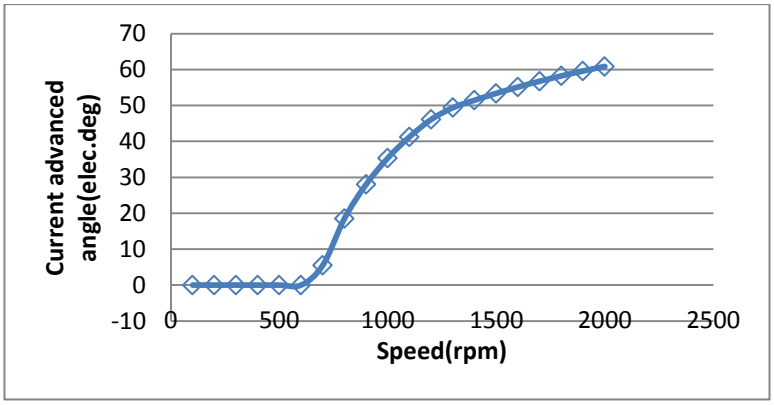

Figure 40 Current advanced angle

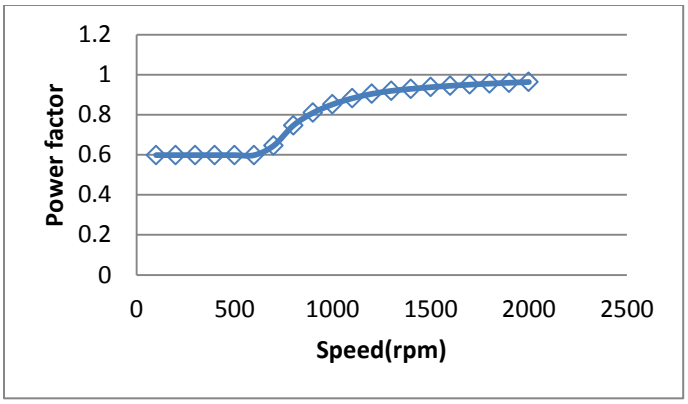

Figure 41 Power factor

2.4 Control strategy

In last section, the maximum possible electromagnetic torque is calculated at a certain speed. However, when the requested load torque is lower than the maximum torque at a certain speed, what is the reference value of input current and the current advanced angle? This problem will be discussed in this section.

2.4.1 Constant torque-angle control

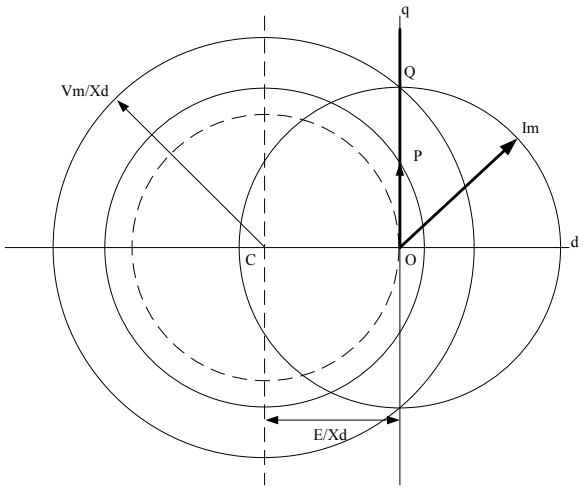

Figure 42 Constant torque-angle control

The current vector is always in line with q-axis. The advanced current angle is zero and the normalized value of current is equal to that of the requested torque.

$$i = i_q = \tau \tag{2.121}$$

$$i_d = 0 \tag{2.122}$$

$$\gamma = 0 \tag{2.123}$$

With speed increasing, the operating trajectory goes along Q-O, the torque will decrease to 0 until the point O is reached. Then the maximum speed is

$$\Omega_{max} = v_m \tag{2.124}$$

2.4.2 Direct flux-weakening control

In this control strategy, the value of i_d reference is only decided by the speed Ω. i_d has a fixed value for a certain speed. However, the value of i_q will change with the torque request [57].

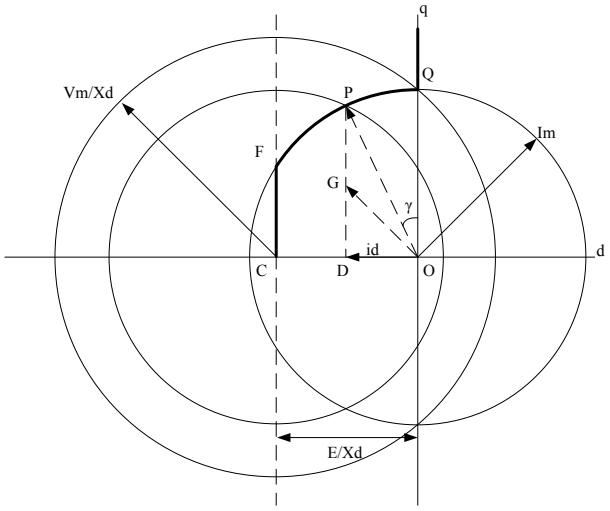

Figure 43 Direct flux-weakening control

From point Q to F, for a certain speed Ω, the value of i_d is fixed. That is

$$i_d = i_m sin\gamma = i_m \frac{1 + i_m^2 - \psi^2}{2i_m} = \frac{1 + i_m^2 - \psi^2}{2} \tag{2.125}$$

where,

$$\psi = \frac{v_m}{\Omega} \tag{2.126}$$

From F to C, the value of i_d is

$$i_{d(\Omega)} = 1 \tag{2.127}$$

In both sections, the value of i_q is always equal to τ,

$$i_q = \tau \tag{2.128}$$

2.4.3 Indirect flux-weakening control

In this flux-weakening control strategy, the value of i_d reference is decided not only by the speed Ω but also by the torque request τ. Although i_q will also change with torque request and

both the values of i_d, i_q are coupled with torque, the value of ψ is always fixed for a certain speed. Taking advantage of this point, the d, q components of current can be solved.

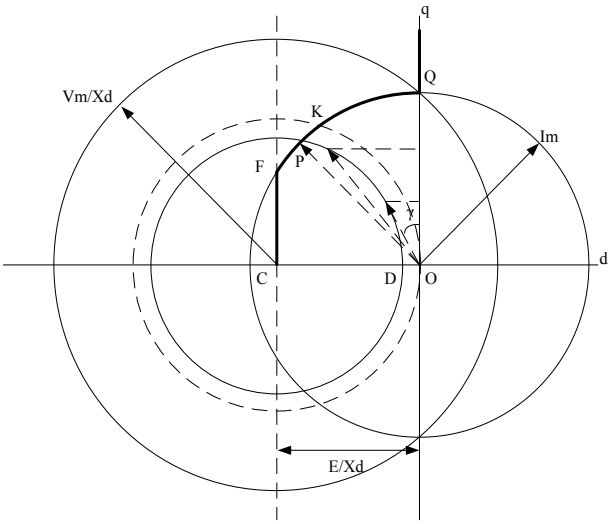

Figure 44 Indirect flux-weakening control

From K to C,

$$i_q = \tau \tag{2.129}$$

Because,

$$i_q^2 + (1 + i_d)^2 = \frac{v_{m^2}}{\Omega^2} = \psi^2 \tag{2.130}$$

Then,

$$i_d = \sqrt{\psi^2 - \tau^2} - 1 \tag{2.131}$$

To summarize, Table 12 lists the requested input current of different control strategies based on the normalized value of requested torque.

Table 12 Requested input current of different control strategies

	i_d	i_q
Constant toque-angle control	0	τ
Direct FW control	From Q to F: $i_d = \frac{1 + i_m^2 - \psi^2}{2}$ From F to C: $i_d = 1$	τ
Indirect FW control	From Q to C: $i_d = \sqrt{\psi^2 - \tau^2} - 1$	τ

2.5 Losses calculation

Three main losses are taken into account: stator copper loss, stator core loss and rotor magnet loss.

2.5.1 Copper loss

The copper loss is given by

$$P_{Cu} = \rho_{Cu} Vol_{Cu} J^2 \tag{2.132}$$

where ρ_{Cu} is the copper electric resistivity, Vol_{Cu} is the volume of copper.

From the section of 1.2.2, the copper loss is

$$P_{Cu} = \frac{\frac{\rho_{Cu}}{k_{fill}}(L_{stk} + L_{ew})\left(\frac{K_{sp}\pi D}{\sqrt{2}k_{wp}}\right)^2}{\frac{\pi}{4}\left(D^2 - \left(D_i + \frac{B_g \pi D}{B_{sj} 2pK_{Fe}}\right)^2\right) - \frac{B_g \pi D}{B_{st}}\left(\frac{D - D_i}{2} - \frac{B_g \pi D}{4 B_{sj} p K_{Fe}}\right)} \tag{2.133}$$

Where,

ρ_{Cu}, is the copper electrical resistivity, Ω. m,

L_{ew}, is the end-winding length, m,

k_{wp}, is the fundamental winding factor.

Because K_{sp} is proportional to phase current I_p, it is obvious copper loss is proportional to I_p^2. Besides, it points out that the combination of slot and pole numbers influence the value of copper loss through winding factor. Figure 45 is an example of copper loss calculation. Starting from the input shown in Table 13, it shows the impact on copper loss by different combinations of slots and poles [58]. This could be a reference to select reasonable slot and pole numbers when there is definite requirement on copper losses during motor design.

Table 13 Input parameters for copper loss comparison

D	282mm
D_i	180mm
L_{stk}	30mm
k_{fill}	45%
K_{Fe}	0.98
B_g	0.863 T
B_{sj}	1.391 T
B_{st}	1.5 T
ρ_{Cu}	1.72e-8 Ω. m
K_{sp}	7.34e4 A/m

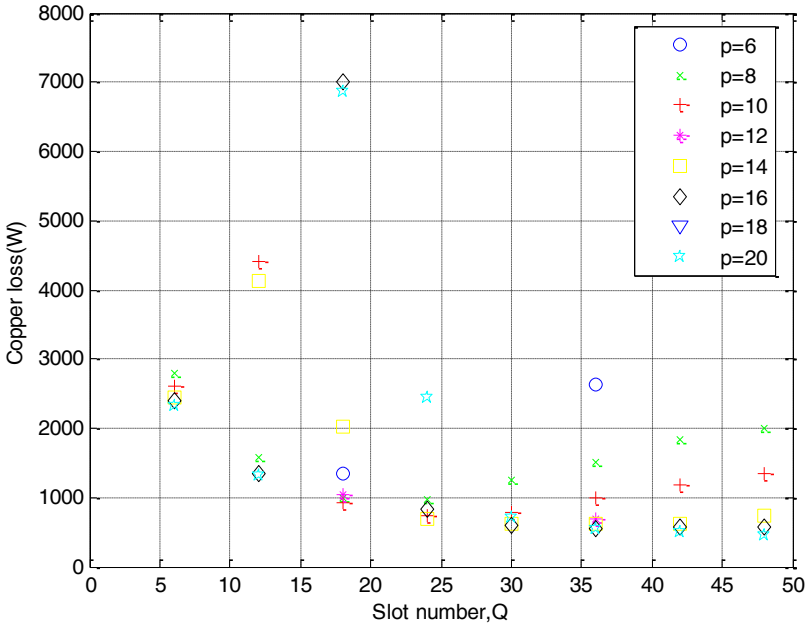

Figure 45 Copper loss of different combinations of slot and pole

2.5.2 Iron loss

Stator core loss is divided into tooth core loss and yoke core loss. Each core loss is the sum of hysteresis loss and induced eddy current loss. There are four methods to calculate iron loss [59], [60].

2.5.2.1 Modified Steinmetz equation

The first one is Modified Steinmetz equation [61–63]. Assuming trapezoidal transition within the tooth and ignored fringing effect, the specific tooth core loss (W/kg) is calculated.

When tooth electric angle $\alpha_{TT} \leq \pi - 2p\alpha_{pm}$,

$$p_{Fe}(B_t) = C_h f B_t^{a+bB_t} + \frac{4}{\pi}\frac{f^2 B_t^2 C_e}{\alpha_{TT}} \tag{2.134}$$

When $\alpha_{TT} > \pi - 2p\alpha_{pm}$,

$$p_{Fe}(B_t) = C_h f B_t^{a+bB_t} + \frac{4}{\pi}\frac{f^2 B_t^2 C_e}{\alpha_{TT}}[2 - \frac{\pi - 2p\alpha_{pm}}{\alpha_{TT}}] \tag{2.135}$$

Where,

f, is the frequency, Hz,

C_h, a, b are hysteresis loss coefficients,

C_e is the eddy loss coefficient. They could be extracted from the manufacture data of lamination [64].

For the yoke part, the specific core loss is

$$p_{Fe}(B_j) = C_h f B_j^{a+bB_j} + \frac{8}{\pi}\frac{f^2 B_j^2 C_e}{2p\alpha_{pm}} \tag{2.136}$$

2.5.2.2 Based on the stator magnetic field

In the section of 2.1.4, the waveforms of flux density in stator tooth and yoke have been investigated over one revolution of the rotor. Based on the waveforms, the looses in stator tooth and yoke are determined by

$$P_{Fe-st} = Vol_{st}\rho_{Fe}K_{Fe}\left\{k_h B_t^2 f + \left[\frac{1}{T}\int_0^T k_e\left(\frac{dB_t}{dt}\right)^2 dt\right] + \left[\frac{1}{T}\int_0^T k_{exc}\left(\frac{dB_t}{dt}\right)^{\frac{3}{2}} dt\right]\right\} \tag{2.137}$$

$$P_{Fe-sj} = Vol_{sj}\rho_{Fe}K_{Fe}\left\{k_h B_j^2 f + \left[\frac{1}{T}\int_0^T k_e\left(\frac{dB_j}{dt}\right)^2 dt\right] + \left[\frac{1}{T}\int_0^T k_{exc}\left(\frac{dB_j}{dt}\right)^{\frac{3}{2}} dt\right]\right\} \tag{2.138}$$

Where,

Vol_{st}, is the volume of stator tooth as calculated in the section of 1.2.2,

Vol_{sj}, is the volume of stator yoke as calculated in the section of 1.2.2,

ρ_{Fe}, is the mass density of stator lamination, $\mathrm{kg/m^3}$,

B_t and B_j are the waveforms of flux density in stator tooth and yoke as discussed in 2.1.4,

k_h, is the hysteresis loss coefficient, $\mathrm{Ws/(T^2 m^3)}$,

k_e, is the eddy current loss coefficient, which is equal to $(\sigma d^2)/12$,

σ, is the electrical conductivity of lamination, S/m,

d, is the thickness of lamination, m,

k_{exc}, is the additional loss coefficient, $\mathrm{W/((Ts^{-1})^{3/2}\, m^3)}$,

K_{Fe}, is the lamination factor.

k_h, k_e and k_{exc} are the coefficients which can be extracted from the manufacture datasheet of the lamination.

2.5.2.3 Iron losses calculation in FEA

Core loss is also calculated in FLUX 2D to make a comparison, where Bertotti's theory is adopted.

$$p_{Fe}(B_m) = K_{Fe}[k_h B_m^2 f + \frac{\pi^2 \sigma d^2}{6}(B_m f)^2 + k_{exc}(B_m f)^{\frac{3}{2}} \cdot 8.67] \quad (2.139)$$

Where,

p_{Fe}, is the specific core loss, W/kg

B_m, is the peak value of flux density, T.

Finally, the stator core loss is expressed as

$$P_{Fe} = \rho_s\left(p_{Fe}(B_t)Vol_{st} + p_{Fe}(B_j)Vol_{sj}\right) \quad (2.140)$$

2.5.2.4 Equivalent circuit with iron losses resistance

The second method is to use equivalent circuit of PM motors considering iron losses [65], [66]. The calculation of iron loss is based on no-load iron loss. From the equations of (2.61), (2.62), (2.63) and (2.64), it can be deduced that

$$u_d = \frac{d\Psi_d}{dt} - \omega L_q I_q + R i_d \quad (2.141)$$

$$u_q = \frac{d\Psi_q}{dt} + \omega \Psi_{1Md} + \omega L_d I_d + R i_q \quad (2.142)$$

When considering iron loss resistance, the equivalent circuits are drawn in Figure 46 and Figure 47.

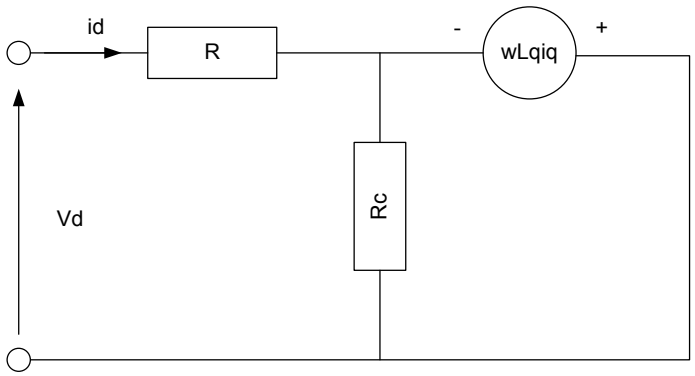

Figure 46 d-axis equivalent circuit

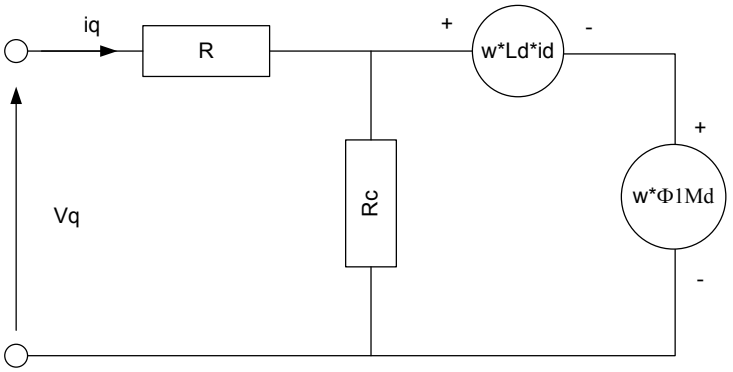

Figure 47 d-axis equivalent circuit

Therefore, neglecting the stator resistance, the iron losses are given by

$$P_{Fe} = \frac{u^2}{R_c} = \frac{u_d^2 + u_q^2}{R_c} = \frac{\omega^2}{R_c}[(\Psi_{1Md} + L_d I_d)^2 + \left(L_q I_q\right)^2] \tag{2.143}$$

The iron loss resistance is composed by three components in parallel: hysteresis losses, eddy current losses and excess losses. Defining the no-load base-speed iron loss resistance as R_{c0}, its three components R_{ch0}, R_{ce0} and R_{cexc0} can be obtained by

$$R_{ch0} = \frac{u_{rate}^2}{P_{Fe-hys0}} \tag{2.144}$$

$$R_{ce0} = \frac{u_{rate}^2}{P_{Fe-eddy0}} \tag{2.145}$$

$$R_{cexc0} = \frac{u_{rate}^2}{P_{Fe-exc0}} \tag{2.146}$$

Where,

u_{rate}, is the rated input phase rms voltage,

$P_{Fe-hys0}$, is the no-load hysteresis losses at base speed,

$P_{Fe-eddy0}$, is the no-load eddy current losses at base speed,

$P_{Fe-exc0}$, is the excess losses at base speed.

The iron losses resistances R_{ch}, R_{ce} and R_{cexc} at other speed can be derived as

$$R_{ch} = R_{ch0}(\frac{\omega}{\omega_b}) \tag{2.147}$$

$$R_{ce} = R_{ce0} \tag{2.148}$$

$$R_{cexc} = R_{cexc0}\left(\frac{\omega}{\omega_b}\right)^{0.5} \tag{2.149}$$

Where,

ω, is the electrical angular speed,

ω_b, is the electrical angular base speed.

2.5.2.5 Comparison of the iron loss calculation methods

To compare the iron loss results calculated by these four methods, one 10-pole-pair 24-slot SPM motor is analyzed. The effect of flux weakening in high speed region is also considered [67], [68]. The specification of the prototype is listed in Table 14. The constant torque region could be maintained from 0rpm to 667rpm under the rms phase voltage of 29.2V. From 667rpm, the operation of motor enters flux-weakening region until 1252rpm. After 1252rpm, the MTPV control starts and the current amplitude begins to decrease. The geometry and winding layout of the motor are shown in Figure 48. According to the discussion of 2.1 and from 2.5.2.1 to 2.5.2.4, iron losses are calculated with four different methods. The imposed current and speed as well as result comparison are shown in Table 15 and Figure 49. Theoretically, the result of FEM is the most accurate prediction because it takes the saturation of the operating motor into account, which other three methods do not.

From the results, it can be observed that, first, the method of Modified Steinmetz is the simplest way of calculation. It does not need the information of motor geometry and is suitable to roughly predict the iron losses during preliminary design procedure. However, it considers flux-weakening effect within very limit extent. After base speed, a big error is observed compared with FEM results.

The method of magnetic field needs to know the motor dimensions. Thus it can be used as analytical way of motor analysis. The algorithm considers flux-weakening effect as shown in Figure 50, which can also be observed from Figure 49 after base speed. The drawbacks of this method are the assumptions of ignoring saturation and infinite permeability of laminations.

The finite element method is the most complicated and time-consuming method, it provides the most accurate result. However, the iron losses result can only be obtained in the step of post-process, not real time. It means after the rotor rotating for one revolution the iron losses can be calculated with the waveform of flux density in stator. Therefore, it can be used as more accurate analysis to validate motor design and performance.

The method of equivalent circuit is also proposed in some papers. But the results indicate this method is lack of accuracy especially in flux-weakening region as labeled with dash in Figure 49. The no-load iron loss resistance can be calculated in FEM. Then the iron loss under load at other speed are predicted as shown in Table 16 and Table 17. This method could be suitable for co-simulation between FLUX 2D and other motor drive software like Portunus or Matlab/Simulink.

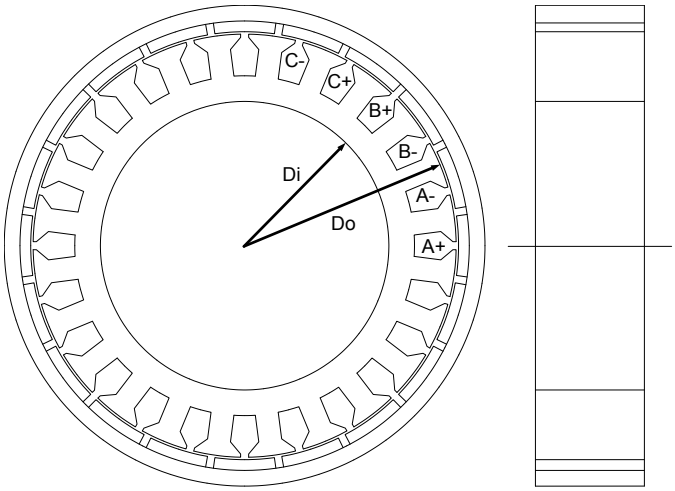

Figure 48 Drawing of a SPM motor

Table 14 Specification of a SPM motor

Pole pairs, p	10
Slot number, Q_s	24
Phase number, m	3
Lamination	M1924
Magnet	NdFeB
Air gap, g (mm)	1
Base speed, nN	667
Magnet arc, α_m(elec.deg)	160
Winding factor, k_w	0.966
Inner diameter of stator, D_i (mm)	180
Out diameter of stator, D (mm)	282
Outermost diameter, D_{ext} (mm)	360
Length of lamination, L_{stk} (mm)	30
Remanence, B_r (T)	1.12
Thickness of magnet, L_m (mm)	4.3
Slot opening, b_0 (mm)	3
Turn-over speed (rpm)	667
Critical speed (rpm)	1252
Phase voltage (V.rms)	29.2

Table 15 Stator iron losses calculated by four different methods (W)

Speed	111 rpm	333 rpm	667 rpm	1000 rpm	1500 rpm
I_p (A)	224.29	224.29	224.29	224.29	188.44
Current advanced angle γ (Elec.deg)	0	0	0	35.38	53.38
Modified Steinmetz equation	6.05	27.49	83.15	155.38	314.68
Magnetic field	4.54	21.56	67.08	105.26	193.85
FEM	7.68	32.24	92.36	132	226.56
Equivalent circuit	8.50	32.31	84.25	71.62	51

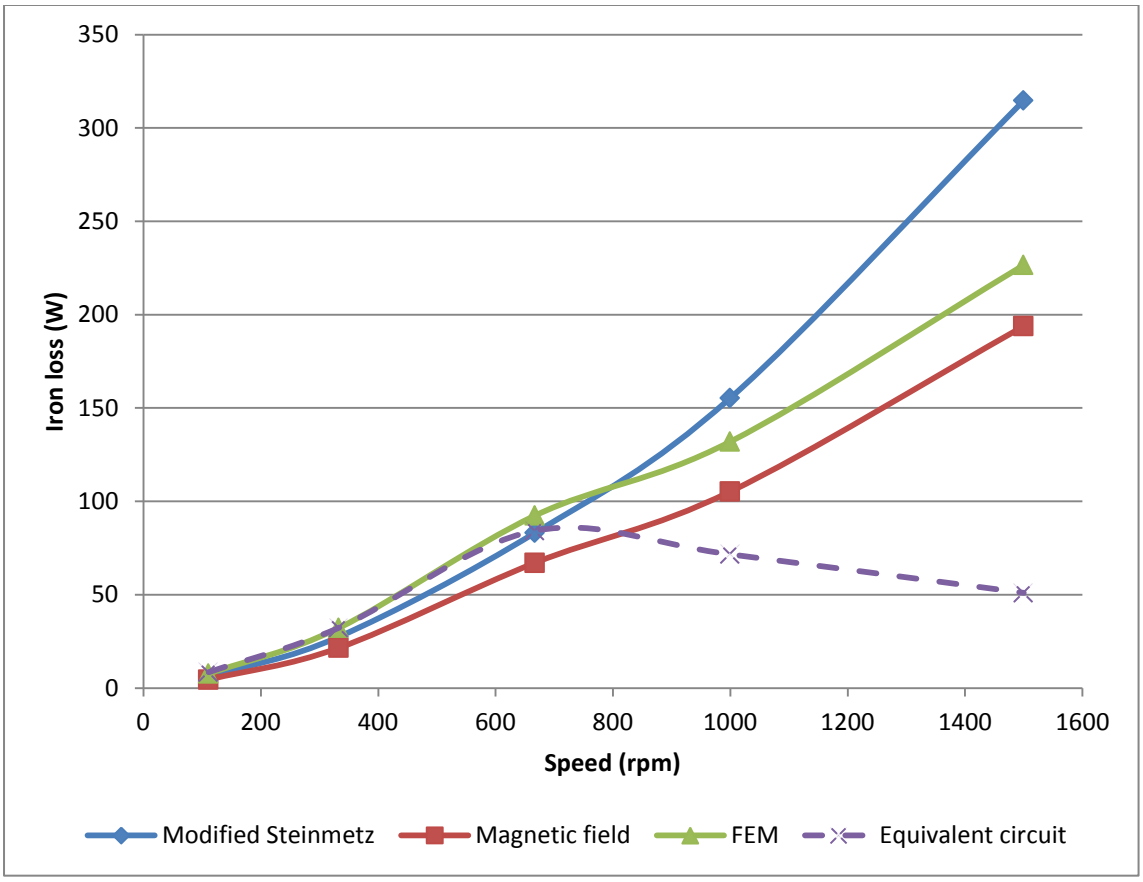

Figure 49 Comparison of iron losses calculated by four different methods

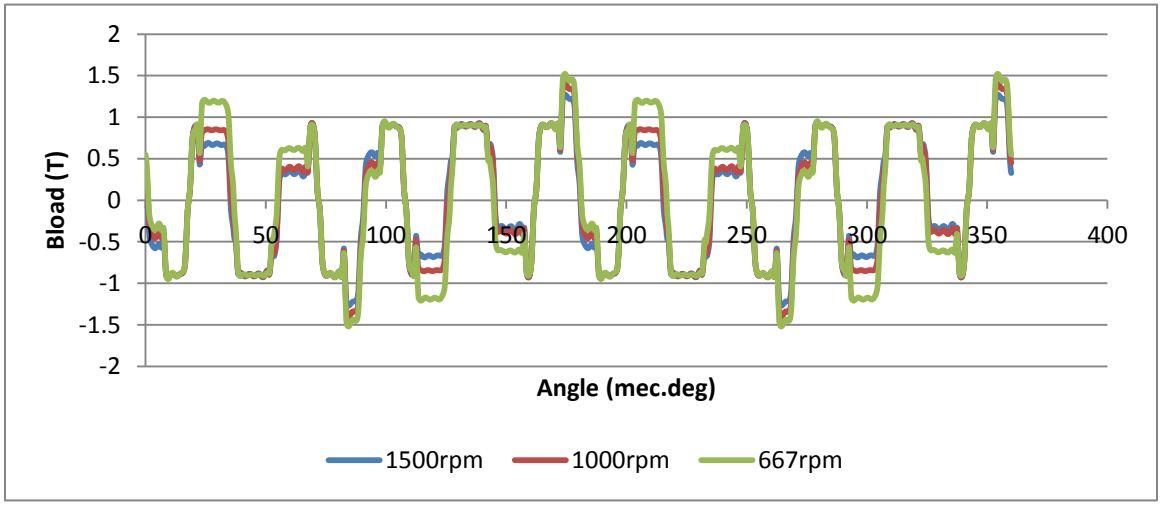

Figure 50 Airgap flux density under flux-weakening operation

Table 16 No-load iron losses at 667rpm

$P_{Fe-hys0}$	$P_{Fe-eddy0}$	$P_{Fe-exc0}$	rms $EMF_{@667rpm}$
10.058W	8.346W	1.568W	16.7V

Table 17 Equivalent iron loss resistances at different speeds

	111	333	667	1000	1500
R_{ch}	3.461	10.382	(R_{ch0}) 20.796	31.179	46.768
R_{ce}	25.062	25.062	(R_{ce0}) 25.062	25.062	25.062
R_{cexc}	54.419	94.256	(R_{cexc0}) 133.398	163.337	200.046
R_c	2.880	6.811	(R_{c0}) 10.473	12.805	15.087

When the motor is running in real condition, the motor losses and efficiency are able to be calculated in real time. Comparing aforementioned four methods of calculating iron losses, Table 18 lists their pros and cons.

Table 18 Comparison of iron losses calculation

	Modified Steinmetz	Magnetic field	FEM	Equivalent circuit
Accuracy	Medium	Better	Best	Worse
Complexity	Easy	Medium	Complicated	Complicated
Application	Motor design	Analytical analysis	FEM analysis	Co-simulation

2.5.3 Magnet loss

There are several models to calculate rotor loss in permanent magnet motor [52], [69–79]. For 3-phase motor, the stator winding is considered as an equivalent current sheet, the linear current density is expressed to the rotor reference frame.

$$K_{sn}(\theta_r, t) = \begin{cases} \sum_n K_{sn}\, cos(np_s\theta_r + (np_s - p)\Omega_m t)\,, for\ n = 3k + k_m \\ -\sum_n K_{sn}\, cos(np_s\theta_r + (np_s + p)\Omega_m t)\,, for\ n = 3k - k_m \\ 0, \qquad for\ n \neq 3k \pm k_m \end{cases} \tag{2.150}$$

Where, K_{sn} is the linear current density for each harmonic,

$$K_{sn} = 6k_{wn}T_{ph}I_p/(\pi D_o) \tag{2.151}$$

k_{wn}, is the winding factor for each harmonic, T_{ph} is the series turns per phase, I_p is the phase current which could be obtained from K_{sp},

p_s, is the fundamental pole pairs of stator winding,

Ω_m, is rotor mechanical angular velocity.

Thus, the rotor magnet loss can be calculated as following, the detail equations of p_{cn} and p_{an} are reported in [18],

$$P_{mag} = 2pL_{stk}\sum_{n=1}^{\infty}(p_{cn} + p_{an}) \tag{2.152}$$

Where,

$$p_{cn} = \frac{m^2\mu_0^2\alpha_{mp}}{8\rho_{mag}}\frac{K_{sn}^2}{n^2p_s^2}(np_s \mp p)^2\Omega_m^2\left[\left(\frac{R_s}{R_m}\right)^{2np_s}R_s^2R_m^2F_n + \left(\frac{R_s}{R_r}\right)^{2np_s}\frac{R_s^2R_r^2}{2np_s+2}\left(1-\left(\frac{R_m}{R_r}\right)^{2np_s+2}\right) + \left(\frac{R_s}{R_r}\right)^{2np_s}R_s^2(R_r^2-R_m^2)\right]\frac{1}{\left[1-\left(\frac{R_s}{R_r}\right)^{2np_s}\right]^2} \quad (2.153)$$

In which,

$$F_n = \begin{cases}\dfrac{\left(\frac{R_r}{R_m}\right)^{-2np_s+2}-1}{-2np_s+2}, np_s \neq 1 \\ ln\left(\dfrac{R_r}{R_m}\right), np_s = 1\end{cases} \quad (2.154)$$

$$p_{an} = -\frac{m^2\mu_0^2}{\alpha_{mp}\rho_{mag}}\frac{K_{sn}^2}{n^4p_s^4}(np_s \mp p)^2\Omega_m^2\left[\left(\frac{R_s}{R_m}\right)^{np_s}R_s\ R_m^2G_n + \left(\frac{R_s}{R_r}\right)^{np_s}\frac{R_s\ R_r^2}{(np_s+2)}\left(1 - \left(\frac{R_m}{R_r}\right)^{np_s+2}\right)\right]^2\frac{\sin^2(np_s\frac{\alpha_{mp}}{2})}{(R_r^2-R_m^2)\left[1-\left(\frac{R_s}{R_r}\right)^{2np_s}\right]^2} \quad (2.155)$$

In which,

$$G_n = \begin{cases}\dfrac{\left(\frac{R_r}{R_m}\right)^{-np_s+2}-1}{-np_s+2}, np_s \neq 2 \\ ln\left(\dfrac{R_r}{R_m}\right), np_s = 2\end{cases} \quad (2.156)$$

Where, α_{mp} is the mechanical pole arc of the magnet. When $n = 3k + k_m$, the '$\mp$' in p_{cn} and p_{an} are taken as '-', else when $n = 3k - k_m$, the '$\mp$' in p_{cn} and p_{an} are taken as '+'. k is an arbitrary integer number, k_m is 1 or -1 depending on the winding configuration.

From equation (2.152), it indicates rotor magnet loss is proportional to Ω_m^2 (or the square of motor rotating speed) and I_p^2. Although this conclusion is not perfectly right especially at very high speed [14], for the in-wheel motor it fits the FEA results very well at low speed.

2.6 Efficiency map evaluation and loss balance

As for the application of in-wheel electric vehicle, it is important to evaluate motor's efficiency map. The efficiency map could help to estimate the global efficiency of electric vehicle. Be aware of the importance of efficiency map, motor designer can also take necessary measures to optimize the motor design, which will be discussed in the following chapter.

A typical analytically calculated SPM motor efficiency map is as shown in Figure 51. The figure on the left is torque-speed efficiency map, the right one is power-speed efficiency map. To evaluate SPM motor efficiency map, the efficiency map is discretized as Figure 52. First, motor's torque-speed characteristic is calculated. The maximum torque, continuous torque, base speed, turn-over speed (the critical speed between flux-weakening region and MTPV region) and maximum speed are calculated with knowing the maximum current, the maximum voltage and the phase inductance. On each working point, according to motor control strategy, different input currents and voltages are calculated. With these input electric parameters as well as motor geometrical dimensions, three main losses (Copper loss, iron loss and magnet loss) of electric motor can be calculated. Furthermore, the efficiency of each working point is obtained to generate the whole efficiency map.

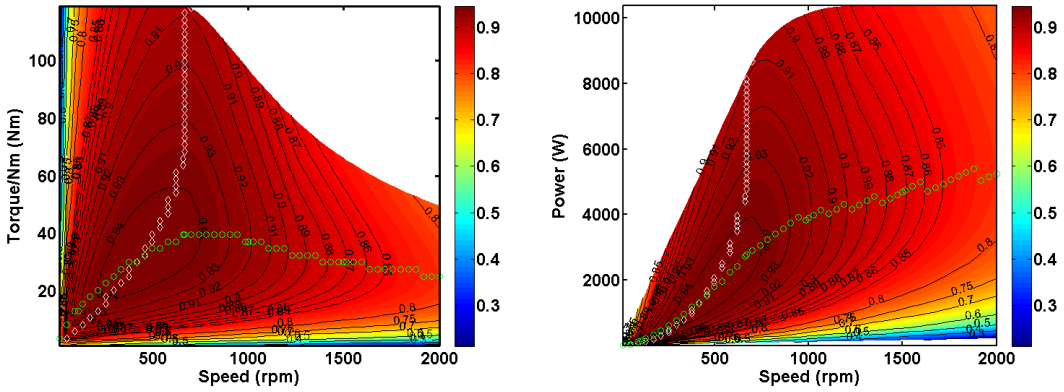

Figure 51 An example of SPM efficiency map

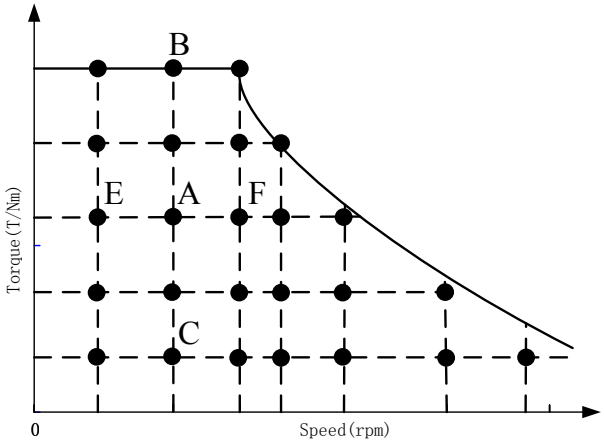

Figure 52 Discretized efficiency map

The flow chart of evaluating motor's efficiency map is shown in Figure 53. It can be seen the necessary inputs are the motor dimensions, voltage and current limits, phase inductance. The analytical algorithms discussed in 2.5.1, 2.5.2 and 2.5.3 are implemented to calculate losses and efficiency. As mentioned in 2.4.2, the algorithm of direct flux-weakening control is adopted to calculate input current of each working point. It also should be noted that the torque and power calculated here are electromagnetic torque and electromagnetic power. Thus, ignoring other kinds of losses, the efficiency of one working point is defined as,

$$\eta = 1 - \frac{P_{Cu} + P_{Fe} + P_{mag}}{T_e \Omega_m}$$

Where,

T_e, is electromagnetic torque,

$T_e \Omega_m$, is the electromagnetic power P_e.

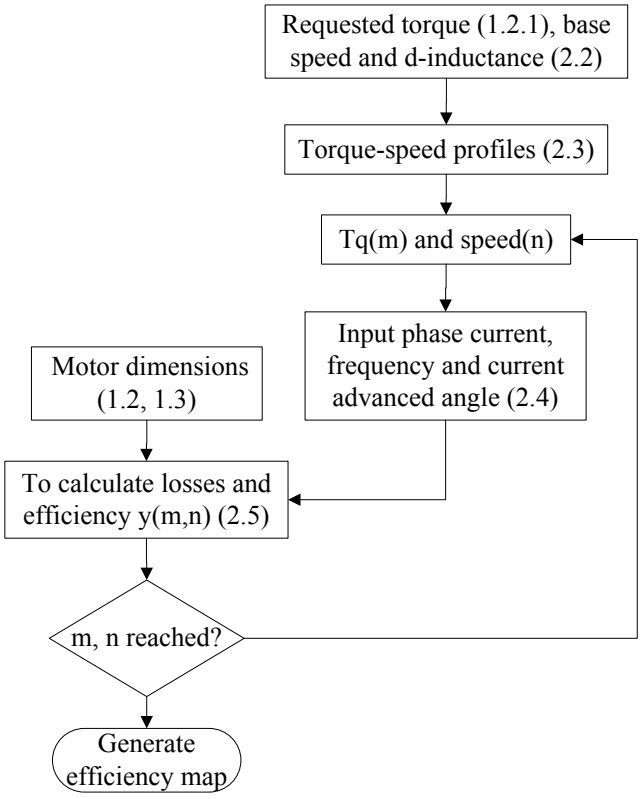

Figure 53 Flow chart of the efficiency map evaluation

For SPM motor, the location of the maximum efficiency area usually takes place within the constant-torque region on the efficiency map. As shown in Figure 51, the maximum efficiency point is in the region of low speed low torque. In order to predict the location of the maximum efficiency point, two formulas describing losses balance are proposed. From the view of losses distribution, the formulas explain why the maximum efficiency point appears at a particular region and whether it is possible to design a motor with a pre-required maximum efficiency point.

For the operating points at the same speed, like the point B, A, C shown in Figure 52, the loss ratio can be calculated as

$$\frac{P_{loss}}{P_e} = \frac{M_{P_{Fe}} + M_{P_{Cu}} {I_p}^2 + M_{P_{mag}} {I_p}^2}{M_{torque} I_p \cdot n} = \frac{M_{P_{Fe}}}{M_{torque} I_p \cdot n} + \frac{M_{P_{Cu}} + M_{P_{mag}}}{M_{torque} \cdot n} I_p \tag{2.157}$$

Where,

$M_{P_{Fe}} = P_{Fe}$, is the core loss,

$M_{P_{Cu}} {I_p}^2 = P_{Cu}$, is the copper loss,

$M_{P_{mag}} {I_p}^2 = P_{mag}$, is the magnet loss, which is the function of ${I_p}^2$,

$M_{torque} I_p$, is the electromagnetic torque,

n, is the motor speed.

Thus, when

$$I_p = \sqrt{M_{P_{Fe}} / (M_{P_{Cu}} + M_{P_{mag}})} \tag{2.158}$$

Namely,

$$P_{Fe} = P_{Cu} + P_{mag} \tag{2.159}$$

P_{loss} / P_{out} can get the minimum value, then the efficiency is maximum versus the phase current at a certain speed as shown in Figure 54. Hence, if at point A, the equation (2.159) is satisfied, then the efficiency of point A will be higher than that of point B and point C.

For the operating points E, A, F on the same torque-speed curve (or at the same phase current) the loss ratio can be calculated as

$$\frac{P_{loss}}{P_e} = \frac{N_{P_{Cu}} + N_{P_{Fe1}} n + N_{P_{Fe2}} n^2 + N_{P_{mag}} n^2}{N_{torque} n} = \frac{N_{P_{Cu}}}{N_{torque} n} + \frac{N_{P_{Fe1}}}{N_{torque}} + \frac{N_{P_{Fe2}}}{N_{torque}} n + \frac{N_{P_{mag}}}{N_{torque}} n \tag{2.160}$$

Where,

$N_{P_{Fe1}} n + N_{P_{Fe2}} n^2 = P_{Fe1} + P_{Fe2}$, is the core loss,

$N_{P_{Cu}} = P_{Cu}$, is the copper loss,

$N_{P_{mag}} n^2 = P_{mag}$, is the magnet loss,

N_{torque}, is the electromagnetic torque T_e.

Thus, when

$$n = \sqrt{N_{P_{Cu}} / (N_{P_{Fe2}} + N_{P_{mag}})} \tag{2.161}$$

Namely,

$$P_{Cu} = P_{Fe2} + P_{mag} \tag{2.162}$$

P_{loss} / P_{out} can reach the minimum value, then the efficiency is maximum versus speed at a certain phase current as shown in Figure 54. Hence, if at point A, the equation (2.162) is satisfied, the efficiency of point A will be higher than that of point E and point F. It can be concluded that the maximum efficiency point happens where both the two formulas are satisfied, namely point A. Besides, Figure 54 indicates the maximum efficiency is approached at the minimum value of the curve of total loss ratio. They illustrate that if the maximum efficiency is requested to be realized at the point of higher speed and lower torque, then the copper loss ratio should be increased and the iron loss ratio as well as the magnet loss ratio should be decreased. For indirect flux-weakening control the formulas are only applicable within the constant-torque region. But when the motor is driven by $i_d = 0$ control the formulas can be applied to the whole range of speed.

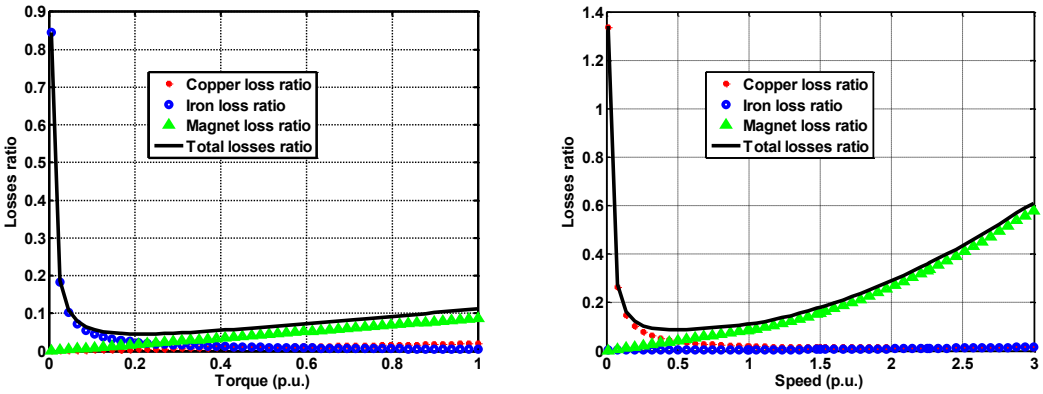

Figure 54 The ratio of losses to eletromagnetic power

(Left: versus torque at the rated speed;

Right: versus speed on the maximum torque-speed curve)

2.7 Three ways to change efficiency map

In order to shift the maximum efficiency area to match motor's regular working area during motor design, it is necessary to investigate the factors affecting motor's efficiency map. Assuming the input power of electric motor is constant, different motor efficiency maps will be compared in the following subsections. Besides, as in-wheel direct drive motor, usually the speed

range is not required to be wide. Here, to make the comparison evident, up to 2000rpm theoretical speed range of efficiency map is calculated.

2.7.1 Dimensions

Two motors having the same volume but different ratios of stator diameter to stator length have been analyzed. They use the same materials (lamination: M1924, magnet: NdFeB), the same winding layout and the same combination of slot and pole number (24 slots, 20 poles). Direct flux-weakening control is adopted to drive the machines. Table 19 and Table 20 show the comparison of motor design and their electric characteristics.

Table 19 Design comparison between Model I and Model II

	p	Q_s	Lamination	Magnet	D (mm)	L_{stk} (mm)	B_g (T)
Model I	10	24	M1924	NdFeB	282	30	0.863
Model II	10	24	M1924	NdFeB	225	47	0.863

Table 20 Electric parameter comparison between Model I and Model II

	$L_{p\hbar}$ (mH)	V_m (V)	I_{scp} (A)	I_p (A)	nN (rpm)	Max. Eff (%)
Model I	0.2112	30	167.48	224.29	693	94
Model II	0.2095	30	211.05	179.43	714	94

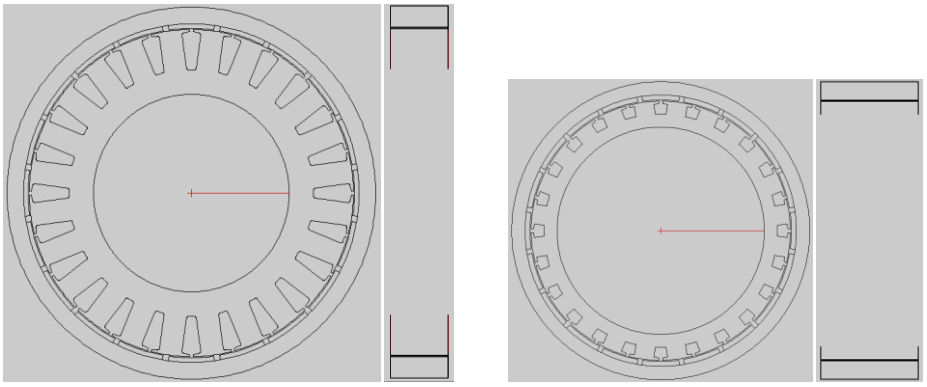

Figure 55 Geometry comparison (left: Do=282mm L=30mm right: Do=225mm L=47mm)

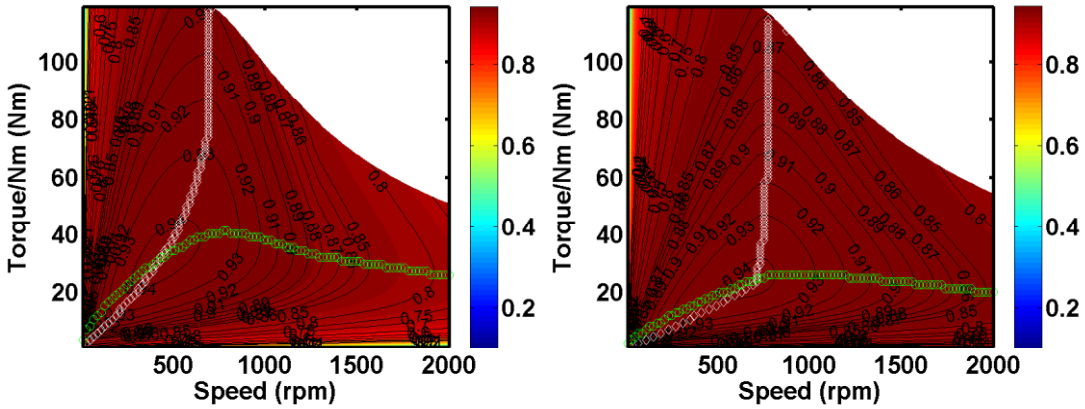

Figure 56 Efficiency map comparison (left: Do=282mm L=30mm right: Do=225mm L=47mm)

It can be observed that although the current of Model II is less than that of Model I, its slot current density is higher, 22A/mm^2 compared with 8.8A/mm^2 of Model I. This leads to the higher copper loss and lower overall efficiency. With the increasing of copper loss, the maximum efficiency area is shifted to high speed region. Because less copper is used in Model II, its weight is less.

2.7.2 Materials

Both the models have the same dimensions (Do=282mm L=30mm), the same magnets, the same winding layout and combination of slot and pole number (24 slots 20 poles). The same control strategies are adopted to drive the machines (direct flux-weakening control). But they use different materials of stator laminations. Vacoflux50 exhibits much better magnetic performance than M1924, and lower specific iron loss.

Table 21 Design comparison between Model I and Model III

	p	Q_s	Lamination	Magnet	D (mm)	L_{stk} (mm)	B_g (T)
Model I	10	24	M1924	NdFeB	282	30	0.863
Model III	10	24	Vacoflux50	NdFeB	282	30	0.863

Table 22 Electric parameter comparison between Model I and Model III

	$L_{p\hbar}$ (mH)	V_m (V)	I_{scp} (A)	I_p (A)	nN (rpm)	Max. Eff (%)
Model I	0.2112	30	167.48	224.29	693	94
Model III	0.2112	30	167.48	224.29	693	96

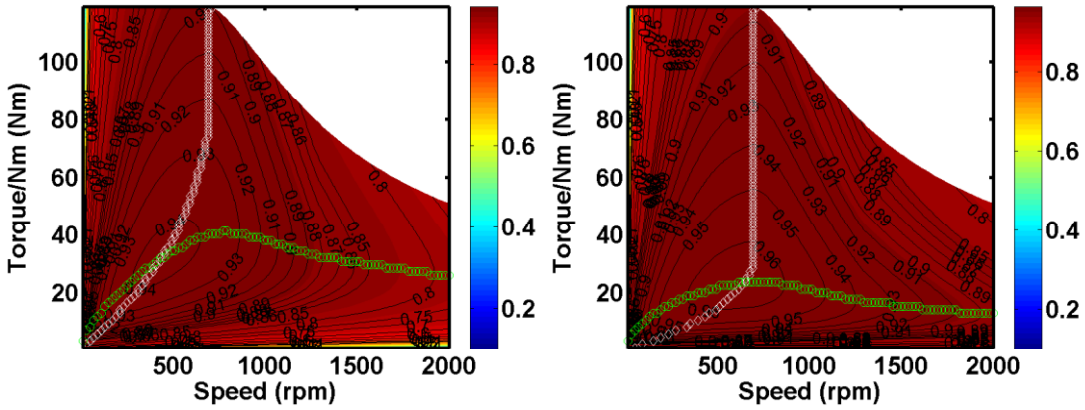

Figure 57 Efficiency map comparison (left: M1924 right: Vacoflux50)

It can be observed that Model III with lower iron loss has maximum efficiency area in the low-torque high-speed region. The overall efficiency is also improved. The weight and slot current density are nearly the same.

2.7.3 The combination of slot and pole number

Both the models have the same dimensions (Do=282mm L=30mm). They use the same materials (Lamination: M1924, Magnet: NdFeB) and are driven by the same control strategy (direct flux-weakening control). But they have different combinations of slot and pole number.

From Figure 60 it can be found that the copper loss of Model IV is decreased a little in comparison with that of Model I. The magnet loss is decreased greatly because it is the same situation that the magnets are segmented. The iron loss is nearly doubled because the frequency is doubled. The change of losses distribution shifts the maximum efficiency area to high-torque region on the efficiency map. Besides, both the models have nearly the same weight and slot current density.

Table 23 Design comparison between Model I and Model IV

	p	Q_s	Lamination	Magnet	D (mm)	L_{stk} (mm)	B_g (T)
Model I	10	24	M1924	NdFeB	282	30	0.863
Model IV	20	48	M1924	NdFeB	282	30	0.863

Table 24 Electric parameter comparison between Model I and Model IV

	$L_{p\hbar}$ (mH)	V_m (V)	I_{scp} (A)	I_p (A)	nN (rpm)	Max. Eff (%)
Model I	0.2112	30	167.48	224.29	693	94
Model IV	0.4101	60	86.25	112.14	693	94

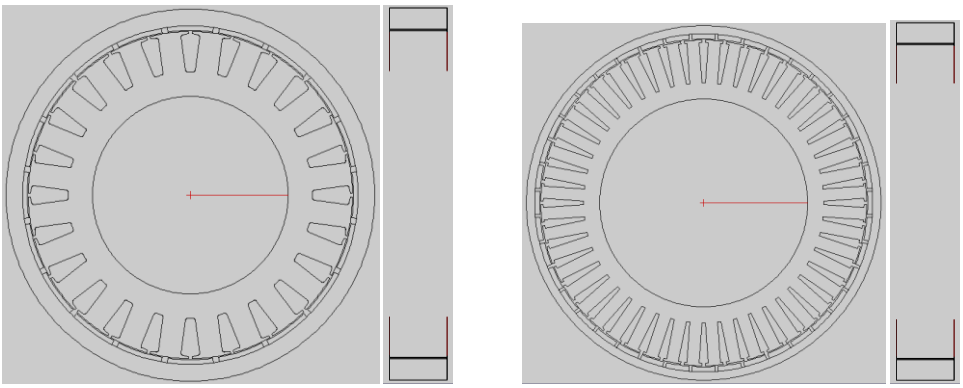

Figure 58 Geometry comparison (left: 24 slots 20 poles right: 48 slots 40 poles)

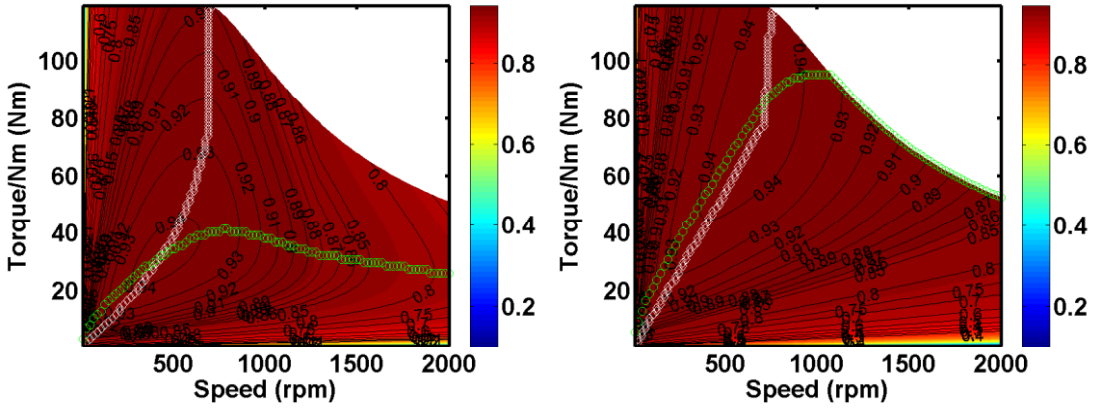

Figure 59 Efficiency map comparison (left: 24 slots 20 poles, right: 48 slots 40 poles)

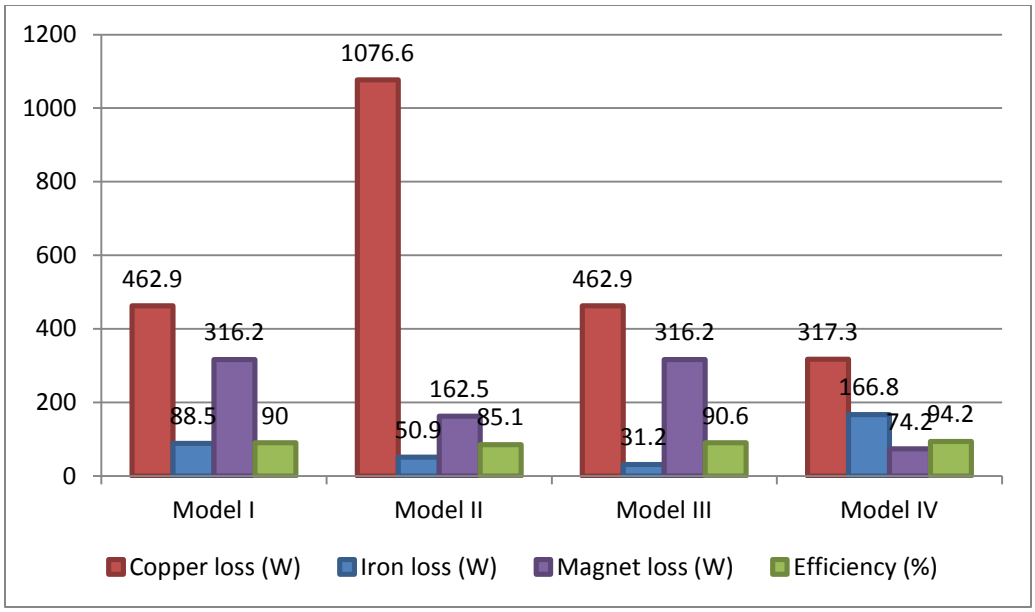

Figure 60 Comparison of losses and efficiency at the working point 119Nm 693rpm

CHAPTER III

OPTIMIZATION OF MOTOR DESIGN BASED ON EFFICIENCY MAP

In this chapter, starting with driving cycle analysis and powertrain design of electric vehicle, motor design specification is specified. Two motor designs are proposed by multi-objective optimization design procedure. Different motor designs are compared from the view of efficiency map and energy saving on board.

3.1 Driving cycle analysis

Driving cycle is a series of data composed by time as x-axis and vehicle velocity as y-axis, which is produced by different countries and organizations to assess the performance of vehicles. In this section, according to different driving cycles, the requested traction torque and motor speed are calculated for a certain electric vehicle. Motor's regular working area will be discovered.

As shown in Figure 61, when an electric vehicle moving on uphill, except the traction force (F_t) from electric motor, there are several resistant forces imposed including rolling resistance (F_{rf} and F_{rr}), aerodynamic resistance (F_w) and grading resistance ($M_g \sin\alpha$) [80], [81].

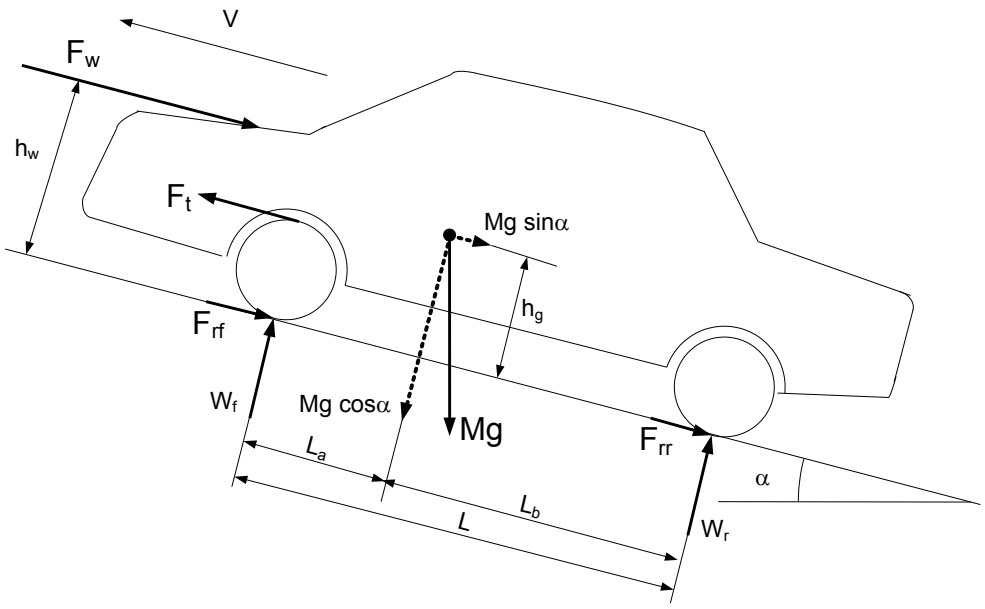

Figure 61 Forces acting on a vehicle

According to Newton's Second Law,

$$\frac{T_m i_t \eta_t}{r} = Mgf_r cos\alpha + \frac{1}{2}\rho_a C_D A_f V^2 + Mgsin\alpha + \delta M \frac{dV}{dt} \tag{3.1}$$

Where,

T_m, is the output torque from electric motor, Nm,

i_t, is the gear ratio of transmission,

η_t, is the efficiency of transmission,

r, is the tire rolling radius, m,

M, is the total mass of electric vehicle, kg,

g, is the gravity acceleration, 9.81 $\mathrm{m/s^2}$,

f_r, is the rolling resistance coefficient,

α, is the grade angle,

ρ_a, is the air density, 1.202 $\mathrm{kg/m^3}$,

C_D, is drag coefficient, 0.335,

A_f, is the front face area, $\mathrm{m^2}$,

V, is the velocity of electric vehicle, $\mathrm{m/s}$,

δ, is the rotational inertia factor,

$$\delta = 1 + \frac{J}{Mr^2} \tag{3.2}$$

Where,

J, is the total rotating moment of the rotating components including in-wheel motor and the wheel, $\mathrm{Nm/rad/s^2}$, for the tire 195/65R15 its value is 3.718.

r, is the tire rolling radius, m.

For an electric vehicle with fuel cell as energy source, its specification and powertrain [82] are shown in Table 25 [83] and Figure 62 respectively. Thus, when this electric vehicle running with a certain driving cycle. According to (3.1), the request values of traction torque can be calculated with the series data of velocity from driving cycles.

For the driving cycle of UDDS(or FTP75) with constant road grade equal to 0 degree, the velocity versus time is shown in Figure 63. For the electric vehicle shown in Table 25, the requested values of torque on each wheel are calculated as shown in Figure 64. In Figure 65, the torque- speed profile is divided into several blocks and how much time the in-wheel motor works within this block is also indicated. It can be observed that the regular working area of this in-wheel motor is around the working point of 30Nm at 400rpm. Consequently, this type of driving cycle can be categorized as" low speed low torque". The same method is also used to calculate other driving cycles like NewYorkBus and UDDSHDV as shown in Figure 66 and Figure 69

respectively, always with 0 degree of road grade. Similarly, the regular working area is around 178Nm at 200rpm in the "low speed high torque" region and 40Nm at 667rpm in the "high speed low torque" region respectively.

Table 25 Specification of electric vehicle

Total mass(kg)	M	1100
Front face area(m^2)	A_f	2
Drag coefficient	C_d	0.335
Tire rolling radius(m)	r	0.282
Rolling resistance coefficient	f_r	0.009
Maximum expected speed(km/h)	V_{Max}	150
Speed range ratio	x	2
Gradeability speed(km/h)	V_g	10
Maximum gradeability	i	20%
Crusing range(km)	L_c	230
Acceleration time (0-100km/h) (s)	t_a	15
Rotational inertia factor	δ	1.0425
Air density(kg/m^3)	ρ_a	1.202
Tire		195/65 R15
Drive mode		4WD

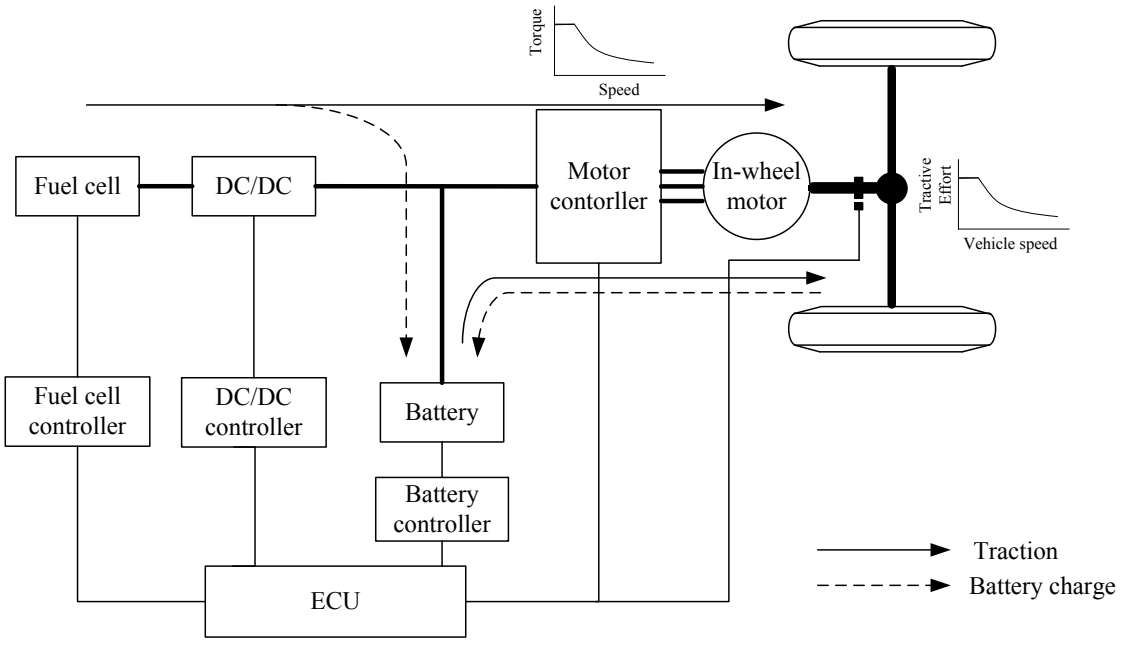

Figure 62 Powertrain of a fuel-cell electric vehicle

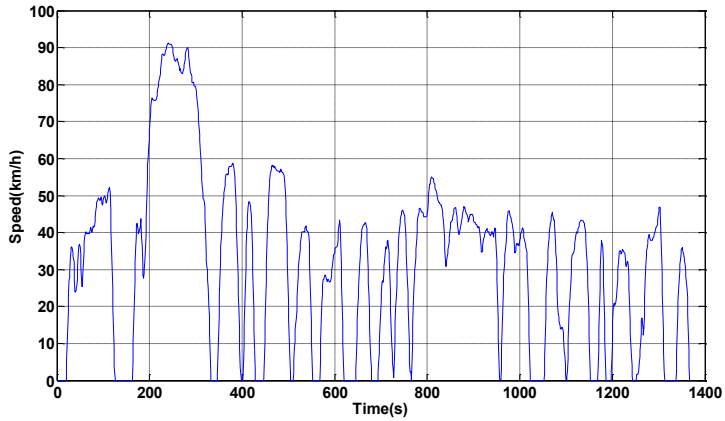

Figure 63 Driving cycle of UDDS

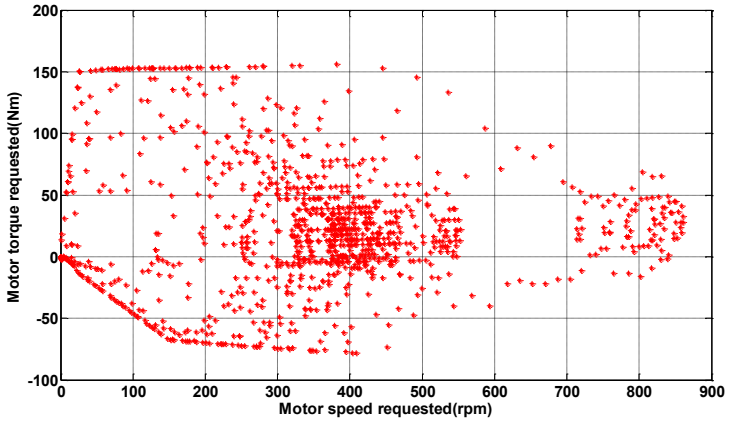

Figure 64 Requested torque and speed of UDDS

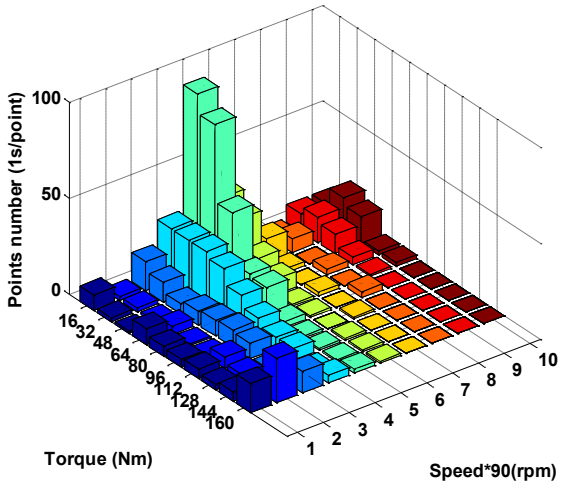

Figure 65 Requested torque and speed of UDDS

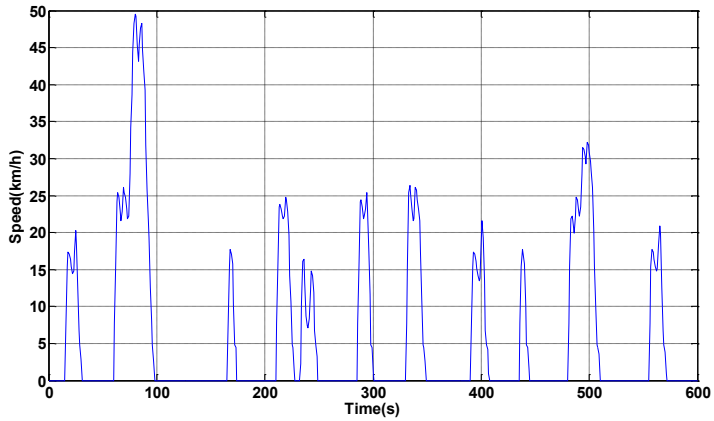

Figure 66 Driving cycle of NewYorkBus

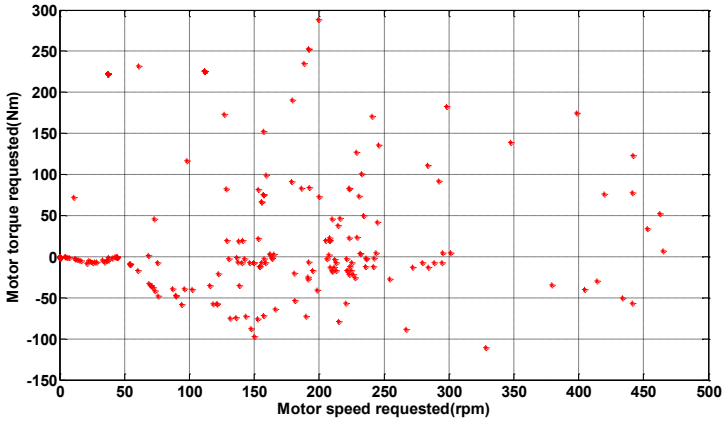

Figure 67 Requested torque and speed of NewYorkBus

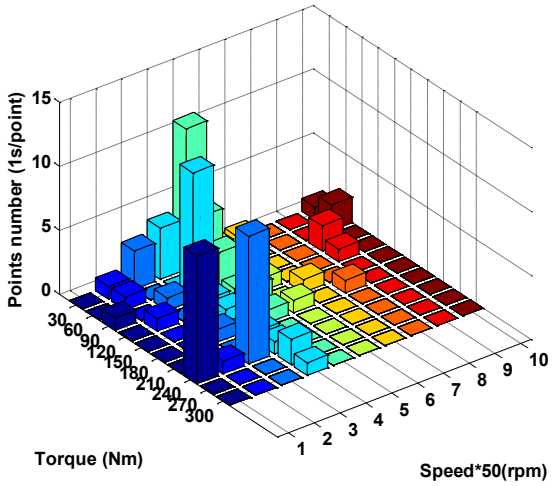

Figure 68 Requested torque and speed of NewYorkBus

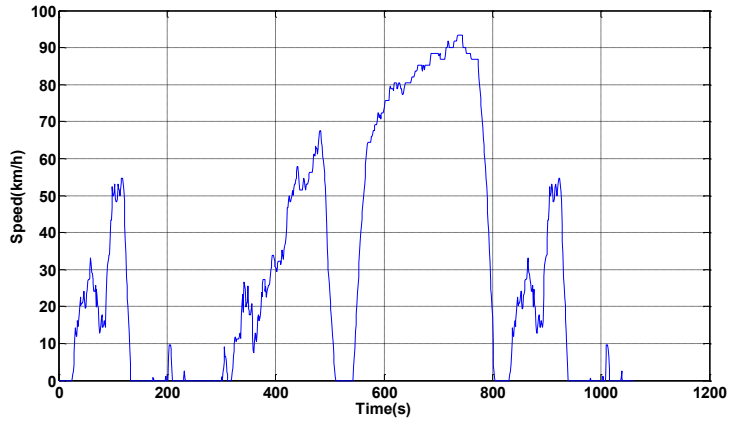

Figure 69 Driving cycle of UDDSHDV

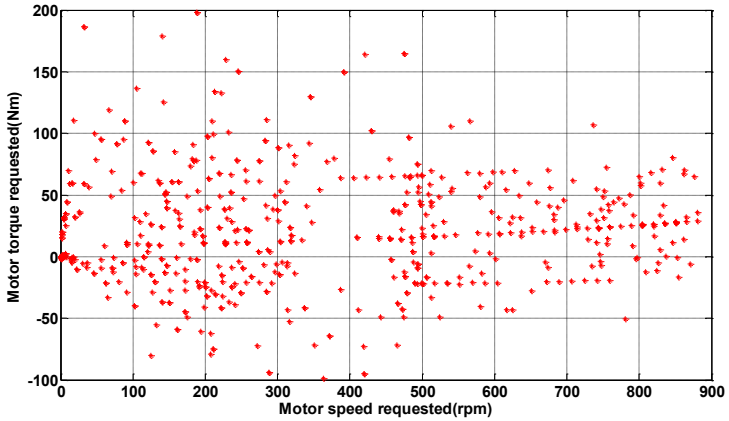

Figure 70 Requested torque and speed of UDDSHDV

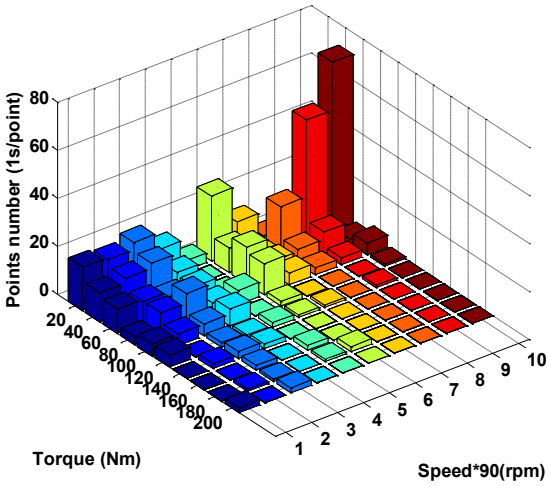

Figure 71 Requested torque and speed of UDDSHDV

3.2 Powertrain power size design

3.2.1 Motor design specification

The performance of electric vehicle is assessed from three aspects: acceleration ability, gradeability and crusing range. The first two assessment requires the motor to deliver enough traction power and the last one requires enough energy source provided or deposited by fuel cells and batteries.

The traction power for accelerating the vehicle from zero km/h to V_f km/h in t_a seconds can be expressed as

$$P_t = \frac{\delta M}{2t_a}\left(\left(\frac{V_f}{3.6}\right)^2 + \left(\frac{V_b}{3.6}\right)^2\right) + \frac{2}{3}Mgf_r\frac{V_f}{3.6} + \frac{1}{5}\rho_a C_D A_f\left(\frac{V_f}{3.6}\right)^3 \tag{3.3}$$

Where,

V_b is the base speed, $x = V_f/V_b$ is the speed ratio assumed to be 2~3,

V_f is equal to 100km/h.

As the vehicle specification in Table 25, the maximum driving speed V_{Max} is 150km/h. Thus, V_b can be taken as 75km/h. Substituting into (3.3), it can be obtained that

$$P_t = 1.0425 \times \frac{1100}{2 \times 15} \times [\left(\frac{70.88}{3.6}\right)^2 + \left(\frac{100}{3.6}\right)^2] + \frac{2}{3} \times 1100 \times 9.8 \times 0.009 \times (\frac{100}{3.6}) + \frac{1}{5} \times 1.202 \times 0.335 \times 2 \times \left(\frac{100}{3.6}\right)^3 \approx 50\text{kW}$$

For the four-wheel drive, the power size of each in-wheel motor is

$$P_{motor} = \frac{P_t}{4} = 12.5\text{kW} \tag{3.4}$$

The base speed of both electric vehicle and electric motor is

$$n_N = \frac{V_b}{0.377r} \tag{3.5}$$

which is equal to $75/(0.377 \times 0.282) \approx 700\text{rpm}$, thus the maximum torque is 170Nm.

This result is the power size of in-wheel motor estimated from the specification of acceleration ability. Moreover, it can be also estimated from the view of maximum speed. The traction power for maintaining the vehicle running at the maximum speed can be expressed as

$$P_t = \frac{1}{3600}\left(Mgf_r + \frac{C_d A_f V_{MAX}^2}{21.15}\right)V_{MAX} \tag{3.6}$$

Substituting the parameters, it is equal to

$$P_t = \frac{1}{3600} \times \left(1100 \times 9.8 \times 0.009 + \frac{0.335 \times 2 \times 150^2}{21.15}\right) \times 150 \approx 34\text{kW}$$

which is much less than the traction power calculated from vehicle's acceleration ability.

Finally, the requested torque from vehicle's gradeability is calculated as

$$T_g = \left(Mgf_r\, cos(arctan(i)) + \frac{C_d A_f V_g^2}{21.15} + Mgsin(arctan(i))\right) r \qquad (3.7)$$

which is equal to

$$T_g = (1100 \times 9.8 \times 0.009 \times \cos(\text{atan}(0.2)\,) + 0.335 \times 2 \times \frac{10^2}{21.15} + 1100 \times 9.8 \times \sin(\text{atan}(0.2)\,)\,) \times 0.282 = 624\text{Nm}$$

For each wheel the requested torque is 156Nm. It can be seen the motor specification calculated from vehicle acceleration ability can also satisfy vehicle maximum driving speed and gradeability. In sum, the specification of the electric motor is specified as shown in Table 26 and Figure 72.

Table 26 Specification of in-wheel motor

Rated/Max rpm	700/1500rpm
Max torque	170Nm
Max power	12.5kW

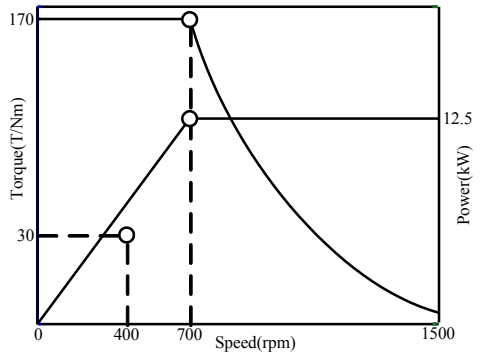

Figure 72 Design specification of in-wheel motor

3.2.2 Power size design of fuel cell and battery

The battery of Evercel 22AH prismatic NiZn is adopted with 25 modules. The DC bus voltage is $12.28\text{V} \times 25 = 307\text{V}$. The weight of battery is $6.35\text{kg} \times 25 \approx 159\text{kg}$.

To check whether the number of battery modules could satisfy the need of the maximum traction power, it is calculated by

$$n_{module} = \frac{P_{tmax}}{p_{bmax}\eta_m\eta_{mc}} \qquad (3.8)$$

Where,

P_{tmax}, is the maximum traction power,

p_{bmax}, is the specific power,

η_m, is the efficiency of electric motor, assumed to be 95%,

η_{mc}, is the efficiency of motor controller, assumed to be 95%.

Thus, the number of battery modules needed is equal to

$$n_{module} = \frac{50 \times 1000}{900 \times 6.35 \times 0.95 \times 0.95} \approx 10$$

Which is less than 25 modules.
However, according to the cruising range, the number of battery modules is re-calculated as

$$n_{module} = \frac{F_t L_c}{W_{bmax}} \tag{3.9}$$

Where,

F_t, is the traction force,

L_c, is the cruising range,

W_{bmax}, is the specific energy.

Thus, the number of battery modules needed is

$$n_{module} = \frac{\frac{34000}{75} \times 230}{100 \times 6.35} \approx 164$$

Which is much more than 25 modules. It indicates that the energy stored in battery could only sustain $25/164 \times 230 = 35$km.
Assessing the power size of fuel cells, the efficiencies of DC/DC converter and fuel cell are also considered. The peak power that fuel cell system should provide are given by

$$P_{FCmax} = \frac{P_{tmax}}{\eta_m \eta_{mc} \eta_{DCDC} \eta_{FC}} \tag{3.10}$$

Where,

η_{DCDC}, is the efficiency of DC/DC converter, assumed to be 95%,

η_{FC}, is the efficiency of fuel cell, assumed to be 80%,

Then, it is

$$P_{FCmax} = \frac{50}{0.95 \times 0.95 \times 0.95 \times 0.8} = 73\text{kW}$$

3.3 Multi-objective optimization design

The necessary input parameters of optimization procedure are motor regular operating torque and speed, which are calculated according to a certain driving cycle. The design objective is to design a motor whose maximum efficiency point matches its regular working point.

The mechanical constraints are defined according to the dimensions of wheel and the intrinsic structure constraints of motor design. There are five design variables. Their ranges are defined by the mechanical constraints to avoid geometry conflictions. But if there is geometry confliction detected, this design result will be filtered out by the optimization algorithm.

Due to the harsh working environment of in-wheel motor slot current density at the maximum output torque should also be confined within a reasonable range. The range depends on the cooling condition and motor operating condition. In order to choose the optimal design solution among a wide range of samples, the slot current density could be taken as an objective function. Another objective function is defined to satisfy the formulas (2.159) and (2.162) so that the maximum efficiency point will take place at the requested operating point.

The algorithm of multi-objective optimization NSGA-II [84–86] is adopted, which is an advanced algorithm based on Genetic Algorithm. Its input are the number of populations, *M*, the number of generations, *N*, the ranges of design variables, and objective functions. The purpose of the optimization procedure is to generate a family of results, which minimize the objective functions meanwhile not dominating each other. The flow chart of optimization procedure is shown in Figure 73. The initial values of *M* populations are generated randomly within the variables' ranges. Then the dimensions of motor are specified by the design variables. Motor losses are calculated on the regular operating point (Tq, n) to get the values of objective functions. After *N* times of evolution, a family of optimal design solutions is generated.

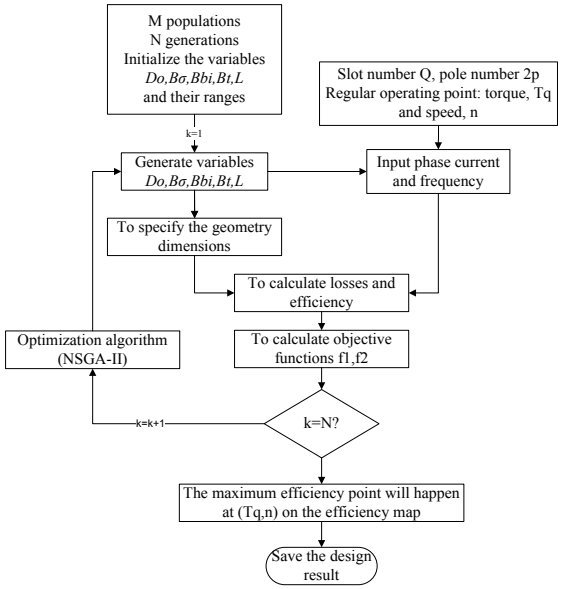

Figure 73 Flow chart of optimization procedure

Table 27 Mechanical constraints and ranges of variables

The number of populations = 50	
The number of generations = 100	
Mechanical constraints	
The outermost diameter $D_{ext} < 360mm$	
The innermost diameter $D_{int} > 180mm$	
The width of teeth *wt*>2.5mm	
The thickness of magnet *LM*>3mm	
Range of variables	
D_o (mm)	230~330
B_g (T)	0.86~0.96
B_{sj} (T)	0.6~1.5
B_{st} (T)	0.6~1.5
L (mm)	<80
Objective functions	
$f_1 = abs(P_{Fe} - P_{Cu} - P_{mag}) + abs(P_{Cu} - P_{Fe}2 - P_{mag})$	
$f_2 =$ Slot current density	

3.4 Comparison of motor designs

A 20-poles 24-slots SPM in-wheel motor is designed with the motor design procedure for a 4-wheel-drive electric vehicle. Based on the driving cycle of UDDS shown in Figure 63, the regular working point is 30Nm and 400rpm. The design specification of an in-wheel motor is proposed in Figure 72. The constraints, variables' ranges and objective functions are listed in Table 27 for the motor design procedure. After 100 generations of evolution, 50 design results are acquired. Their values of objective functions are shown in Figure 74. The design results do not dominate each other, namely that none is better than another when comparing the values of the two objective functions. It shows that with the bigger value of f_1 the maximum efficiency area will appear further away from the expected operating point. But with lower value of f_1 there will be higher slot current density. Hence, considering both aspects, Design I is selected as shown in Figure 75 and Table III.

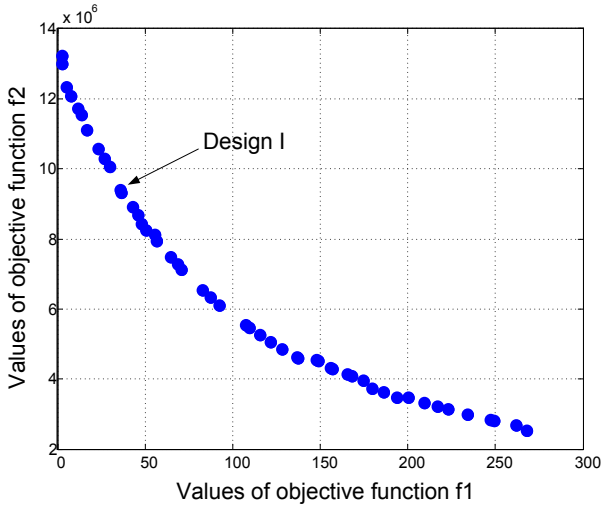

Figure 74 Values of objective functions of design results

Table 28 Common specifications of the motor designs

Phase number	3
Magnet	NdFeB
Lamination	M1942
Magnet arc	160 elec.deg
Turns per coil	10
Filling factor	45%
Rated speed	700rpm
Max torque	170Nm
Magnet electrical resisitivity	0.16e-5 Ohm.m
Relative permeability	1.1
Remanence	1.12 T
LM	4.3mm

Table 29 Motor designs

	Design I	Design II
Pole pairs	10	20
Slot number	24	48
Winding factor	0.966	0.966
Air gap (mm)	1	1
Slot opening (mm)	3	2
Bg (T)	0.86	0.86
Do (mm)	282	282
L (mm)	30	45
hj (mm)	14	10.80
ht (mm)	37	40.20
wt (mm)	21.20	10.60
Ip (A)	320.41	106.80
Im/Isc	1.91	1.23
Vm (V)	37.71	87.33
Phase inductance (mH)	0.21	0.61
Current density @170Nm(A/mm^2)	12.57	8.37
Total weight (kg)	12.69	14.52

Figure 76 and Figure 77 show the efficiency map of Design I. The maximum efficiency is realized at the operating point of 30Nm 400rpm. The efficiency is 94.5%. At this point the copper loss, iron loss and magnet loss are 29.4W, 36.4W and 6.7W respectively, which satisfy the formulas of losses balance equations. The efficiency at the point of 170Nm 700rpm is 86.3%, 8.2% lower than the maximum efficiency. The power factor map is shown in Figure 78.

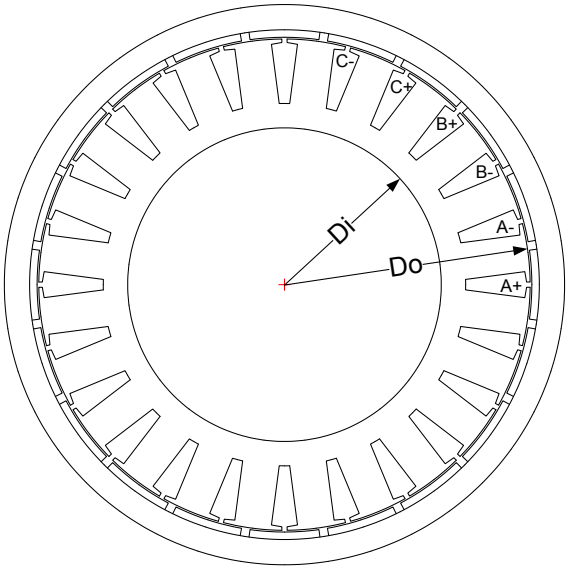

Figure 75 View of In-wheel motor Design I

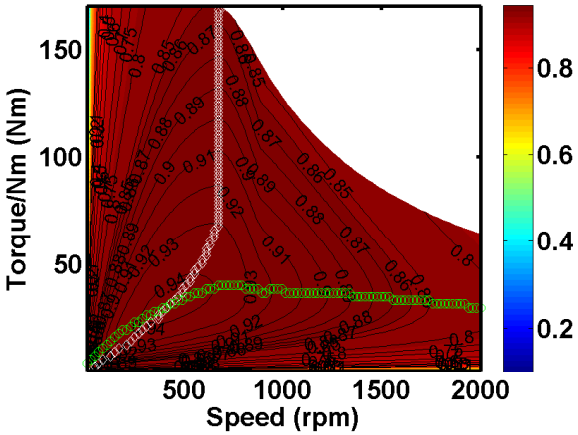

Figure 76 The torque-speed efficiency map of Design I

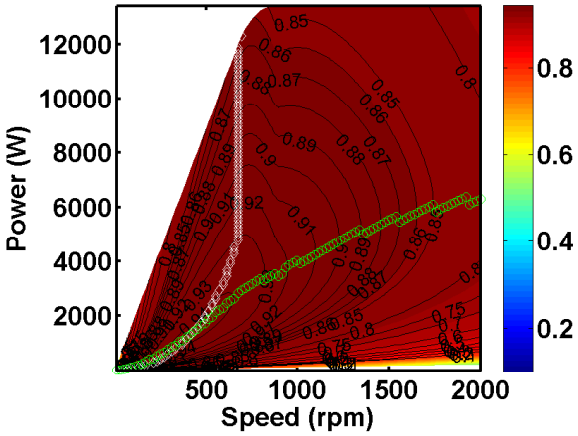

Figure 77 The power-speed efficiency map of Design I

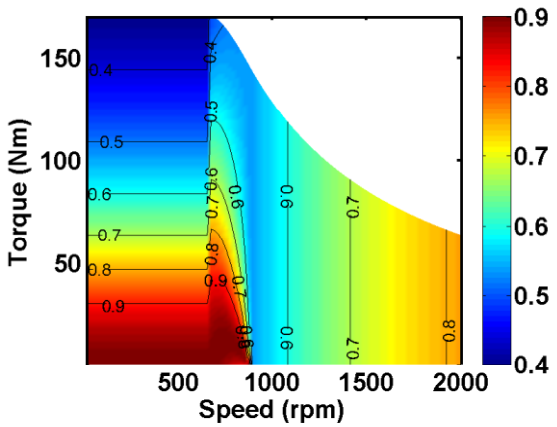

Figure 78 The torque-speed power factor map of Design I

To further illustrate the changing of efficiency map by motor design, based on Design I, Design II is proposed for another driving cycle NewYorkBus shown in Figure 66, which requests the maximum efficiency deployed at the operating point of high torque. Design I and Design II share some same design specifications as shown in Table 28. As discussed in 2.6, in order to shift the maximum efficiency area to high torque region, the iron loss ratio should be increased while the magnet loss and copper loss ratio should be decreased. The changes of stator diameter and lamination length could reassign losses ratio and influence efficiency map. But within limited space, it is difficult to vary motor geometry too much. Another more effective method is to change the combination of slot and pole numbers.

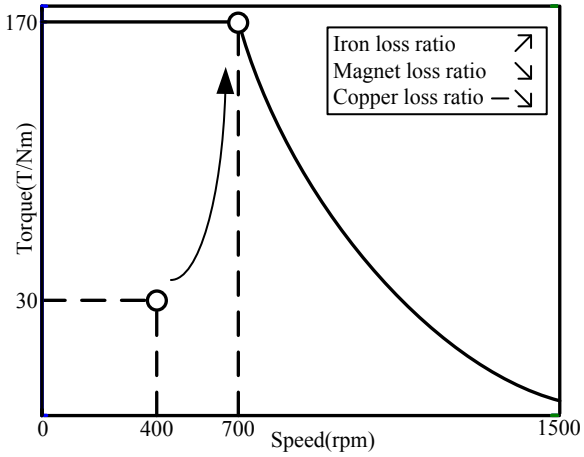

Figure 79 Shifting maximum efficiency point

From 2.5.2, it can be seen that the core loss is only influenced by pole number and has nothing to do with the slot number. Thus, increasing pole number leads to increase core loss ratio. From the view of copper loss ratio, for the same requested torque and the same geometry of motor, Figure 45 lists the copper loss of all possible combinations of slot and pole numbers. The combinations whose copper losses are equal or less than that of 20 poles and 24 slots are the potential candidates. The magnet loss is mainly caused by the MMF harmonics which are asynchronous with rotor. After investigating the possible combinations, from 2.5.3 it can be found for the same

diameter and input current the magnet loss of 10 pole pairs and 24 slots is much higher than that of 20 pole pairs and 48 slots.

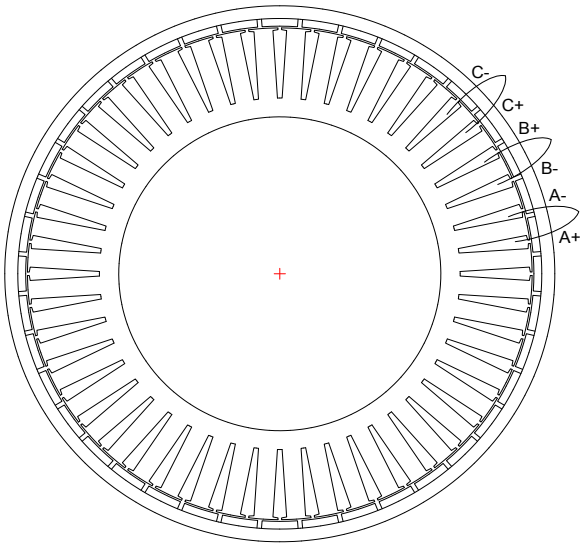

Figure 80 SPM motor with 40 poles and 48 slots

Thus, Design II is proposed as shown in Figure 80 and Table 29. To make a comparison, it has the same stator diameter. Longer lamination helps increase the core loss ratio more as shown in Figure 81. In Design II, the maximum efficiency 94.5% is shifted to the operating point of 114Nm 538rpm. The efficiency of 30Nm 400rpm is decreased to 90.7%. The comparison of losses distribution between Design I and Design II at 119Nm 667rpm is shown in Figure 85. It can be observed that with reference to the same output the copper loss is decreased, the iron loss is increased and the magnet loss is decreased. This agrees with Figure 79.

To conclude, for SPM motor the maximum efficiency point on the efficiency map appears when the formulas (2.159) and (2.162) are both satisfied. Utilizing this characteristic in multi-objective optimization, SPM motor can be designed to make its maximum efficiency area cover its regular working area for a certain driving cycle and control strategy. Within limited space, the motors with different number of slots and poles can exhibit different efficiency maps. Taking advantage of the characteristic of losses balance formulas, changing the combination of slot and pole numbers can shift the maximum efficiency area from one part to another.

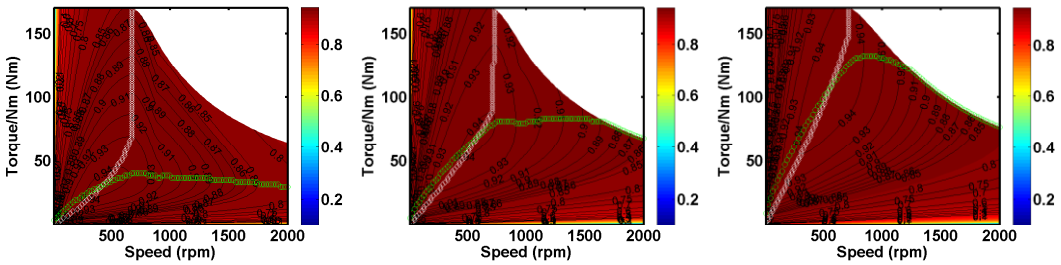

Figure 81 Comparison of efficiency maps (Left: Do=282mm, L=30mm, Qs=24, p=10;

Center: Do=282mm, L=30mm, Qs=48, p=20; Right: Do=282mm, L=45mm, Qs=48, p=20)

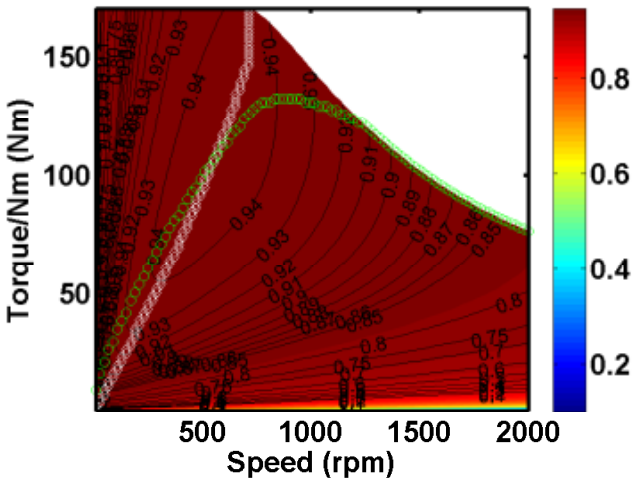

Figure 82 The torque-speed efficiency map of Design II

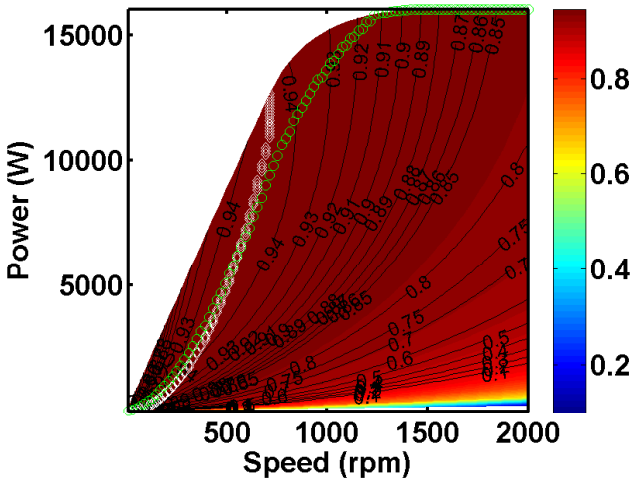

Figure 83 The power-speed efficiency map of Design II

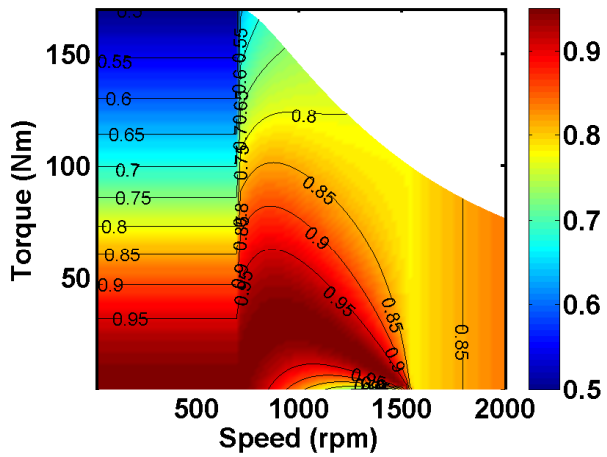

Figure 84 The power factor map of Design II

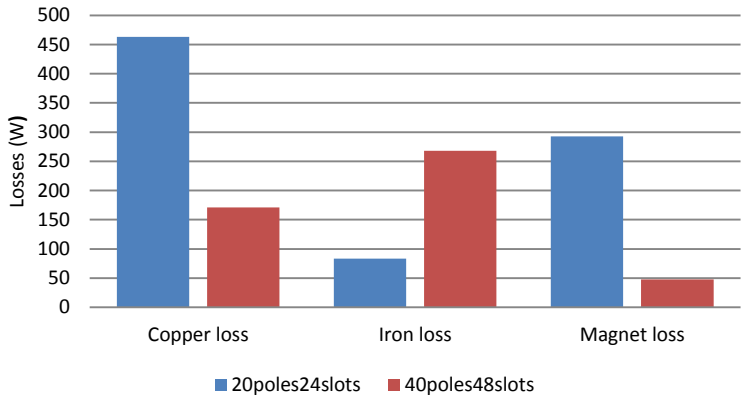

Figure 85 Losses comparison between Design I and Design II

3.5 Performance evaluation of motor design in powertrain

The powertrain of electric vehicle is analyzed with the help of Advisor2002 [35] as shown in Figure 86. Both the motors of Design I and Design II are equipped on the vehicle for the driving cycle of UDDS. Their energy consumption and efficiency will be compared.

As introduced in Figure 62, the power train of electric vehicle is composed by fuel cell (grey and green blocks) and fuel cell converter (blue block), battery and battery converter (grey block with black dots), motor and motor controller (grey block with black sideline).

Before the analysis, several assumptions have to be declared in advance:

1) Because there are four in-wheel motors, the transmission should be ignored, whose efficiency is set as 1 in Advisor2002.

2) In this model, the motor and motor controller are integrated into one single block. Thus the efficiency map of this block should be the multiplication of efficiency map of motor and that of motor controller. However, the objective in this section is to compare the performance of two motor designs with the same power size. The efficiency of motor controller is considered as a constant as 1.

3) The four in-wheel motors are assumed to have the same working condition. Therefore, they can be equivalent to one synthesized motor block, which has the same efficiency map to that of individual in-wheel motor but with quadruple torque value.

4) The efficiency map calculated in analytical way with y-axis of electromagnetic torque rather than output mechanical torque. However, the motor block in this model receives reference signals of requested output mechanical torque and speed. Considering the error is less, the efficiency map with electromagnetic torque as y-axis can be precise enough.

5) The motor will run in regeneration mode to send the energy back into battery when the vehicle brakes. Here, the efficiency map of generation mode is assumed to be equal to that of traction mode.

Finally, the performance of fuel cell electric vehicle with different motor designs (Design I and Design II as shown in Table 28 and Table 29) for the driving cycle of UDDS as shown in Figure 63 and Figure 66) are analyzed. The vehicle runs one round of the driving cycle with 0 road grade. The acceleration ability and gradeability are also calculated.

Table 30 Acceleration and gradeability test

	0-96.6km/h	Max. speed	20%
Design I	15s	187.2km/h	57.9km/h
Design II	14.7s	187.2km/h	57.9km/h

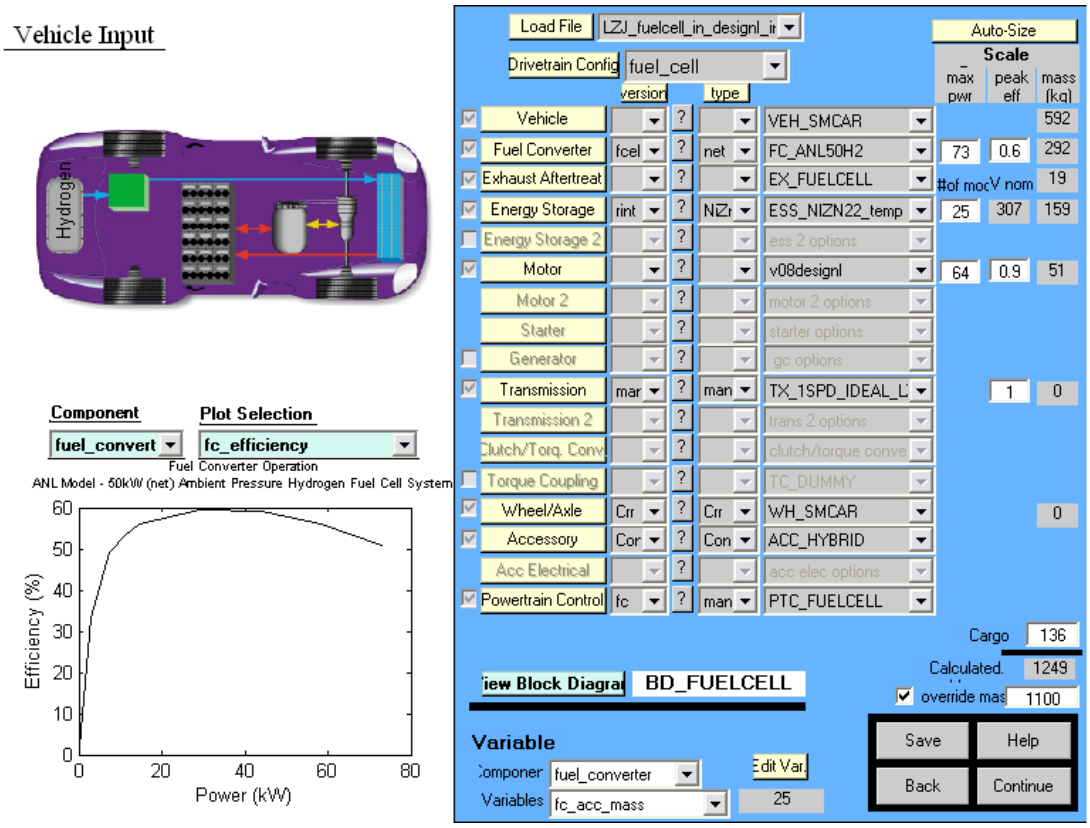

Figure 86 Powertrain analysis in Advisor2002

Table 31 Performance comparison of motor/controller of UDDS

	Losses		Efficiency		Fuel consumption
	Traction	Regeneration	Traction	Regeneration	
Design I	461kJ	79kJ	90%	91%	16L/100km
Design II	1414kJ	147kJ	75%	84%	46.6L/100km

It can be concluded that both the motors can satisfy the specification of electric vehicle from the view of acceleration ability and gradeability. After running one round of driving cycle UDDS, Design I with high efficiency area around 30Nm 400rpm on the efficiency map shows better performance with lower loss generation, higher efficiency and lower fuel consumption in

comparison with Design II. The high efficiency area of Design II is located around 114Nm 538rpm. Its worse performance indicates the impact of motor efficiency map on vehicle performance. Figure 87 and Figure 88 show the operation points of electric motors and their efficiency maps as calculated in Figure 76 and Figure 82.

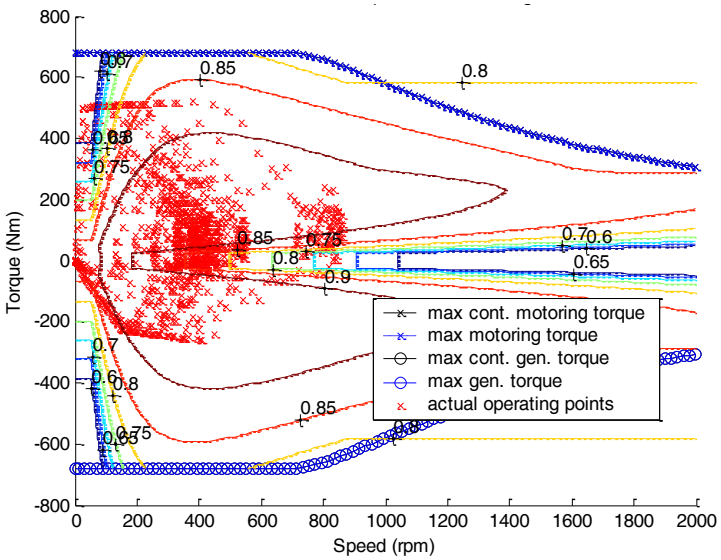

Figure 87 Motor/Controller operation of Design I under UDDS

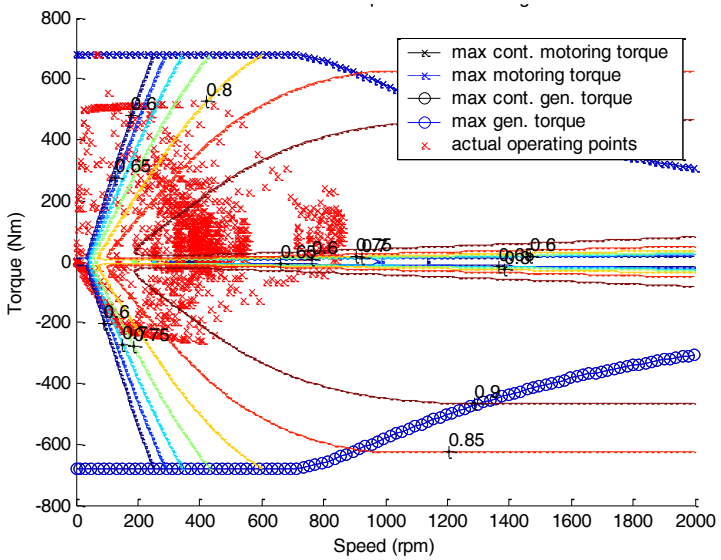

Figure 88 Motor/Controller operation of Design II under UDDS

CHAPTER IV

FEM EVALUATION

Considering the Finite Element Method (FEM) can provide more reliable and accurate results. In this chapter, the characteristics of the SPM motor designs are also calculated in FLUX 2D. The analytic results are compared with the FEM results.

4.1 Inductance calculation

First, the theory used to calculate phase inductance of SPM motor is introduced [87]. As shown in Figure 89, the d-q rotating coordinate can be taken as the equivalence of the static three-phase coordinate.

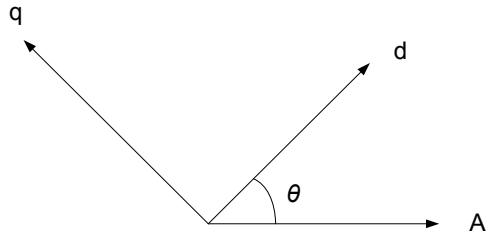

Figure 89 Three-phase coordinate and its equivalent d-q coordinate

The transformation from ABC reference to d, q reference is given by,

$$\begin{bmatrix} i_A \\ i_B \\ i_C \end{bmatrix} = \sqrt{\frac{2}{3}} \begin{bmatrix} 1 & 0 \\ -\frac{1}{2} & \frac{\sqrt{3}}{2} \\ -\frac{1}{2} & -\frac{\sqrt{3}}{2} \end{bmatrix} \begin{bmatrix} \cos\theta & -\sin\theta \\ \sin\theta & \cos\theta \end{bmatrix} \begin{bmatrix} i_d \\ i_q \end{bmatrix} \tag{4.1}$$

On the contrary, the transformation from d, q reference to ABC reference is given by,

$$\begin{bmatrix} i_d \\ i_q \end{bmatrix} = \sqrt{\frac{2}{3}} \begin{bmatrix} \cos\theta & \sin\theta \\ -\sin\theta & \cos\theta \end{bmatrix} \begin{bmatrix} 1 & -\frac{1}{2} & -\frac{1}{2} \\ 0 & \frac{\sqrt{3}}{2} & -\frac{\sqrt{3}}{2} \end{bmatrix} \begin{bmatrix} i_A \\ i_B \\ i_C \end{bmatrix} \tag{4.2}$$

In order to keep the same power before and after the transformation, assuming the turns number of each phase A, B, C is N_3, while the turns number of d and q is N_2, then following equation should be ensured,

$$N_2 = \sqrt{\frac{3}{2}} N_3 \tag{4.3}$$

Besides, the inductances of d-axis L_d and q-axis L_q are calculated from,

$$L_d = \frac{\psi_d - \psi_m}{i_d} \tag{4.4}$$

$$L_q = \frac{\psi_q}{i_q} \tag{4.5}$$

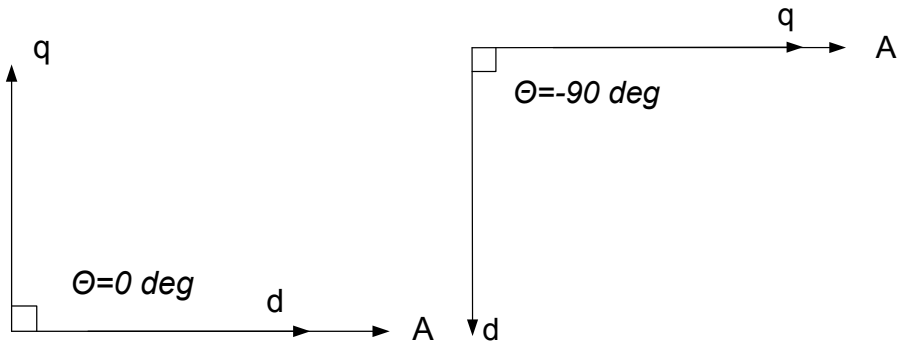

Figure 90 D, q flux passing through phase A

Thus, in Figure 90, when d-axis is lined up with the axis of phase A, the flux passing through coils of phase A is equal to

$$\phi_A = \phi_d \tag{4.6}$$

When q-axis is lined up with the axis of phase A, the flux passing through coils of phase A is equal to

$$\phi_A = \phi_q \tag{4.7}$$

The flux linkage is calculated by

$$\begin{aligned} \psi_d &= \phi_d N_2 \\ \psi_q &= \phi_q N_2 \\ \psi_A &= \phi_A N_3 \end{aligned} \tag{4.8}$$

Assuming that

$$\begin{aligned} i_A &= I \\ i_B &= -0.5I \\ i_C &= -0.5I \end{aligned} \tag{4.9}$$

According to the park transformation (4.2), when $\theta = 0$,

$$i_d = \sqrt{\frac{3}{2}} I = \sqrt{\frac{3}{2}} i_A \tag{4.10}$$

When $\theta = -90$,

$$i_q = \sqrt{\frac{3}{2}} I = \sqrt{\frac{3}{2}} i_A \tag{4.11}$$

Consequently, the d-axis inductance becomes

$$L_d = \frac{\psi_d - \psi_{m_{dq}}}{i_d} = \frac{\psi_A - \psi_{m_{abc}}}{i_A} \tag{4.12}$$

Neglecting the fluctuation of magnet working point caused by armature reaction, it can be assumed that

$$\psi_m = \psi_o \tag{4.13}$$

Where Ψ_0 is the flux linkage under no-load condition.

Similarly, the inductance of q-axis becomes,

$$L_q = \frac{\psi_q}{i_q} = \frac{\psi_A}{i_A} \tag{4.14}$$

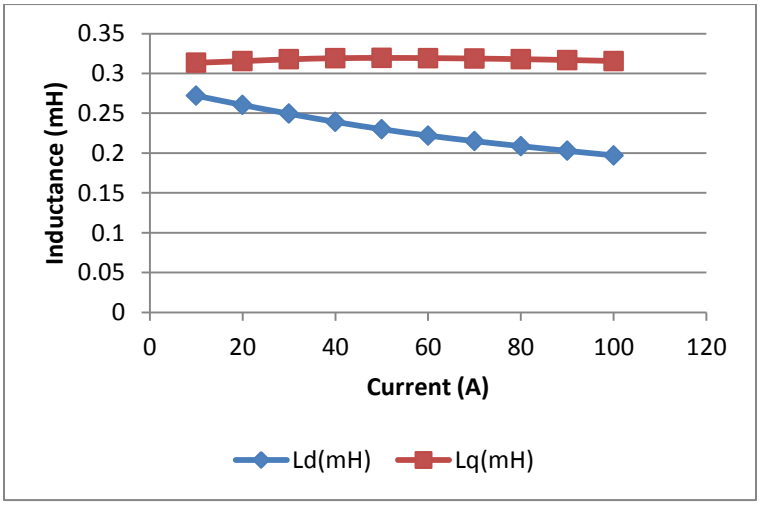

The phase inductance is calculated analytically as following,

$$L_d = L_{md} + L_\sigma - M_\sigma \tag{4.15}$$

Where,

L_{md}, is the magnetizing inductance,

L_σ, is the leakage inductance,

M_σ, is the mutual leakage inductance.

The leakage inductances have several components expressed as

$$L_\sigma = L_{Slot} + L_{diff} + L_{end} \tag{4.16}$$

$$M_\sigma = M_{Slot} + M_{diff} \tag{4.17}$$

Where,

L_{Slot}, is the slot leakage inductance,

L_{diff}, is differential leakage inductance,

L_{end}, is the end-winding inductance,

M_{Slot}, is the mutual slot leakage inductance,

M_{diff}, is the mutual differential leakage inductance.

Here, $L_{md} = 0.0364\text{mH}$, $L_{Slot} = 0.0689\text{mH}$, $L_{diff} = 0.1096\text{mH}$, $L_{end} = 0.0056\text{mH}$, $M_{Slot} = 0\text{mH}$, $M_{diff} = 0.012\text{mH}$. Then, $L_d = 0.2085\text{mH}$, which is a little bit lower than FEA result.

4.2 Performance evaluation

4.2.1 Back EMF calculation

Back EMF is also calculated in FEM method and analytical method at base speed. With the help of FLUX 2D, FEM calculation is implemented. The model of Design I in FLUX is presented in Figure 91 and its electric circuit is presented in Figure 92. The three-phase coils are connected with infinite value of resistor and the motor is dragged to rotate at 700rpm for at least one electric revolution. The three-phase back EMF results are presented in Figure 93.

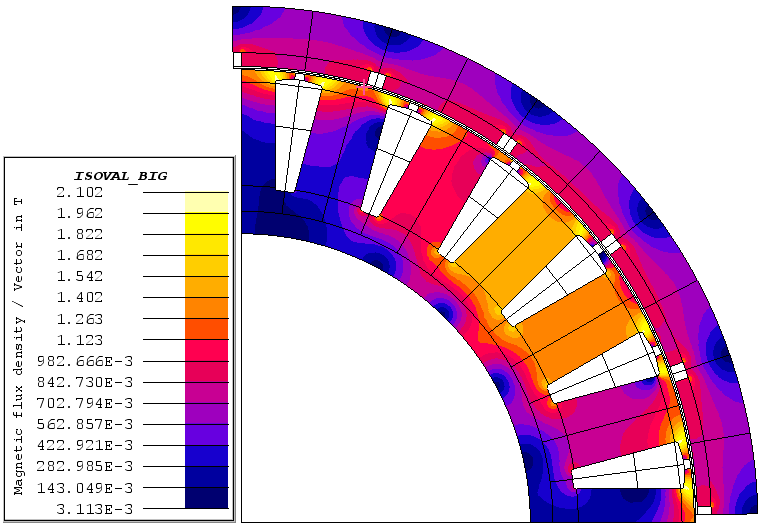

Figure 91 Model of Design I in FLUX

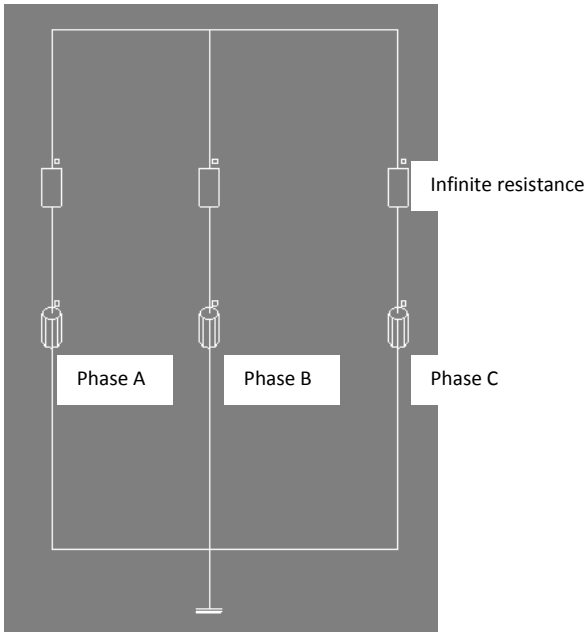

Figure 92 Electric circuit in FLUX

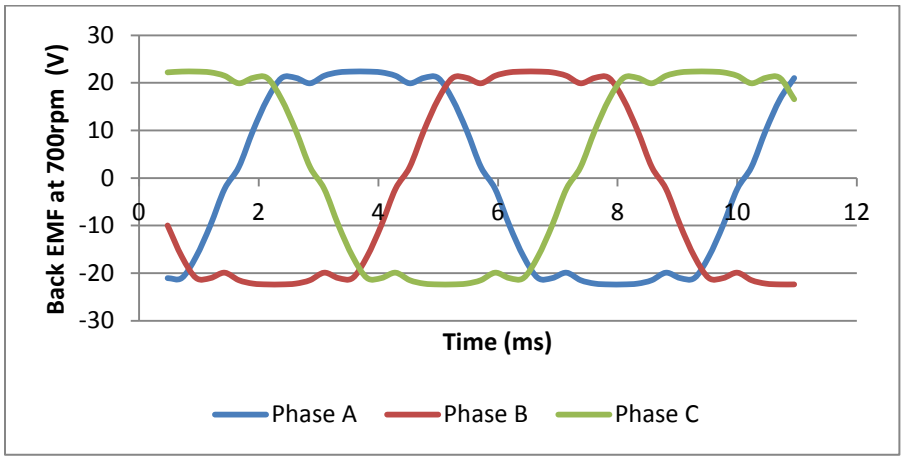

Figure 93 Three-phase back EMF in FLUX

The back EMF is also calculated analytically. First, according to 2.1, the open-circuit flux density distribution at the stator surface is given by

$$B_{roc}(\propto, t) = \widetilde{\Lambda_0} \sum_n B_n cosnp(\alpha - \alpha_{ma}) \tag{4.18}$$

The flux linkage through one stator coil is expressed by

$$\psi = \int_{-\alpha_y/2}^{\alpha_y/2} B_{roc}(\propto, t) R_s L_{stk} d\alpha \tag{4.19}$$

Where,

α_y, is the winding pitch angle, mec.rad,

R_s, is the radius of stator surface,

L_{stk}, is the length of the stator lamination.

It can be calculated the back EMF induced in one turn of a coil is

$$e_{turn} = -\frac{d\psi}{dt} = \widetilde{\Lambda_0} \sum_n 2B_n R_s L_{stk} \omega_r K_{dn} sinnp\alpha_{ma} \tag{4.20}$$

Where,

ω_r, is rotating speed, mec.rad/s,

K_{dn}, is the n-th winding pitch factor,

Hence, the induced back EMF of one phase is expressed as

$$e_{ph} = \widetilde{\Lambda_0} \sum_n 2T_{ph} B_n R_s L_{stk} \omega_r K_{dn} K_{pn} sinnp\alpha_{ma} \tag{4.21}$$

Where,

T_{ph}, is the number of serial turns per phase,

K_{dn}, is the n-th winding distributed factor.

The analytical result is presented in Figure 94 in comparison with FEM result.

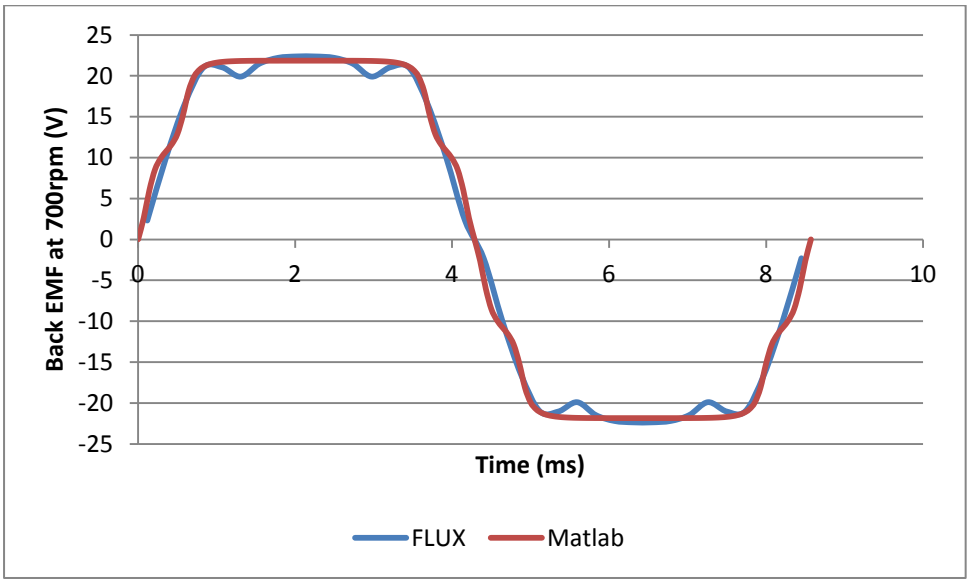

Figure 94 Comparison of back EMF between FEM and analytic results

4.2.2 Torque calculation

The analytic calculation of electromagnetic torque is validated by FEM. The electric circuit utilized for torque calculation in FLUX is presented in Figure 95. Two of the three-phase windings are connected to current sources. The amplitude, frequency and advanced angle are imported into the current sources to drive the motor in constant torque region or flux-weakening region. Five solid conductors are linked to five magnet blocks to calculate the magnet loss.

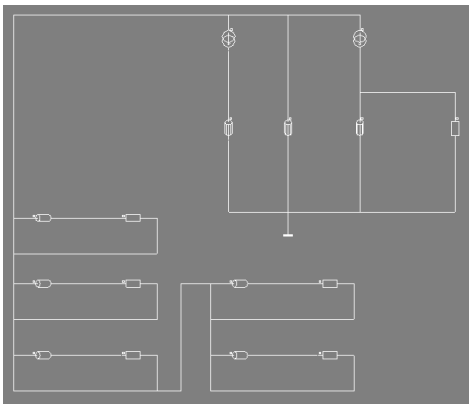

Figure 95 Electric circuit in FLUX

For Design I, when the amplitude of current is imposed as 224.3A at 667rpm with 0 current advanced angle, the waveform of electromagnetic torque is presented in Figure 96. The torque ripple is calculated to be 4.34%.

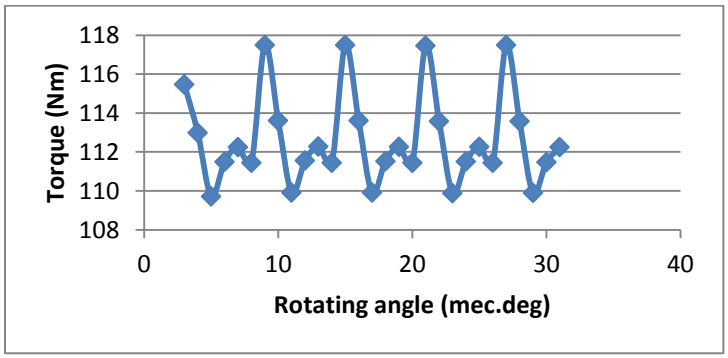

Figure 96 Electromagnetic torque calculated in FLUX

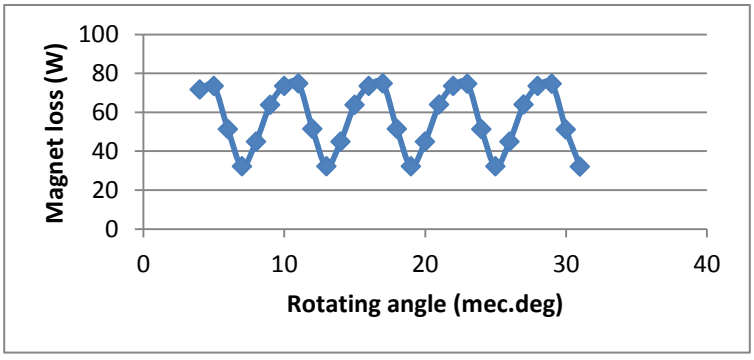

Figure 97 Magnet loss calculated in FLUX

The result of magnet loss calculated in FLUX is presented in Figure 97. Its mean value is 57.03W. Because this is the result of ¼ model, the total magnet loss is 228.12W.

Furthermore, according to 2.3, different values of input current and advanced angle are calculated and exported into current source in FLUX for Design I and Design II. The comparison of results is presented in Figure 98. The error is caused mainly by the error of phase inductance estimation and the error of open-circuit air gap flux density.

Table 32 Torque comparison of Design I

Speed		111rpm	333rpm	667rpm	1000rpm	1500rpm
Advanced angle γ (elec.deg)		0	0	0	35.40	53.41
Torque(Nm)	Analytical	119	119	119	97.03	66.04
	FEM	119.21	118.75	118.06	91.22	62.99
Design phase current amplitude: 224.29A FLUX phase current amplitude: 240.46A						

Table 33 Torque comparison of Design II

Speed		111rpm	333rpm	667rpm	1000rpm	1500rpm
Advanced angle γ (elec.deg)		0	0	0	33.74	53.38
Torque(Nm)	Analytical	119	119	119	98.98	71.03
	FEM	118.86	118.79	118.66	98.14	69.06
Design phase current amplitude: 74.76A FLUX phase current amplitude: 78.04A						

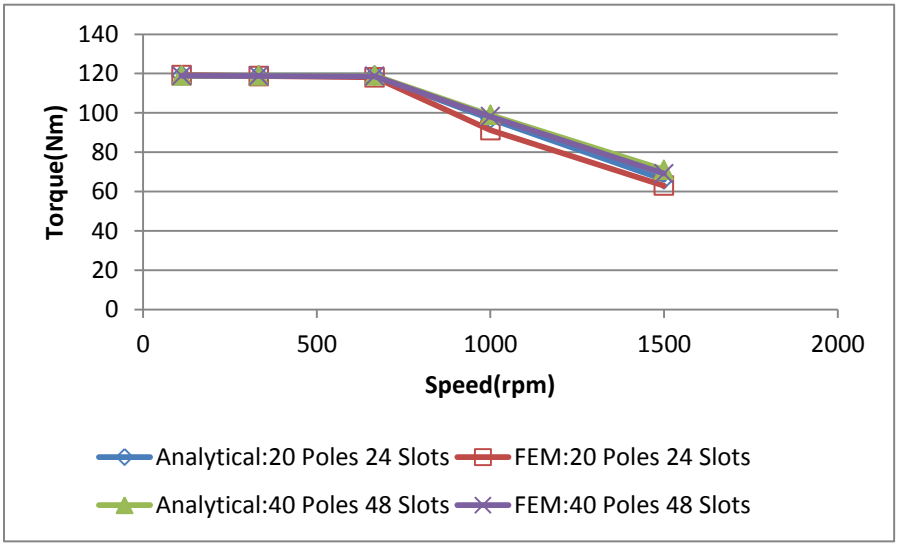

Figure 98 Comparison of torque-speed profile

4.2.3 Losses calculation

The transient magnetic solver in FLUX is used to calculate the iron loss and magnet loss. The results of Design I and Design II are presented in Table 34 and Table 35. The comparison is shown in Figure 99 and Figure 100. In order to deliver the same torque, the imposed phase current in FLUX is different from that of design value. This is caused by the error of open-circuit air gap flux density.

Modified Steinmetz equation is adopted to calculate iron loss as discussed in 2.5.2.1. It can be seen this method overestimates iron loss due to not considering the armature reaction effect precisely. Especially when the motor operation goes into high-speed region, the error of iron loss becomes bigger. However, this error only accounts for few percent of electromagnetic power. It will not influence the accuracy of the efficiency map very much.

In general, an acceptable agreement of losses calculation can be detected, especially under rated speed, to make reliable the evaluation of motor efficiency map.

Table 34 Losses comparison of Design I

Speed		111rpm	333rpm	667rpm	1000rpm	1500rpm
Advanced angle γ (elec.deg)		0	0	0	35.40	53.41
Stator iron loss(W)	Analytical	6.05	27.49	83.15	155.38	--
	FEM	7.68	32.24	92.36	132	--
Magnet loss(W)	Analytical	8.1	72.92	292.55	657.59	1280.6
	FEM	7.24	64	252.16	645.28	1544.16
Design phase current amplitude: 224.29A FLUX phase current amplitude: 240.46A						

Table 35 Losses comparison of Design II

Speed		111rpm	333rpm	667rpm	1000rpm	1500rpm
Advanced angle γ (elec.deg)		0	0	0	33.74	53.38
Stator iron loss(W)	Analytical	15.5	74.58	233.98	466.73	--
	FEM	16.08	79.12	251.84	350.16	--
Magnet loss(W)	Analytical	1.32	11.87	47.62	107.03	240.82
	FEM	1.52	13.76	54.08	117.92	252.16
Design phase current amplitude: 74.76A FLUX phase current amplitude: 78.04A						

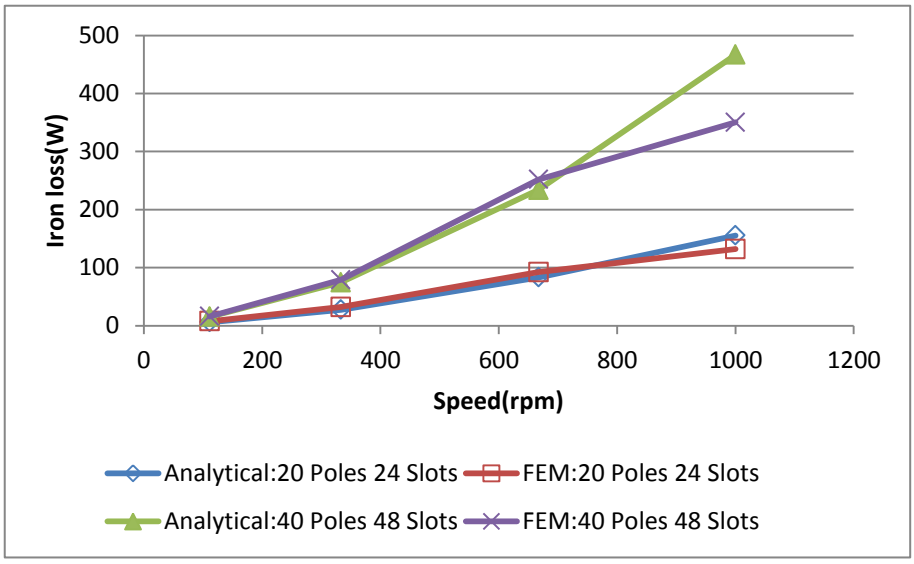

Figure 99 Comparison of iron loss

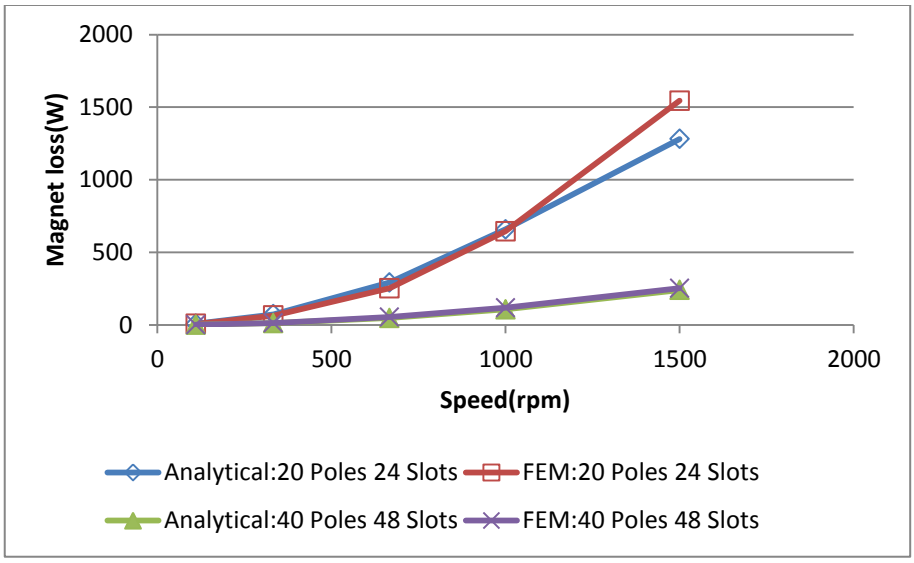

Figure 100 Comparison of magnet loss

4.3 Flux-weakening control in Portunus

In order to know the motor performance under real driving cycle, motor control model is built in Portunus, which can be used to co-simulink with Flux 2D. The variation of losses and efficiency can be known in real time.

The control theory has been discussed in 2.4. It is implemented as shown in Figure 101 in the block of "i_d^*, i_q^* reference generator" [88], [89]. The block of "Speed regulator" is an anti-windup PI regulator, which generates torque reference from speed error. The d,q voltage references are calculated from d,q current references based on the equations of (2.61) and (2.62). Both voltage references, together with rotor position, are sent to the block of "Space Vector Modulation (SVM)" to generate PWM signal [90].

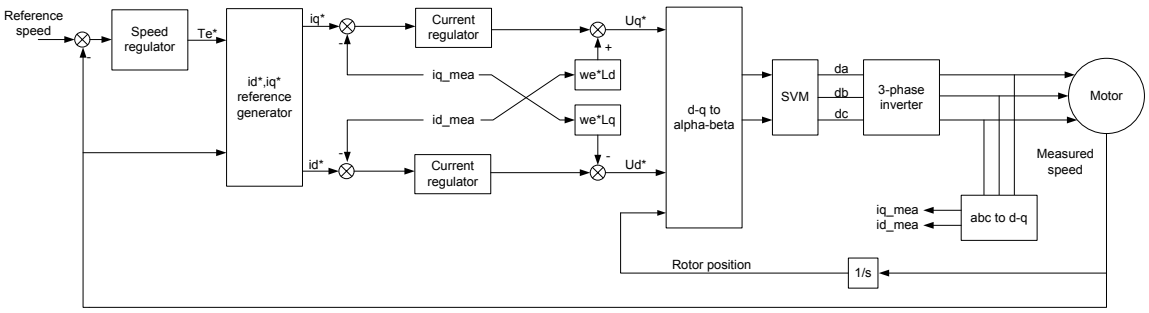

Figure 101 Motor control schematic diagram

4.3.1 Current loop

The transfer function of the current regulator is given by

$$G_{id,iq}(s) = K_{mp} + \frac{K_{mp}}{T_{mi}s} \tag{4.22}$$

The i_d, i_q current loop can be presented as Figure 102 [91]. Several delays are introduced including

- the delay due to control algorithm with the time constant $T_{sw} = \frac{1}{f_{sw}}$, where f_{sw} is sampling frequency equal to 10kHz, thus $T_{sw} = 0.1\text{ms}$;
- the delay due to the sampling and holding with the time constant equal to $0.5T_{sw} = 0.05\text{ms}$;
- the delay due to the modulation and the inverter with the time constant equal to $0.5T_{sw} = 0.05\text{ms}$.

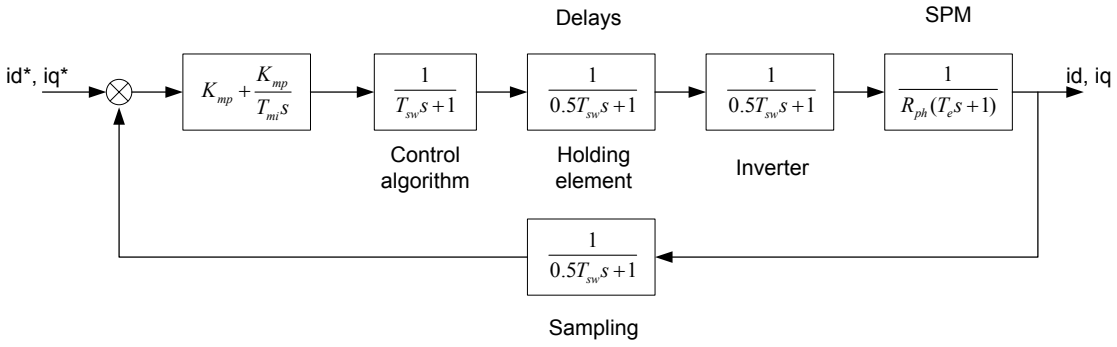

Figure 102 Current loop

From Figure 102, the transfer function of open current loop with unity feedback can be expressed as

$$G_{oltf} = (K_{mp} + \frac{K_{mp}}{T_{mi}s}) \cdot \frac{1}{0.5T_{sw}s+1} \cdot \frac{1}{T_{sw}s+1} \cdot \frac{1}{0.5T_{sw}s+1} \cdot \frac{1}{0.5T_{sw}s+1} \cdot \frac{1}{R_{ph}(T_e s+1)} \tag{4.23}$$

From the root loci of the open loop transfer function, it can be deduced that

$$T_{mi} = T_e = \frac{L_d}{R_{ph}} \tag{4.24}$$

For the motor of Design I in Table 29, $L_d = 0.2085$ mH, $R_{ph} = 0.0059$ Ohm. Thus, $T_{mi} = 35.34$ ms.

Consequently, the open loop transfer function can be approximated with one equivalent time constant,

$$G_{oltf} = \frac{K_{mp}}{T_{mi}s} \cdot \frac{1}{R_{ph}(T_{se}s+1)} \tag{4.25}$$

Where,

$$T_{se} = 3 \cdot 0.5T_{sw} + T_{sw} = 2.5T_{sw} = 0.25ms$$

According to Optimal Modulus design criterion, the gain of the current regulator is found

$$K_{mp} = \frac{R_{ph}T_{mi}}{2T_{se}} = \frac{0.0059 \times 35.34}{2 \times 0.25} = 0.417$$

Because d, q inductances are almost equal for SPM machine, the coefficients of d, q current regulators can have the same values.

Furthermore, the equivalent time constant of current loop needs to be calculated for speed loop as a delay. The equivalent closed loop transfer function of current loop is expressed as

$$G_{cltf} = \frac{1}{1 - 0.5T_{sw}s} \cdot \frac{1}{2T_{se}^2 s^2 + 2T_{se}s + 1} \tag{4.26}$$

The second order term is neglected so that the equivalent time constant of the current loop is estimated as

$$T_i = 2T_{se} - 0.5T_{sw} = 0.45\text{ms}$$

4.3.2 Speed loop

The transfer function of the speed regulator is given by

$$G_{speed}(s) = K_{sp} + \frac{K_{sp}}{T_{si}s} \tag{4.27}$$

Before building up the speed loop, it is necessary to know the mechanical equation of SPM motor,

$$T_{em} - T_L - B\omega_m = J\frac{d\omega_m}{dt} \tag{4.28}$$

Where,

T_{em}, is the electromagnetic torque, Nm,

T_L, is the load torque, Nm,

B, is the viscous friction coefficient, Nm/rad/s,

J, is the total rotating moment of electric motor and the wheel, Nm/rad/s^2,

ω_m, is the mechanical speed, mec.rad/s.

According to 3.1, the rotating moment of the wheel is 3.718Nm/rad/s^2. It can also be calculated that the rotating moment of the in-wheel motor, Design I, is 0.1236Nm/rad/s^2. Thus, $J = 3.718 + 0.1236 = 3.8416\text{Nm/rad/s}^2$.

If B is neglected, the mechanical equation is simplified as,

$$T_{em} - T_L = \frac{J}{p}\frac{d\omega_e}{dt} \tag{4.29}$$

Where, $\omega_e = p\omega_m$.

In the frequency domain, it can be expressed as

$$T_{em}(s) - T_L(s) = \frac{J}{p}\omega_e(s) \cdot s \tag{4.30}$$

Then, the speed loop is presented in Figure 103.

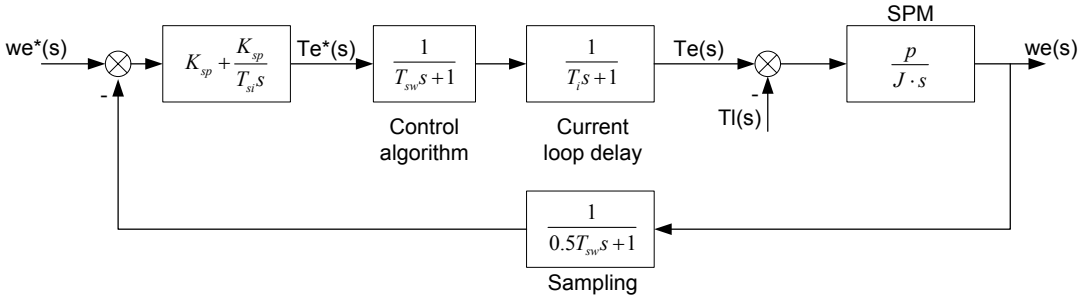

Figure 103 Speed loop

The delays considered in speed loop are:

- the delay due to the control algorithm, $T_{sw} = 0.1\text{ms}$;
- the delay due to the current loop, $T_i = 0.45\text{ms}$;
- the delay due to the sampling, which has the time constant $0.5T_{sw} = 0.05\text{ms}$.

There are two inputs to the speed loop: the reference speed ω_e^* and load torque T_L. In order to configure the proper coefficients of speed regulator, one of the inputs is considered as 0. When $T_L = 0$, the speed loop can be presented Figure 104. For this case, only the proportional gain of speed regulator K_{sp} is considered.

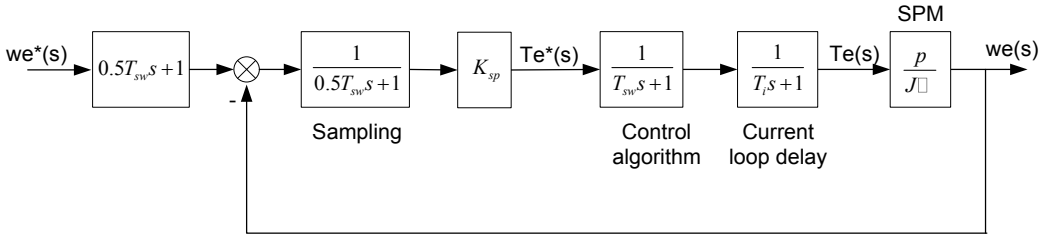

Figure 104 Speed loop when Tl=0

Thus, the open loop transfer function has the following expression,

$$G_{oltf} = K_{sp}\frac{1}{0.5T_{sw}s+1}\frac{1}{T_{sw}s+1}\frac{1}{T_{is}s+1}\frac{p}{Js} \tag{4.31}$$

As similar as aforementioned, the delays are approximated to one delay with the time constant equal to

$$T_{se} = 1.5T_{sw} + T_{is} = 0.6\text{ms}$$

The open loop transfer function becomes

$$G_{oltf} = K_{sp}\frac{1}{T_{se}s+1}\frac{p}{Js} \tag{4.32}$$

According to Optimal Modulus design criterion, the gain of the speed regulator is found

$$K_{sp} = \frac{J}{2pT_{se}} = \frac{3.8416}{2\times 10\times 0.6\text{e}-3} = 320.133$$

When $T_L = 0$, the speed loop can be presented Figure 105.

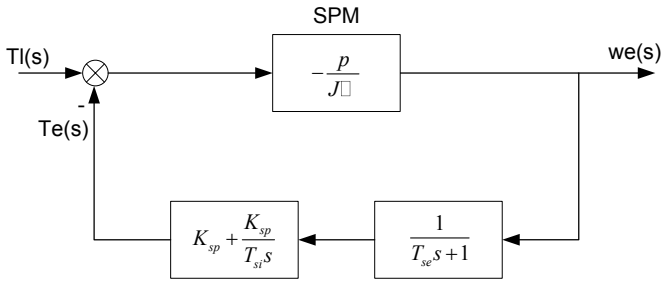

Figure 105 Speed loop when we*=0

The closed loop transfer function of Figure 105 is given by

$$G_{cltf} = \frac{-\frac{pT_{si}}{J}T_{se}s(T_{se}s+1)}{2T_{se}^2T_{si}s^3 + 2T_{se}T_{si}s^2 + T_{si}s + 1} \tag{4.33}$$

With the Symmetric Optimum method, T_{si} can be obtained as

$$T_{si} = 4T_{se} = 2.4\text{ms}$$

In sum, the coefficients of speed regulator and current regulator are listed in Table 36.

Table 36 Coefficients of PI regulator

Speed regulator		Current regulator	
K_{sp}	T_{si}(s)	K_{mp}	T_{mi}(s)
320.133	2.4e-3	0.417	35.34e-3

Finally, the SPM motor control strategy is realized in Portunus as shown in Figure 106. The motor controller needs inputs of reference speed, feedback speed and rotor position, feedback 3 phase currents. The controller will generate reference values of voltage in $\alpha - \beta$ coordinate, which are sent to 3-phase Space Vector Modulation (SVM) inverter [92]. The input currents of SPM motor and the shaft torque are measured for feedback. The friction torque including ground friction torque and wind dragging torque are generated and imposed as load torque on the shaft.

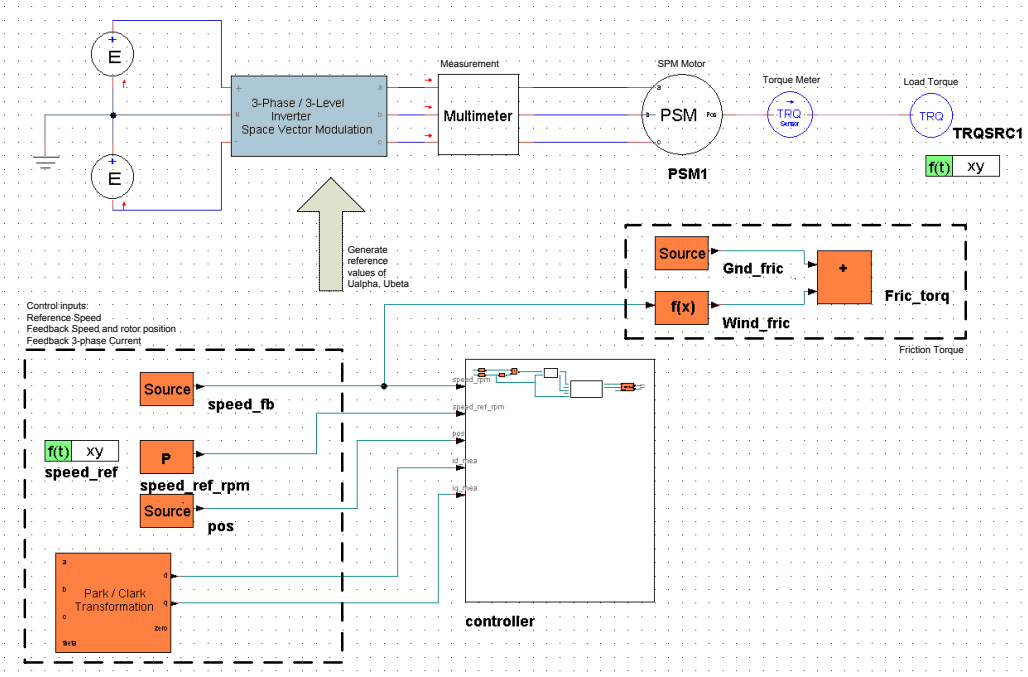

Figure 106 SPM motor control in Portunus

Assuming the road grade is 0 degree, ground friction torque of each wheel is calculated as

$$T_{gnd} = \frac{Mgf_r r}{4} = 1100 \times 9.8 \times 0.009 \times 0.282 \div 4 = 6.84\text{Nm}$$

While the wind dragging torque of each wheel is

$$T_{wnd} = \frac{\frac{1}{2}\rho_a C_D A_f V^2 r}{4} = \frac{\frac{1}{2} \times 1.202 \times 0.335 \times 2 \times (\frac{n \times 0.377 \times 0.282}{3.6})^2 \times 0.282}{4}$$
$$= 2.476\text{e} - 5 \cdot n^2$$

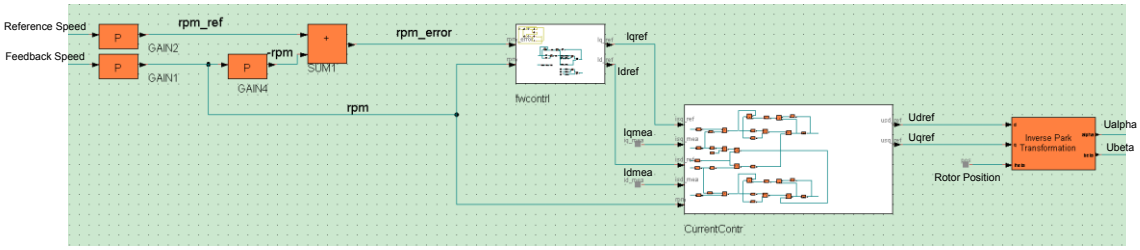

Figure 107 Controller subsystem

The inside of controller in Figure 106 is presented in Figure 107. It is composed by two main blocks, flux-weakening controller ("fwcontrl") and current controller ("CurrentContr"). Flux-weakening controller serves to generate reference values of d, q components of input current. It includes speed regulator and d, q current generator as shown in Figure 101. Current controller serves to generate reference values of d, q voltage. It includes current regulator and d, q voltage calculation inside.

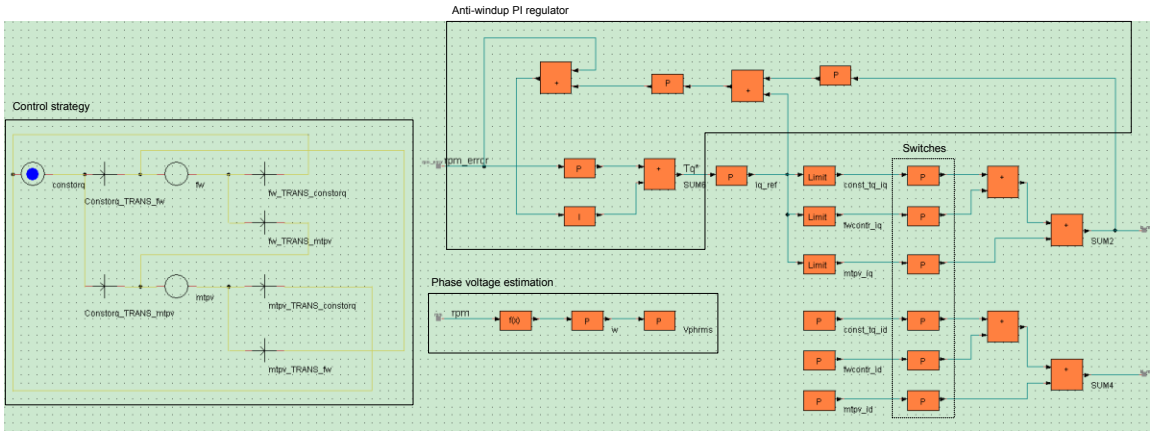

Figure 108 Flux-weakening controller

Inside Flux-weakening Controller, direct flux-weakening control strategy is implemented. According to the estimation of d-axis current and phase voltage, the block of "Control strategy" will activate or deactivate corresponding switches to make the motor operation transfer among MTPA region, Flux-weakening region and MTPV region.

The first round test is implemented to make the motor accelerate from 0km/h to 100km/h, which is from 0rpm to 941rpm, considering the ground friction and wind friction as load on the shaft. It can be observed that the motor accelerates to 941rpm within 3.85 seconds as shown in Figure 109 Speed and torque. The shaft torque is equal to the total friction torque. After 1.814 seconds, the operation of motor transfer from MTPA control to flux-weakening control as indicated in Figure 111, which presents the status of motor operation mode switches.

The requested speed and torque are imported into the model to check whether the electric drive system can satisfy load request dynamically. Figure 112 (blue line represents load request, red line represents motor output) indicates that the output torque and speed can track load request very well.

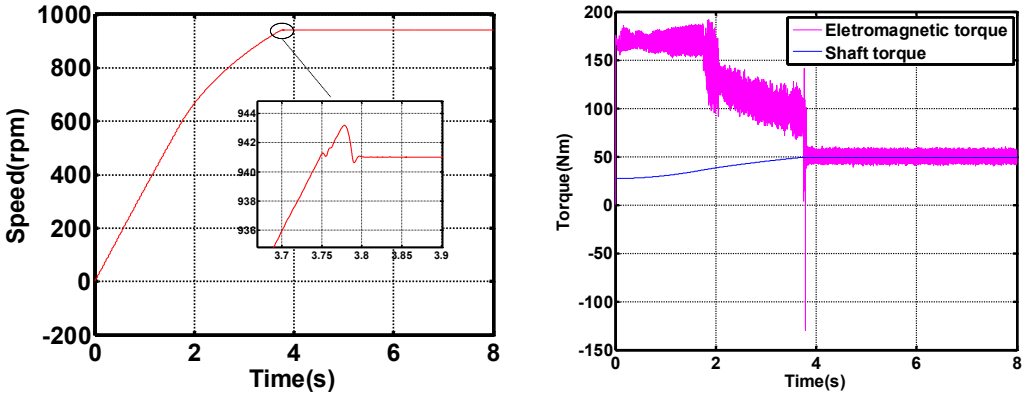

Figure 109 Speed and torque

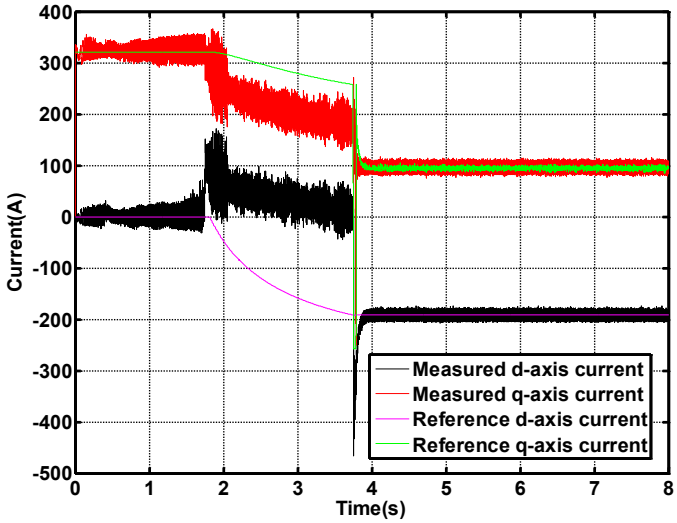

Figure 110 Measured and reference d, q current

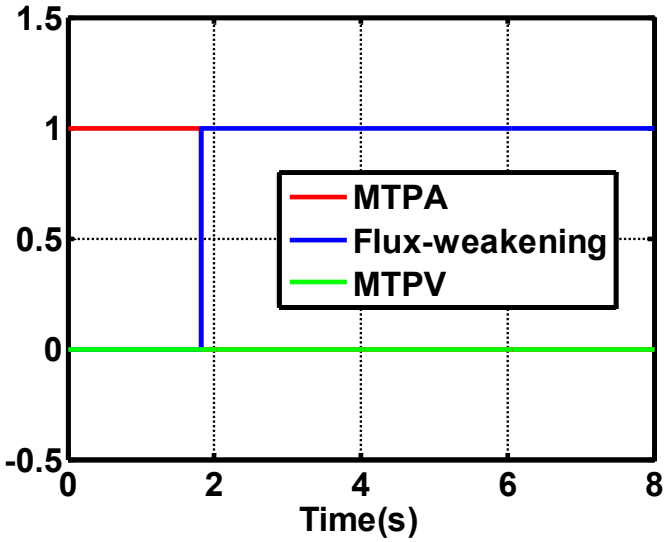

Figure 111 Motor operation mode switches

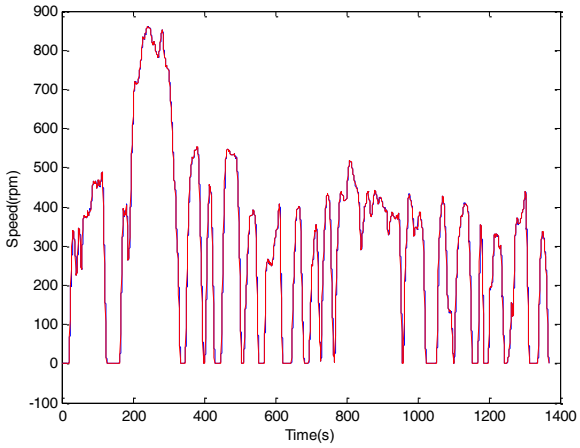

Figure 112 Load request of UDDS and motor output

4.4 Co-simulation of Portunus and Flux 2D

In co-simulation, the model of electric motor is replaced by FLUX model as shown in Figure 113. The electric circuit in FLUX needs to be modified as Figure 114. The voltage from Portunus is imposed on the phase coils in FLUX as shown in Figure 114and the current is fed back to the inverter as an equivalent current source in Portunus. The length of co-simulation time varies greatly depending on the setup of step time.

The final objective is to calculate the variation of different losses within one driving cycle. With the loss changing with time, the dynamic temperature rise can be predicted. Future work will also consider the thermal effect on motor performance. A multi-physics simulation of transient electromagnetic calculation coupled with transient thermal calculation will be implemented based on this co-simulation model.

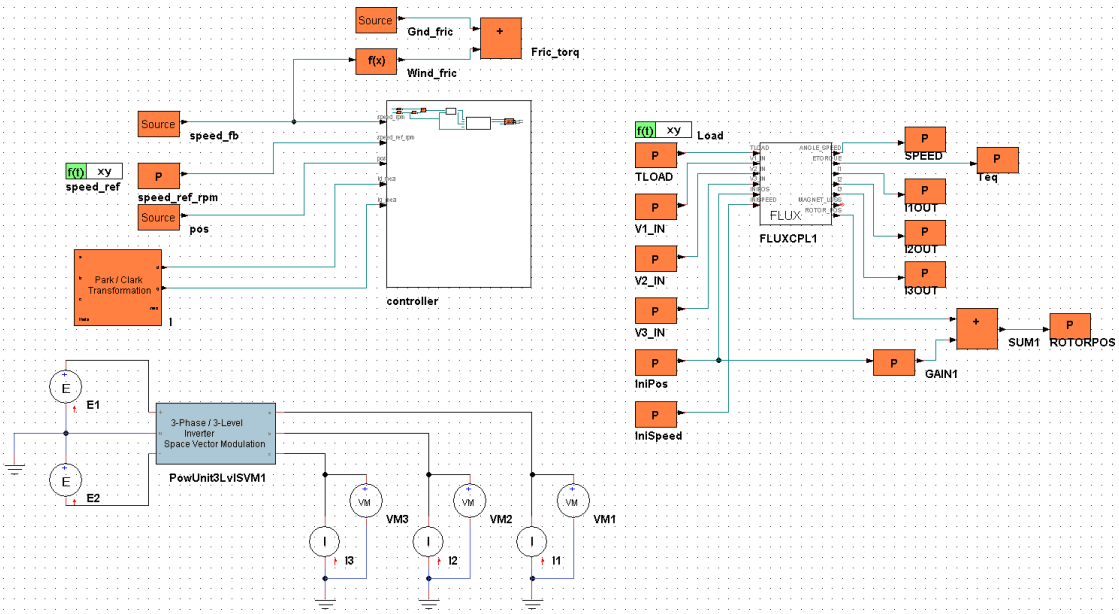

Figure 113 Co-simulation in Portunus

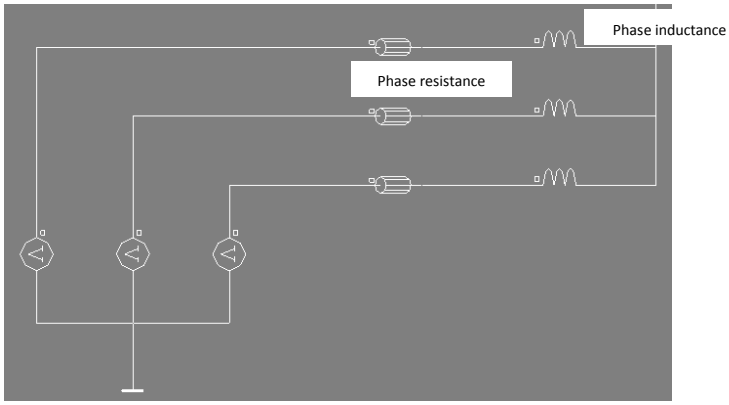

Figure 114 Electric circuit for co-simulation in FLUX

CHAPTER V

PROTOTYPE AND EXPERIMENT RESULTS

A 10kW prototype of concentrated-winding fractional-slot SPM motor with 28 poles 24 slots is manufactured. The view of the prototype is shown in Figure 115. It has six phases with double-layer windings. But the double-layer six-phase windings can also be connected into single-layer three-phase windings as indicated in Figure 116.

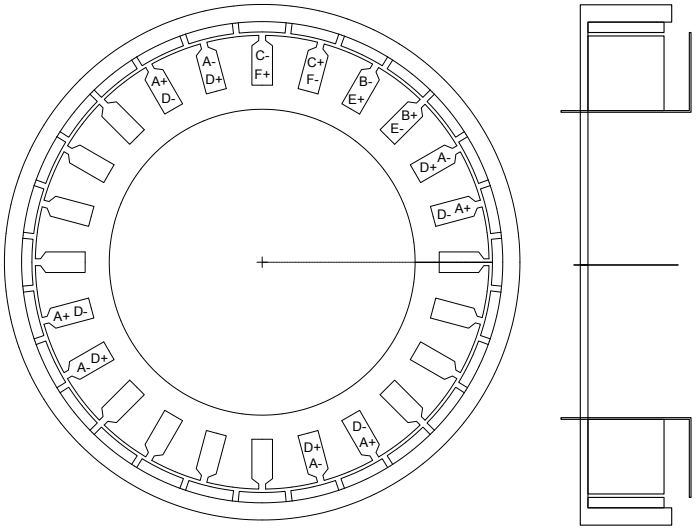

Figure 115 View of SPM prototype

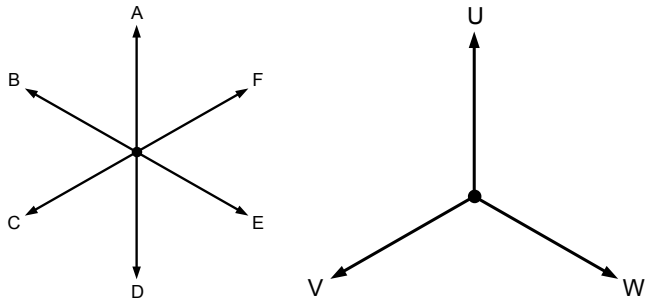

Figure 116 Phase angle diagram of six phase and three phase

The prototype is used for high-speed application. Its rated speed is 2400rpm. Hence, the parallel slot shape is adopted to accommodate Liz wire for weakening the skin effect at high frequency. Although this prototype is not manufactured for in-wheel application, it has the same structure to the motor which is studied in this thesis like external rotor, surface mounted magnet and the same type of winding layout. Thus, the experimental results can be utilized to validate the analytical results. So far the experiments are still on progress. In this chapter some primary experimental results will be presented and compared with analytical calculation. Table 37 presents the design parameters of the prototype.

Table 37 Design parameters of the prototype

Phase number, m	6
Pole pairs, p	14
Slot number, Q_s	24
Magnet material	SM-26U
Relative permeability, μ_r	1.02
Remanence, B_r	0.9 T
Air gap flux density, B_g	0.64T
Lamination material	Cogent NO-20 Laminated 2mm
Magnet arc, $\propto_m$	160 elec.deg
Winding factor, k_{wp}	0.966
Turns per coil, N	8
Filling factor, k_{fill}	40%
Base speed, n_N	2400rpm
Rated torque, T_N	40Nm
Magnet length, L_m	6mm
Air gap, g	2mm
Slot opening, b_0	4mm
Stator diameter, D	264mm
Length of lamination, L_{stk}	44mm
Peak phase current, I_p	43.83A
Rms phase voltage, V_{rms}	120V
Phase inductance, L_d	0.526mH
Current density @40Nm, J	4 A/mm^2
Cooling condition	Air cooling
Insulation class	Class H

Based on the slot star shown in Figure 117, motor's winding layout can be identified. Its winding factors are calculated until 100th harmonics in Figure 118. The manufactured stator and rotor are shown in the photo Figure 119.

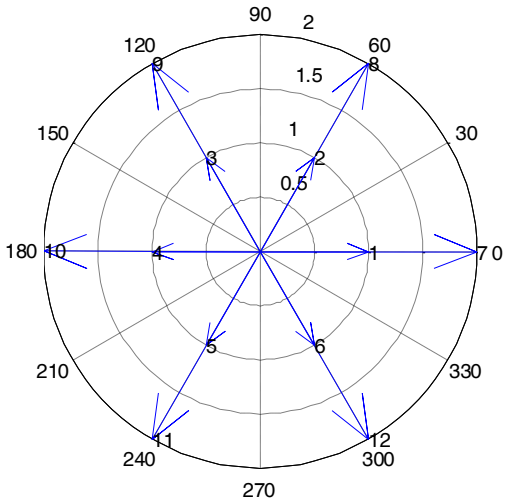

Figure 117 Slot star of 24-slot 28-pole fractional-slot concentrated winding

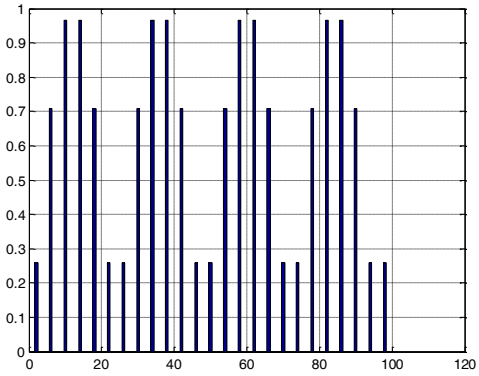

Figure 118 Winding factors for all the harmonics

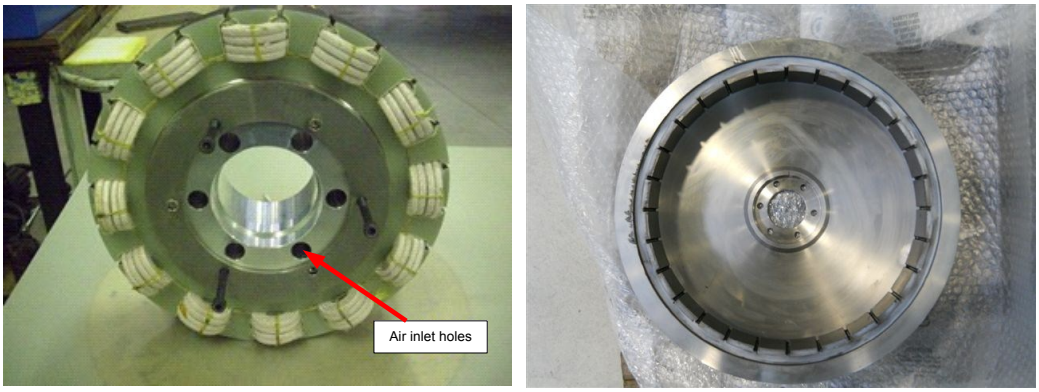

Figure 119 Rotor and stator of the prototype

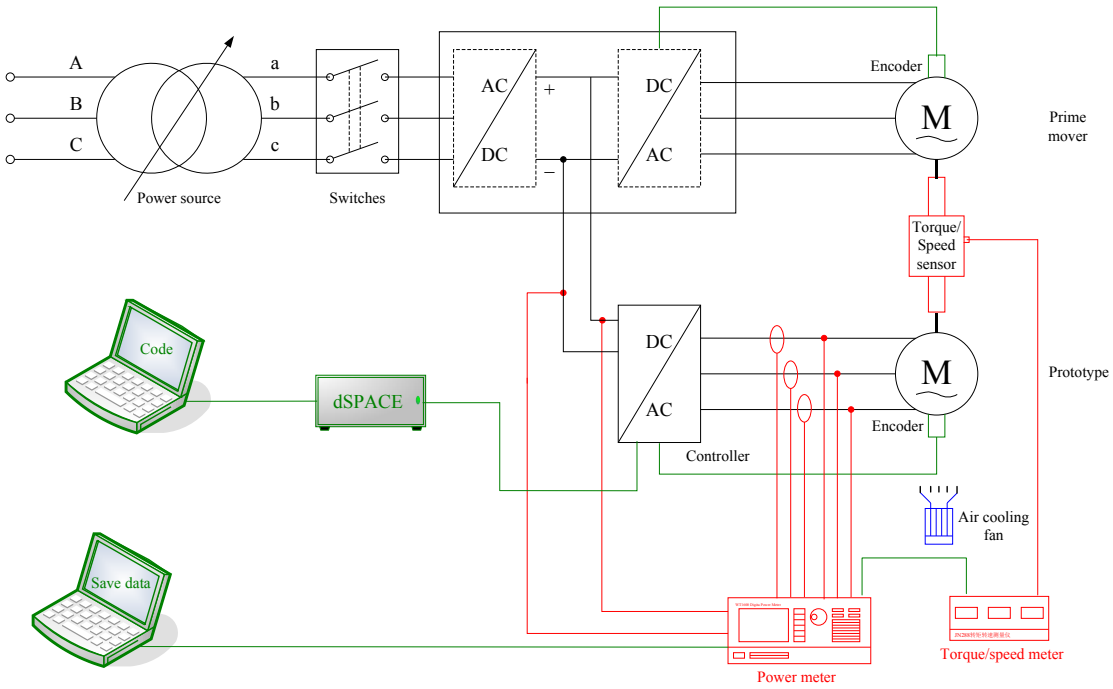

Figure 120 Scheme of test bench

The test bench for the prototype is built up as shown in Figure 120. Figure 121 displays the prototype mounted on the test bench. The air inlet hole, air outlet window and resolver can be seen from the photos. The cooling air generated by fan passes though air inlet hole, stator, end-winding, air gap and air outlet window as presented in Figure 122. The winding can be visualized through the air outlet window made by glass as well as its temperature can be measured by infrared thermal meter.

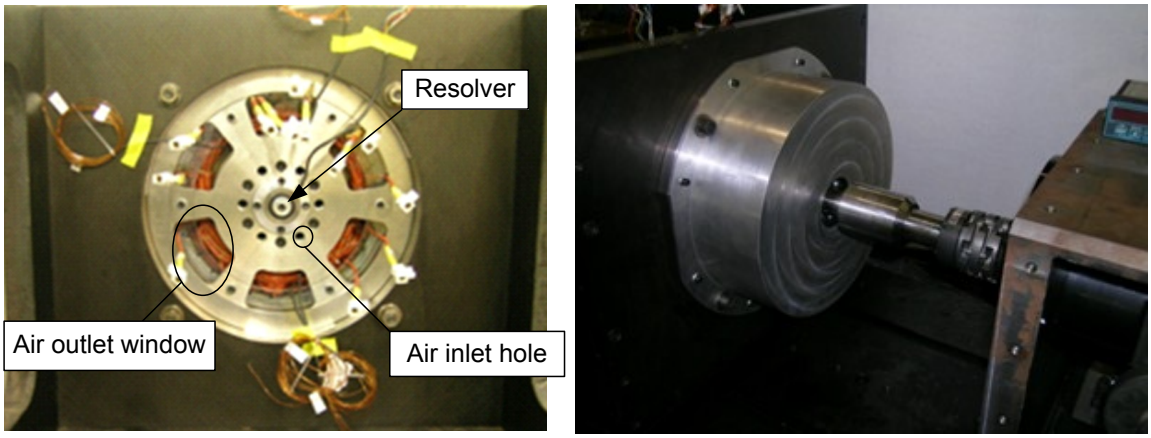

Figure 121 The prototype mounted on test bench

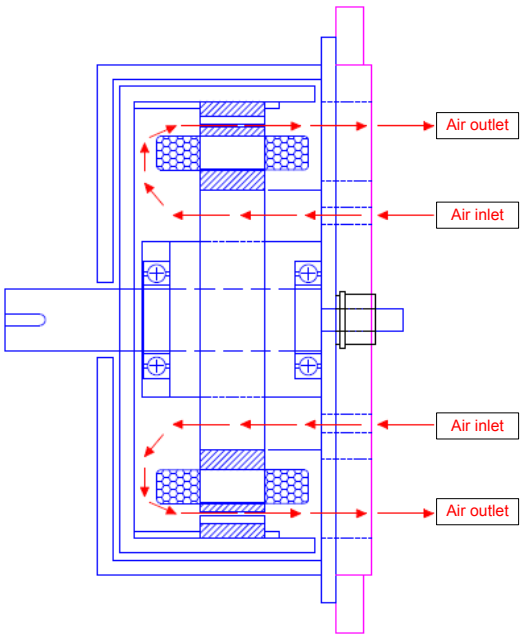

Figure 122 Passage of cooling air

Some preliminary tests have been completed. The phase resistance under ambient temperature is measured as shown in Table 38. The error is possibly caused by the estimation of end-winding length and the contact resistance between Liz wire and leading wire. The back EMF at base speed

2400rpm is measured and compared with FEM results and analytic results as shown in Figure 123. They make a good agreement. The back EMF at other speed is also measured to calculate its back EMF factor as shown in Figure 124. The experimental result of 0.1066V.rms/Hz agrees well with the design value of 0.0922V.rms/Hz.

Table 38 Phase resistance at 20 C

Design value	14.95mΩ
Measured value	20.15mΩ

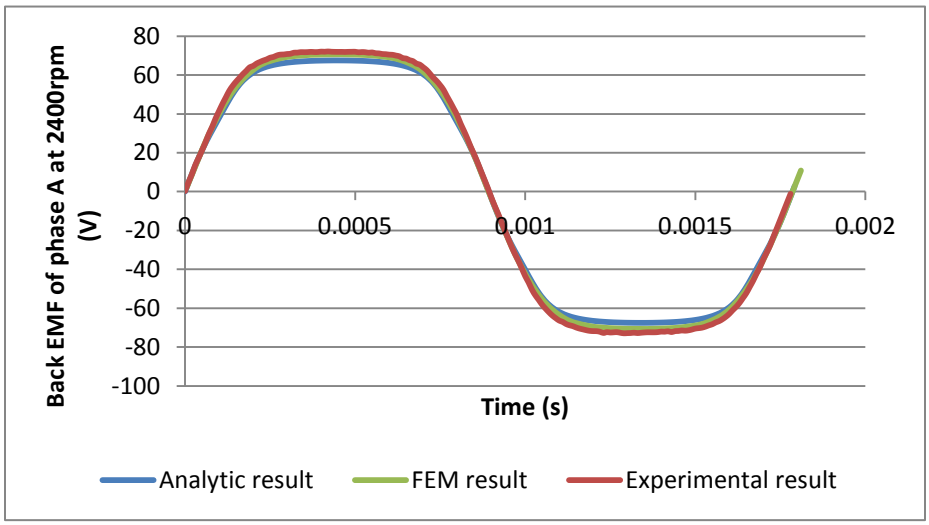

Figure 123 Back EMF comparison of phase A at 2400rpm

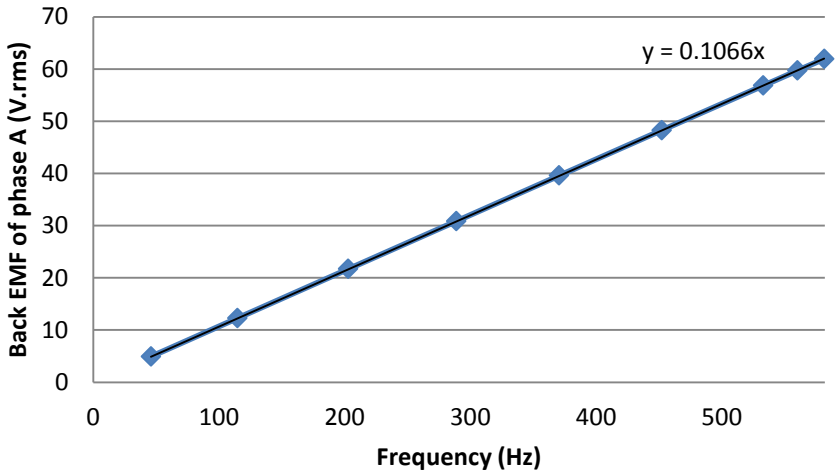

Figure 124 Back EMF at different speed

REFERENCES

[1] Kamiya, "Development of Traction Drive Motors for the Toyota Hybrid System," *IEEJ Transactions on Industry Applications*, vol. 126, no. 4, pp. 473-479, 2006.

[2] Mitch Olszewski, "EVALUATION OF THE 2010 TOYOTA PRIUS HYBRID SYNERGY DRIVE SYSTEM," Oak Ridge National Laboratory, Mar. 2011.

[3] Mitch Olszewski, "EVALUATION OF THE 2007 TOYOTA CAMRY HYBRID SYNERGY DRIVE SYSTEM," Oak Ridge National Laboratory, Apr. 2008.

[4] Mitch Olszewski, "Evaluation of 2004 Toyota Prius Hybrid Electric Drive System," Oak Ridge National Laboratory, May 2005.

[5] R. H. Staunton, S. C. Nelson, P. J. Otaduy, J. W. McKeever, J. M. Bailey, S. Das, and R. L. Smith, "PM Motor Parametric Design Analyses for a Hybrid Electric Vehicle Traction Drive Application," OAK RIDGE NATIONAL LABORATORY, Sep. 2004.

[6] Karl H. Hellman, Maria R. Peralta, and Gregory K. Piotrowski, "Evaluation of a Toyota Prius Hybrid System (THS)," United States Environmental Protection Agency, Aug. 1998.

[7] J. S. Hsu, C. W. Ayers, and C. L. Coomer, "REPORT ON TOYOTA/PRIUS MOTOR DESIGN AND MANUFACTURING ASSESSMENT," OAK RIDGE NATIONAL LABORATORY, Oak Ridge,Tennessee 37831, Jul. 2004.

[8] Laura D. Marlino, "REPORT ON TOYOTA PRIUS MOTOR THERMAL MANAGEMENT," OAK RIDGE NATIONAL LABORATORY, Oak Ridge,Tennessee 37831, Feb. 2005.

[9] Mitch Olszewski, "REPORT ON TOYOTA/PRIUS MOTOR TORQUE CAPABILITY,TORQUE PROPERTY, NO-LOAD BACK-EMF,AND MECHANICAL LOSSES–REVISED MAY 2007," OAK RIDGE NATIONAL LABORATORY, Oak Ridge,Tennessee 37831, May 2007.

[10] SERGIO ROMERO P ´ EREZ, "Analysis of a light permanent magnet in-wheel motor for an electric vehicle with autonomous corner modules," Royal Institute of Technology, Stockholm, Sweden, Feb. 2011.

[11] "Siemens VDO visualises the electric wheel hub motor." [Online]. Available: http://www.gizmag.com/go/5996/. [Accessed: 17-Nov-2011].

[12] "Hybrid Cars | Protean Electric." [Online]. Available: http://www.proteanelectric.com/index.html. [Accessed: 17-Nov-2011].

[13] Z. Q. Zhu and D. Howe, "Electrical Machines and Drives for Electric, Hybrid, and Fuel Cell Vehicles," *Proceedings of the IEEE DOI - 10.1109/JPROC.2006.892482*, vol. 95, no. 4, pp. 746-765, 2007.

[14] A. Vagati, A. Fratta, G. Franceschini, and P. Rosso, "AC motors for high-performance drives: a design-based comparison," *Industry Applications, IEEE Transactions on DOI - 10.1109/28.536885*, vol. 32, no. 5, pp. 1211-1219, 1996.

[15] K. T. Chau, C. C. Chan, and Chunhua Liu, "Overview of Permanent-Magnet Brushless Drives for Electric and Hybrid Electric Vehicles," *Industrial Electronics, IEEE Transactions on DOI - 10.1109/TIE.2008.918403*, vol. 55, no. 6, pp. 2246-2257, 2008.

[16] A. Fratta, A. Vagati, and F. Villata, "On the evolution of AC machines for spindle drive applications," in *Industry Applications Society Annual Meeting, 1989., Conference Record of the 1989 IEEE*, 1989, pp. 699-704 vol.1.

[17] X. D. Xue, K. W. E. Cheng, T. W. Ng, and N. C. Cheung, "Multi-Objective Optimization Design of In-Wheel Switched Reluctance Motors in Electric Vehicles," *Industrial Electronics, IEEE Transactions on DOI - 10.1109/TIE.2010.2051390*, vol. 57, no. 9, pp. 2980-2987, 2010.

[18] F. Profumo, Zheng Zhang, and A. Tenconi, “Axial flux machines drives: a new viable solution for electric cars,” *Industrial Electronics, IEEE Transactions on DOI - 10.1109/41.557497*, vol. 44, no. 1, pp. 39-45, 1997.
[19] D. Luque, E. Ruppert, N. Bianchi, and M. Castiello, “Analysis of a three-phase in-wheel electric motor,” in *Universities Power Engineering Conference (UPEC), 2009 Proceedings of the 44th International*, 2009, pp. 1-5.
[20] W. Jiabin, K. Atallah, Z. Q. Zhu, and D. Howe, “Modular Three-Phase Permanent-Magnet Brushless Machines for In-Wheel Applications,” *Vehicular Technology, IEEE Transactions on*, vol. 57, no. 5, pp. 2714-2720, 2008.
[21] P. Asko, “Design of axial-flux permanent-magnet low-speed machines and performance comparison between radial-flux and axial-flux machines,” Lappeenranta University of Technology, 2005.
[22] A. Cavagnino, M. Lazzari, F. Profumo, and A. Tenconi, “A comparison between the axial flux and the radial flux structures for PM synchronous motors,” *Industry Applications, IEEE Transactions on DOI - 10.1109/TIA.2002.805572*, vol. 38, no. 6, pp. 1517- 1524, 2002.
[23] F. G. Jacek, W. Rong-jie, and J. K. Maarten, *Axial Flux Permanent Magnet Brushless Machines*. Dordrecht,The Netherlands: Kluwer Academic Publishers, 2004.
[24] A. M. El-Refaie, “Fractional-Slot Concentrated-Windings Synchronous Permanent Magnet Machines: Opportunities and Challenges,” *Industrial Electronics, IEEE Transactions on*, vol. 57, no. 1, pp. 107-121, 2010.
[25] EL-Refaie, A.M., and T. M. Jahns, “Optimal flux weakening in surface PM machines using fractional-slot concentrated windings,” *Industry Applications, IEEE Transactions on*, vol. 41, no. 3, 2005.
[26] N. Bianchi and M. D. Pre, “Design considerations for fractional-slot winding configurations of synchronous machines,” *Industry Applications, IEEE Transactions on*, 2006.
[27] A. M. El-Refaie, T. M. Jahns, P. J. McCleer, and J. W. McKeever, “Experimental verification of optimal flux weakening in surface PM Machines using concentrated windings,” *Industry Applications, IEEE Transactions on*, vol. 42, no. 2, pp. 443-453, 2006.
[28] J. D. Ede, K. Atallah, J. B. Wang, and D. Howe, “Modular fault-tolerant permanent magnet brushless machines,” in *Power Electronics, Machines and Drives, 2002. International Conference on (Conf. Publ. No. 487)*, 2002, pp. 415- 420.
[29] B. C. Mecrow, A. G. Jack, and J. A. Haylock, “Fault tolerant permanent magnet machine drives,” *Electrical Machines and Drives*, 1995.
[30] J. D.Ede, G. W. Jewell, and K. Atallah, “Design of a 250kW, fault tolerant PM generator for the more electric Aircraft,” in *3rd International Energy Conversion Engineering Conference*, San Francisco, California, 2005.
[31] A. M. El-Refaie and T. M. Jahns, “Impact of Winding Layer Number and Magnet Type on Synchronous Surface PM Machines Designed for Wide Constant-Power Speed Range Operation,” *Energy Conversion, IEEE Transactions on*, vol. 23, no. 1, pp. 53-60, 2008.
[32] D. Ishak, Z. Q. Zhu, and D. Howe, “Comparison of PM brushless motors, having either all teeth or alternate teeth wound,” *Energy Conversion, IEEE Transactions on DOI - 10.1109/TEC.2005.853765*, vol. 21, no. 1, pp. 95- 103, 2006.
[33] S. Williamson, M. Lukic, and A. Emadi, “Comprehensive drive train efficiency analysis of hybrid electric and fuel cell vehicles based on motor-controller efficiency modeling,” *Power Electronics, IEEE Transactions on DOI - 10.1109/TPEL.2006.872388*, vol. 21, no. 3, pp. 730-740, 2006.

[34] S. M. Lukic and A. Emado, “Modeling of electric machines for automotive applications using efficiency maps,” in *Electrical Insulation Conference and Electrical Manufacturing & Coil Winding Technology Conference, 2003. Proceedings*, 2003, pp. 543-550.
[35] K. B. Wipke, M. R. Cuddy, and S. D. Burch, “ADVISOR 2.1: a user-friendly advanced powertrain simulation using a combined backward/forward approach,” *Vehicular Technology, IEEE Transactions on DOI - 10.1109/25.806767*, vol. 48, no. 6, pp. 1751-1761, 1999.
[36] A. J. Mitcham, G. Antonopoulos, and J. J. A. Cullen, “Favourable slot and pole number combinations for fault tolerant PM mahicnes,” *IEE Proc. -Electr. Power*, vol. 151, 2004.
[37] A. M. El-Refaie, Z. Q. Zhu, T. M. Jahns, and D. Howe, “Winding Inductances of Fractional Slot Surface-Mounted Permanent Magnet Brushless Machines,” in *Industry Applications Society Annual Meeting, 2008. IAS ’08. IEEE*, 2008, pp. 1-8.
[38] Nicola Bianchi, Michele Dai Pre’, Luigi Alberti, and Emanuele Fornasiero, *Theory and Design of Fractional-Slot PM Machines*. 2007.
[39] N. Bianchi and S. Bolognani, “Design criteria of high efficiency SPM synchronous motors,” *IEEE Trans. on Energy Conversion*, vol. EC–21, no. 2, pp. 396-404, 2006.
[40] P. P., B. B.K., J. T.M., and L. R.D., *Performance and Design of Permanent Magnet AC Motor Drives*. IEEE Industrial Drives and Education committees of the Industry Applications Society, 1991.
[41] Chen, G.H. and Tseng, K.J., “Design of a permanent-magnet direct-driven wheel motor drive for electric vehicle,” presented at the Power Electronics Specialists Conference, 1996. PESC ’96 Record., 27th Annual IEEE, 1996, vol. 2, pp. 1933 - 1939.
[42] Pia Salminen, “FRACTIONAL SLOT PERMANENT MAGNET SYNCHRONOUS MOTORS FOR LOW SPEED APPLICATIONS,” Lappeenranta University of Technology, 2004.
[43] Florence Meier, “Permanent-Magnet Synchronous Machines with Non-Overlapping Concentrated Windings f or Low-Sp eed Direct-Drive Applications,” Roya l Institute of Technology, Sto ckholm, 2008.
[44] D. Ishak, Z. Q. Zhu, and D. Howe, “Permanent-magnet brushless machines with unequal tooth widths and similar slot and pole numbers,” *Industry Applications, IEEE Transactions on*, vol. 41, no. 2, pp. 584-590, 2005.
[45] Z. Q. Zhu and D. Howe, “Influence of design parameters on cogging torque in permanent magnet machines,” *Energy Conversion, IEEE Transactions on*, vol. 15, no. 4, pp. 407-412, 2000.
[46] N. Bianchi, S. Bolognani, and F. Luise, “Analysis and Design of a PM Brushless Motor for High-Speed Operations,” *Energy Conversion, IEEE Transactions on*, vol. 20, no. 3, pp. 629-637, 2005.
[47] Z. Q. Zhu, D. Howe, E. Bolte, and B. Ackermann, “Instantaneous magnetic field distribution in brushless permanent magnet DC motors. I. Open-circuit field,” *Magnetics, IEEE Transactions on*, vol. 29, no. 1, pp. 124-135, 1993.
[48] Z. Q. Zhu and D. Howe, “Instantaneous magnetic field distribution in brushless permanent magnet DC motors. III. Effect of stator slotting,” *Magnetics, IEEE Transactions on*, vol. 29, no. 1, pp. 143-151, 1993.
[49] D. Hanselman, *Brushless permanent-magnet motor design*. New York: McGraw-Hill, 1994.
[50] Z. Q. Zhu and D. Howe, “Instantaneous magnetic field distribution in brushless permanent magnet DC motors. II. Armature-reaction field,” *Magnetics, IEEE Transactions on*, vol. 29, no. 1, pp. 136-142, 1993.

[51] Z. Q. Zhu and D. Howe, “Instantaneous magnetic field distribution in permanent magnet brushless DC motors. IV. Magnetic field on load,” *Magnetics, IEEE Transactions on*, vol. 29, no. 1, pp. 152-158, 1993.
[52] Z. Q. Zhu, K. Ng, N. Schofield, and D. Howe, “Improved analytical modelling of rotor eddy current loss in brushless machines equipped with surface-mounted permanent magnets,” *Electric Power Applications, IEE Proceedings* -, vol. 151, no. 6, pp. 641-650, 2004.
[53] “Calculation of synchronous reactances of small permanent magnet alternating current motors comparison of analytical approach and finite element method with measurements,” 1998.
[54] A. Vagati, G. Pellegrino, and P. Guglielmi, “Comparison between SPM and IPM motor drives for EV application,” in *Electrical Machines (ICEM), 2010 XIX International Conference on*, 2010, pp. 1-6.
[55] G. Pellegrino, A. Vagati, P. Guglielmi, and B. Boazzo, “Performance Comparison Between Surface-Mounted and Interior PM Motor Drives for Electric Vehicle Application,” *Industrial Electronics, IEEE Transactions on DOI - 10.1109/TIE.2011.2151825*, vol. 59, no. 2, pp. 803-811, 2012.
[56] N. Bianchi and S. Bolognani, “Parameters and volt-ampere ratings of a synchronous motor drive for flux-weakening applications,” *Power Electronics, IEEE Transactions on*, vol. 12, no. 5, pp. 895-903, 1997.
[57] R. Krishnan, *Electric motor drives : modeling, analysis, and control*. Upper Saddle River: Prentice Hall, 2001.
[58] Magnussen, F. and Sadarangani, C., “Winding factors and Joule losses of permanent magnet machines with concentrated windings,” presented at the Electric Machines and Drives Conference, 2003. IEMDC’03. IEEE International, 2003, vol. 1, pp. 333-339.
[59] J. Soulard, S. Meier, and Y.-K. Chin, “Modeling of Iron Losses in Permanent Magnet with Field-Weakening Capability,” 2002.
[60] A. KRINGS and J. SOULARD, “Overview and Comparison of Iron Loss Models for Electrical Machines.”
[61] M. Chunting, G. R. Slemon, and R. Bonert, “Modeling of iron losses of permanent-magnet synchronous motors,” *Industry Applications, IEEE Transactions on*, vol. 39, no. 3, pp. 734-742, 2003.
[62] T. J. E. Miller and R. Rabinovici, “Back-EMF waveforms and core losses in brushless DC motors,” *Electric Power Applications, IEE Proceedings* -, vol. 141, no. 3, pp. 144-154, 1994.
[63] J.R.Hendershot and T. Miller, *Design of brushless permanent-magnet motors*. New York: Oxford University Press Inc., 1994.
[64] *SPEED manual: SPEED’s electric motors*. University of Glasgow, 2002.
[65] F. G. Capponi, R. Terrigi, and G. De Donato, “A synchronous axial flux PM machine d,q axes model which takes into account iron losses, saturation and temperature effects on the windings and the permanent magnets,” in *Power Electronics, Electrical Drives, Automation and Motion, 2006. SPEEDAM 2006. International Symposium on*, 2006, pp. 421-427.
[66] K. Yamazaki, “Torque and efficiency calculation of an interior permanent magnet motor considering harmonic iron losses of both the stator and rotor,” *Magnetics, IEEE Transactions on*, vol. 39, no. 3, pp. 1460-1463, May 2003.
[67] Z. Q. Zhu, Y. S. Chen, and D. Howe, “Iron loss in permanent-magnet brushless AC machines under maximum torque per ampere and flux weakening control,” *Magnetics, IEEE Transactions on DOI - 10.1109/TMAG.2002.802296*, vol. 38, no. 5, pp. 3285- 3287, 2002.

[68] P. H. Mellor, R. Wrobel, and D. Holliday, “A computationally efficient iron loss model for brushless AC machines that caters for rated flux and field weakened operation,” in *Electric Machines and Drives Conference, 2009. IEMDC ’09. IEEE International*, 2009, pp. 490-494.
[69] Bianchi, N., Bolognani, S., and Fornasiero, E., “A General Approach to Determine the Rotor Losses in Three-Phase Fractional-Slot PM Machines,” presented at the Electric Machines & Drives Conference, 2007. IEMDC ’07. IEEE International, 2007, vol. 1, pp. 634 - 641.
[70] M. Lazzari, A. Miotto, A. Tenconi, and S. Vaschetto, “Analytical prediction of eddy current losses in retaining sleeves for surface mounted PM synchronous machines,” in *Electrical Machines (ICEM), 2010 XIX International Conference on*, 2010, pp. 1-6.
[71] J. Alexandrova, H. Jussila, J. Nerg, Pyrho, x, and J. nen, “Comparison between models for eddy-current loss calculations in rotor surface-mounted permanent magnets,” in *Electrical Machines (ICEM), 2010 XIX International Conference on*, 2010, pp. 1-6.
[72] A. Jassal, H. Polinder, D. Lahaye, and J. A. Ferreira, “Comparison of analytical and Finite Element calculation of eddy-current losses in PM machines,” in *Electrical Machines (ICEM), 2010 XIX International Conference on*, 2010, pp. 1-7.
[73] Bianchi, N. and Fornasiero, E., “Impact of MMF Space Harmonic on Rotor Losses in Fractional-Slot Permanent-Magnet Machines,” *Energy Conversion, IEEE Transactions on*, vol. 24, no. 2, pp. 323 - 328, Jun. 2009.
[74] L. Alberti, E. Fornasiero, and N. Bianchi, “Impact of the rotor yoke geometry on rotor losses in permanent magnet machines,” in *Energy Conversion Congress and Exposition (ECCE), 2010 IEEE*, 2010, pp. 3486-3492.
[75] N. Bianchi and E. Fornasiero, “Index of rotor losses in three-phase fractional-slot permanent magnet machines,” *Electric Power Applications, IET*, vol. 3, no. 5, pp. 381-388, 2009.
[76] M. R. Shah and L. Sang Bin, “Rapid analytical optimization of eddy-current shield thickness for associated loss minimization in electrical Machines,” *Industry Applications, IEEE Transactions on*, vol. 42, no. 3, pp. 642-649, 2006.
[77] H. Toda, X. Zhenping, W. Jiabin, K. Atallah, and D. Howe, “Rotor eddy-current loss in permanent magnet brushless machines,” *Magnetics, IEEE Transactions on*, vol. 40, no. 4, pp. 2104-2106, 2004.
[78] K. Atallah, D. Howe, P. H. Mellor, and D. A. Stone, “Rotor loss in permanent-magnet brushless AC machines,” *Industry Applications, IEEE Transactions on*, vol. 36, no. 6, pp. 1612-1618, 2000.
[79] X. Hung Vu, D. Lahaye, M. J. Hoeijmakers, H. Polinder, and J. A. Ferreira, “Studying rotor eddy current loss of PM machines using nonlinear FEM including rotor motion,” in *Electrical Machines (ICEM), 2010 XIX International Conference on*, 2010, pp. 1-7.
[80] M. Ehsani, *Modern electric, hybrid electric, and fuel cell vehicles fundamentals, theory, and design*, 2nd édition. Boca Raton: CRC Press, 2010.
[81] A. E. Fuhs, *Hybrid vehicles and the future of personal transportation*. Boca Raton: CRC Press, 2009.
[82] M. Ehsani, Yimin Gao, and J. M. Miller, “Hybrid Electric Vehicles: Architecture and Motor Drives,” *Proceedings of the IEEE DOI - 10.1109/JPROC.2007.892492*, vol. 95, no. 4, pp. 719-728, 2007.
[83] L. Lu and M. Ouyang, “How to determine the electric car design specifications?,” presented at the The 25th World Battery, Hybrid and Fuel Cell Eletric Vehicle Symposium & Exhibition, Shenzhen,China, 2010.

[84] J. L. Besnerais, V. Lanfranchi, and M. Hecquet, “Multiobjective optimization of induction machines including mixed variables and noise minimization,” *IEEE TRANSACTIONS ON MAGNETICS*, vol. 44, no. 6, 2008.
[85] K. Deb, A. Pratap, S. Agarwal, and T. Meyarivan, “NSGA-II A Fast and Elitist Multiobjective Genetic Algorithm,” *Evolutionary Computation, IEEE Transactions on*, vol. 6, no. 2, 2002.
[86] N. Bianchi and S. Bolognani, “Brushless dc motor design: an optimization procedure based on genetic algorithms,” 1997.
[87] D. R. and R. M.F., “Analysis and Comparison of Methods for Determining d- and q-axes Inductances of IPM Machines,” presented at the Electric Machines and Drives, 2005 IEEE International Conference on, 2005, pp. 359-365.
[88] B. J.M. and M. J.W., “Fractional-Slot Surface Mounted PM Motors with Concentrated Windings for HEV Traction Drives,” OAK RIDGE NATIONAL LABORATORY, Oak Ridge,Tennessee 37831, Oct. 2005.
[89] J. Wai and T. M. Jahns, “A new control technique for achieving wide constant power speed operation with an interior PM alternator machine,” presented at the Industry Applications Conference, 2001. Thirty-Sixth IAS Annual Meeting. Conference Record of the 2001 IEEE, 2001, vol. 2, pp. 807 - 814.
[90] M. Barcaro, A. Faggion, L. Sgarbossa, N. Bianchi, and S. Bolognani, “Performance evaluation of an integrated starter alternator using an interior permanent magnet machine,” *Electric Power Applications, IET*, vol. 4, no. 7, pp. 539-546, 2010.
[91] Group PED4-1038C, “Torque Control in Field Weakening Mode,” Institute of Energy Technology, Aalborg University, Jun. 2009.
[92] Wang Zhengguang, Jin Jianxun, and Y. Guo, “Modeling and Simulation of PMSM Control System Based on SVPWM,” presented at the 27 th Chinese Control Conference, KunMing,China, 2008.

APPPENDICES

Coefficients extraction from the lamination datasheet

Coefficients extraction is implemented both for the Modified Steinmetz method and for the magnetic field method. Table 39 shows the iron loss datasheet of Vacoflux 48 Cobalt-iron Alloy at different values of frequency and flux density.

Table 39 Iron losses of Vacoflux 48 Cobalt-iron Alloy (W/kg)

f (Hz)	p_{Fe} (B=1T)	p_{Fe} (B=1.5T)	p_{Fe} (B=2T)
50	0.812	1.470	2.379
60	0.998	1.799	2.929
100	1.809	3.279	5.298
400	10.527	20.594	34.290
1000	38.189	85.875	155.655
2000	111.268	278.520	539.845
5000	523.149	1449.583	2970.145

First is to extract the coefficients of Modified Steinmetz method. The original Steinmetz equation is given by

$$p_{Fe}(B_m) = C_h f B_m^{a+bB_m} + C_e f^2 B_m^2$$

To get the value of C_h and C_e, the equation is divided by f to get the form as

$$\frac{p_{Fe}(B_m)}{f} = D + Ef$$

With the manufacture date sheet, three lines of $(p_{Fe}\ (B_m))/f$ can be drawn versus different frequencies f as shown in Figure 125. Then three values of D can be obtained from the intercept on the vertical axis of the three lines. Because

$$D = C_h B_m^{a+bB_m}$$

then with three different values of B_m, 1T, 1.5T and 2T in this case, the coefficients C_h, a and b can be solved. At the same time, three values of E can also be obtained from the slope of the lines. The maximum value of E is used to calculate C_e.

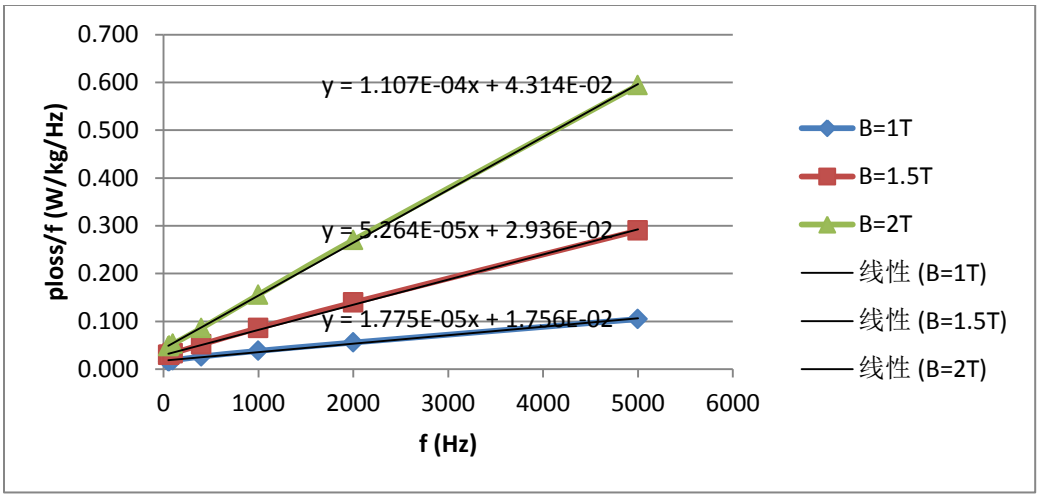

Figure 125 Linearization of the lamination datasheet

The extracted values of iron loss coefficients from the manufacture datasheet are shown in Table 40. Figure 126 indicates the difference between the estimation of iron loss density by Steinmetz equation and the datasheet.

Table 40 The coefficients of iron loss calculation

C_h	a	b	C_e
0.018	1.181	0.058	2.768e-5

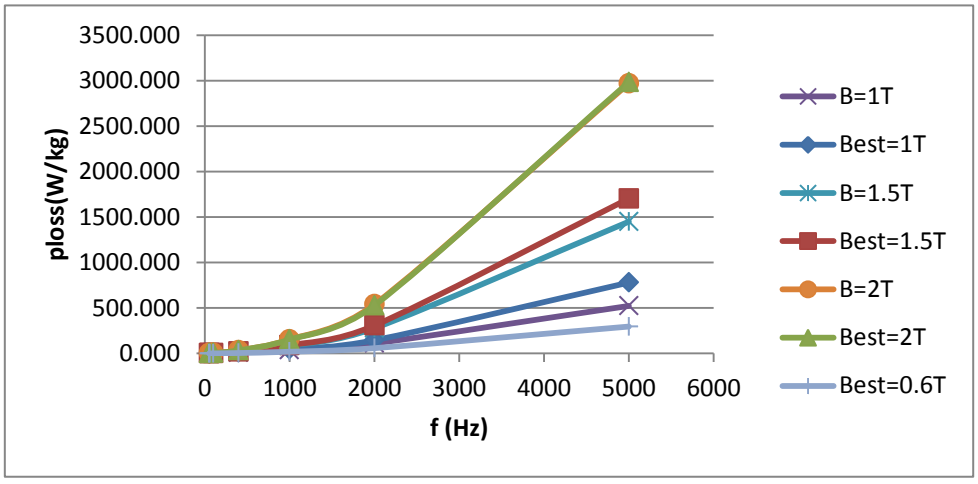

Figure 126 Comparison between estimation and datasheet

The coefficients of Steinmetz equation are extracted as abovementioned. After the coefficients are known, Steinmetz equation is used to estimate iron losses at other values of frequency. Based on the data of iron losses estimated from Steinmetz equation, the coefficients of equation (2.139) are extracted as following.

The physical property of Vacoflux 48 Cobalt-iron Alloy is shown in Table 41. For a 10 pole pairs motor, the calculated loss density at certain speeds is shown in Table 42. Consequently, with two

equations k_{exc} and k_h can be calculated for different values of speed. The calculated results are shown in Table 43.

Table 41 Physical property of Vacoflux 48 Cobalt-iron Alloy

Mass density ρ_s ($\mathrm{kg/m^3}$)	8120
Electrical conductivity σ ($\mathrm{S/m}$)	2.2727e6
Thickness of lamination d (m)	0.0002

Table 42 Calculated iron loss density

Speed (rpm)	Frequency (Hz)	Loss density with B=1T (W/kg)	Loss density with B=1.5T (W/kg)
111	18.5	0.334331769	0.564471
333	55.5	1.059825919	1.821281
667	111.16667	2.294095876	4.033369
1000	166.66667	3.69541756	6.623015
1500	250	6.1196875	11.23179
2000	333.33333	8.928332133	16.7054

Table 43 Calculated coefficients for different frequency

Speed (rpm)	111	333	667	1000	1500	2000
Frequency (Hz)	18.5	55.5	111.1667	166.6667	250	333.3333
k_h	-55.5456	-52.8334	-48.6676	-44.4971	-38.2346	-31.9651
k_{exc}	5.35007	3.0901	2.1837	1.7834	1.4562	1.261